University of Glasgow

Gregory, Thomas (2022) *Quantum enhanced imaging*. PhD thesis.

https://theses.gla.ac.uk/82788/

Copyright and moral rights for this work are retained by the author

A copy can be downloaded for personal non-commercial research or study, without prior permission or charge

This work cannot be reproduced or quoted extensively from without first obtaining permission in writing from the author

The content must not be changed in any way or sold commercially in any format or medium without the formal permission of the author

When referring to this work, full bibliographic details including the author, title, awarding institution and date of the thesis must be given

Enlighten: Theses
https://theses.gla.ac.uk/
research-enlighten@glasgow.ac.uk

Quantum Enhanced Imaging

Thomas Gregory

Submitted in fulfilment of the requirements for the

Degree of Doctor of Philosophy

School of Physics and Astronomy

College of Science and Engineering

University of Glasgow

August 2021

Abstract

Exploiting the quantum properties of entangled photon-pairs allows the limits of classical imaging to be surpassed, whether that may be imaging beyond the shot-noise limit or the classical limits of resolution. Full-field imaging of quantum correlations has recently become possible as a result of single-photon sensitive detector arrays thereby offering a substantial reduction in the time required to acquire an image when compared to the scanning-fibre techniques previously employed. The work presented in this thesis seeks to utilise the spatial correlations between entangled photon-pairs to improve quantum imaging techniques such that quantum-enhanced imaging may be applied in real-world applications. Such applications included in this work include contrast-enhanced and resolution-enhanced imaging which may find applications in quantum enhanced microscopy, and quantum Lidar.

Contents

Abstract **i**

Acknowledgements **xii**

Declaration of Authorship **xiii**

Publications **xiv**

Abbreviations **xvii**

1 Introduction **1**

1.1 Preamble 1

1.2 The Photon and Quantum Mechanics 2

1.3 Quantum Entanglement 3

1.4 Spontaneous Parametric Downconversion 7

1.5 Quantum-Enhanced Imaging 14

1.6 Walkthrough 23

2 Experimental Methods **24**

2.1 Introduction 24

2.2 Downconversion Sources 24

2.3 Spatial Correlations 28

2.3.1 Poissonian Statistics 33

2.3.2 Klyshko Advanced Wave Picture 35

2.4 Detector Technologies 36

2.4.1 EMCCD Cameras . . . 37
2.4.2 ICCD Camera . . . 41
2.4.3 Camera Selection . . . 45

3 Contrast Enhanced Imaging 48
3.1 Introduction . . . 48
3.2 Experimental Methods . . . 49
3.2.1 Experimental Setup . . . 49
3.2.2 Data Analysis . . . 50
3.3 Theory . . . 51
3.3.1 Quantum Efficiency . . . 55
3.4 Results . . . 56
3.5 Discussion . . . 59

4 Quantum Illumination as Applied to Full-Field Imaging 61
4.1 Introduction . . . 61
4.2 Experimental Methods . . . 62
4.2.1 Experimental Setup . . . 62
4.2.2 Data Analysis . . . 63
4.3 Theory . . . 64
4.4 Results . . . 66
4.4.1 Quantum Illumination Contrast Enhancement . . . 66
4.4.2 Bit Error Rate Enhancement . . . 70
4.4.3 Rejection of Structured Background . . . 76
4.5 Discussion . . . 80

5 Noise Rejection Through An Improved Quantum Illumination Protocol 82
5.1 Introduction . . . 82
5.2 Methods . . . 83
5.2.1 Imaging system . . . 83

5.2.2 Image analysis 84
5.3 Results 86
5.3.1 Rejection of structured thermal illumination 86
5.3.2 Noise Rejection in Imaging a Complex Object 91
5.4 Discussion 92

6 Improved Data Extraction Techniques 94
6.1 Introduction 94
6.2 Integrating Correlations Over Extent of Peak 94
6.2.1 Contrast Enhancement 96
6.2.2 Noise Rejection 102
6.3 Optimisation of the Distinguishability 107
6.3.1 AND-images optimisation 107
6.3.2 AND-images with accidentals subtracted optimisation 115
6.3.3 Application of Optimisation Solution to an Unknown Scene 124
6.4 Discussion 127

7 Conclusions 128

A Tables of Optimisation Values 131

List of Figures

1.1 Diagram of the EPR thought experiment 5

1.2 Diagram of SHG and PDC frequency conversion 9

1.3 Diagram of collinear and near-collinear phase matching 11

1.4 Diagram of the downconverted beams emitted via SPDC in the case of type-I and type-II phase-matching 14

1.5 SPDC rings from downconversion source with type-II phase matching 15

2.1 Diagram of the generation of 355nm light by an Nd:YAG laser 25

2.2 Diagram of the quantum illumination setup pre-crystal 27

2.3 Diagram of the spatial correlations between photon-pair events incident upon an array detector 30

2.4 Diagram of a correlation peak from simulated data 31

2.5 Diagram of a correlation peak from experimental data 32

2.6 Degree of Correlation 35

2.7 Klyshko Advanced Wave Picture applied to ghost imaging 36

2.8 Schematic of readout including additional EM gain register for EMCCD cameras 39

2.9 Histograms of analogue counts for frames obtained using an EMCCD camera . 40

2.10 Schematic of intensifier for ICCD cameras 42

2.11 Histograms of analogue counts for frames obtained using an ICCD camera . . . 43

2.12 Image of the blooming effect for ICCD cameras 44

2.13 Quantum enhanced images obtained using an EMCCD and an ICCD for the purposes of comparison 47

3.1 Schematic of the contrast enhanced imaging experimental setup 50
3.2 Demonstration of the AND-operation 51
3.3 Plot of the ratio of real correlated events vs fill-factor 53
3.4 Plot of the ratio of real correlated events vs AND-efficiency 54
3.5 Plot of the ratio of real correlated events vs AND-efficiency 55
3.6 Plot of the contrast advantage ratio vs AND-efficiency 56
3.7 Contrast enhancement demonstrated with a binary test target 57
3.8 Real-world binary objects imaged to demonstrate contrast enhancement 59

4.1 Schematic of the quantum illumination experimental setup 63
4.2 Images of UoG using quantum illumination within a thermal background . . . 67
4.3 Graph of the quantum illumination advantage under an increasing a thermal background 68
4.4 Imaging using quantum illumination with losses introduced 69
4.5 Graph of the quantum illumination advantage under increasing losses 70
4.6 The bit error rate P_{err} of detecting a target calculated over a range of thermal light levels using the blind strategy 73
4.7 The bit error rate P_{err} of detecting a target calculated over a range of thermal light levels using the non-blind strategy 75
4.8 Images of the rejection of structured thermal illumination 77
4.9 Images of quantum illuminated object preferentially selected over thermally illuminated mask with increasing thermal illumination and the introduction of losses 79

5.1 The quantum illumination experimental setup 83
5.2 Images of the classically acquired image, the quantum illumination AND-image, and the quantum illumination AND-image with accidentals subtracted for the bird in a cage 88
5.3 Images of a wasp wing 92

6.1 Figure displaying the order of the offsets for integrating the correlations over the extent of the correlation peak 95

6.2 Comparison of images resulting from performing the original AND-operation and the peak integration method for the UoG object under differing levels of thermal illumination 97

6.3 Comparison of images resulting from performing the original AND-operation and the peak integration method for the UoG object under differing levels of loss in the probe beam 98

6.4 Comparison of images resulting from performing the subtraction operation after applying the peak integration method for the UoG object under differing levels of thermal illumination 100

6.5 Comparison of images resulting from performing the subtraction operation after applying the peak integration method for the UoG object under differing levels of loss in the probe beam 101

6.6 Comparison of images created by performing the original AND-operation and the peak integration method for the bird in a cage object under differing levels of thermal illumination 104

6.7 Comparison of images created by performing the subtraction operation in combination with the peak integration method for the bird in a cage object under differing levels of thermal illumination 106

6.8 Optimised combination of AND-images of the bird in a cage object constructed using a 1×1 kernel combined to maximise the distinguishability metric 110

6.9 Combination of AND-images of the bird in a cage object constructed using a 1×1 kernel using average optimised solution for Thermal illumination to SPDC illumination ratios of $1.1\times$ to $7.3\times$ 112

6.10 Optimised combination of AND-images of the bird in a cage object constructed using a 3×3 kernel combined to maximise the distinguishability metric 114

6.11 Optimised combination of AND-images with accidentals subtracted for the bird in a cage object constructed using a 1×1 kernel combined to maximise the distinguishability metric 116

6.12 Combination of AND-images with accidentals subtracted for the bird in a cage object constructed using a 1×1 kernel using the optimised solution for the set of AND-images with accidentals subtracted obtained across the entire range of thermal illumination to SPDC illumination ratios of $0.5\times$ to $19.3\times$ 118

6.13 Optimised combination of AND-images with accidentals subtracted constructed using a 3×3 kernel combined to maximise the distinguishability metric. 120

6.14 Combination of AND-images with accidentals subtracted constructed using a 3×3 kernel using the optimised solution for the set of AND-images with accidentals subtracted obtained across the entire range of thermal illumination to SPDC illumination ratios of $0.5\times$ to $19.3\times$. 122

6.15 Combination of AND-images with accidentals subtracted constructed using a 1×1 kernel using the optimised solution for the set of AND-images with accidentals subtracted for the fish in a net object obtained across the entire range of thermal illumination to SPDC illumination ratios of $0.5\times$ to $19.3\times$ 125

6.16 Combination of AND-images with accidentals subtracted constructed using a 3×3 kernel using the optimised solution for the set of AND-images with accidentals subtracted for the fish in a net object obtained across the entire range of thermal illumination to SPDC illumination ratios of $0.5\times$ to $19.3\times$ 126

List of Tables

3.1 Table of the quantum efficiencies of system components used to calculate total QE of the experimental setup 57

5.1 Table of the proportion of the thermally illuminated cage that remain in the quantum illumination AND-image and the quantum illumination AND-image with accidentals subtracted 90

5.2 Table of the average number of events in the pixels that correspond to the regions of the final images that solely correspond to the quantum illuminated bird . . . 91

6.1 Table of the proportion of a Gaussian with widths of $\sigma_x = 1.29$ and $\sigma_y = 1.70$ contained within a kernel of 1, 3, and 5 pixels 95

6.2 Table of distinguishabilities for the bird in a cage images created by performing the original AND-operation and the peak integration method for the bird in a cage object under differing levels of thermal illumination 103

6.3 Table of distinguishabilities for the bird in a cage images constructed by implementing the peak integration method and the subtraction operation 105

6.4 Table of mean and standard deviation of the entire quantum illuminated bird object regions for the bird in a cage images constructed by implementing the peak integration method and the subtraction operation 107

6.5 Table of the proportions of different ranges of AND-images used to construct the optimised AND-image of the bird in a cage object for a 1×1 kernel 109

6.6 Table of the proportions of different ranges of AND-images used to construct the optimised AND-image of the bird in a cage object for a 3×3 kernel 115

6.7 Table of the proportions of different ranges of AND-images used to construct the optimised AND-image of the bird in a cage object for a 1×1 kernel 117

6.8 Table of the distinguishability ratios for the optimised combinations of each set of AND-images with accidentals subtracted of the bird in a cage object constructed using a 1×1 kernel 119

6.9 Table of the proportions of different ranges of AND-images used to construct the optimised AND-image for a 3×3 kernel 121

6.10 Table of the distinguishability ratios for the optimised combinations of each set of AND-images with accidentals subtracted constructed using a 3×3 kernel . . 123

6.11 Table of the improvement in the distinguishability ratios using the improved data extraction techniques for the bird in a cage object 123

6.12 Table of the improvement in the distinguishability ratios using the improved data extraction techniques for the fish in a net object 124

A.1 Table of the optimisation solution for the combination of AND-images constructed using a 1×1 kernel combined to maximise the distinguishability metric for each of the thermal illumination to SPDC illumination ratios of $0.5\times$ to $19.3\times$.132

A.2 Table of the generalised optimisation solution for the combination of AND-images constructed using a 1×1 kernel using the optimised solution for thermal illumination to SPDC illumination ratios of $1.1\times$ to $7.3\times$. 133

A.3 Table of the optimisation solution for the combination of AND-images constructed using a 3×3 kernel combined to maximise the distinguishability metric for each of the thermal illumination to SPDC illumination ratios of $0.5\times$ to $19.3\times$.134

A.4 Table of the optimisation solution for the combination of AND-images with accidentals subtracted constructed using a 1×1 kernel combined to maximise the distinguishability metric for each of the thermal illumination to SPDC illumination ratios of $0.5\times$ to $19.3\times$.. 135

A.5 Table of the generalised optimisation solution for the combination of AND-images with accidentals subtracted constructed using a 1×1 kernel using the optimised solution for the set of AND-images with accidentals subtracted obtained across the entire range of thermal illumination to SPDC illumination ratios of 0.5× to 19.3×. 136

A.6 Table of the optimisation solution for the combination of AND-images with accidentals subtracted constructed using a 3×3 kernel combined to maximise the distinguishability metric for each of the thermal illumination to SPDC illumination ratios of 0.5× to 19.3×.. 137

A.7 Table of the generalised optimisation solution for the combination of AND-images with accidentals subtracted constructed using a 3×3 kernel using the optimised solution for the set of AND-images with accidentals subtracted obtained across the entire range of thermal illumination to SPDC illumination ratios of 0.5× to 19.3×. 138

Acknowledgements

With thanks to my supervisor Miles Padgett, my lab supervisor Paul-Antoine Moreau, my lab partners Ermes Toninelli, Osian Wolley, and Simon Mekhail, and to all the Optics Group.

The work on Contrast Enhanced Imaging presented in Chapter 3 was performed in collaboration with E. Toninelli, P.-A. Moreau, and M.J. Padgett. This work forms preliminary work for that presented in the following chapters and is unpublished.

The work on Quantum Illumination as Applied to Full-Field Imaging presented in Chapter 4 was performed in collaboration with P.-A. Moreau, E. Toninelli, and M.J. Padgett. This work is published in *Science Advances*.

The work on Noise Rejection Through An Improved Quantum Illumination Protocol presented in Chapter 5 was performed in collaboration with P.-A. Moreau, S. Mekhail, O. Wolley, and M.J. Padgett. This work is published in *Scientific Reports*.

The work on Improved Data Extraction Techniques presented in Chapter 6 was performed in collaboration with S. Mekhail, O. Wolley, P.-A. Moreau, and M.J. Padgett. This work was conducted to inform future directions in research and is unpublished.

Declaration of Authorship

I hereby declare that this thesis is the result of my own work, except where explicit reference is made to the work of others, and has not been presented in any previous application for a degree at this or any other institution.

Thomas M. Gregory

Publications

During the course of my PhD studies a number of peer-reviewed papers were co-authored with colleagues in the Optics group at the University of Glasgow under the supervision of Miles J. Padgett and Paul-Antoine Moreau.

1. P.-A. Moreau, E. Toninelli, T. Gregory, and M.J. Padgett, "Ghost imaging using optical correlations". *Laser & Photonics Reviews* **12**, 1700143, (2017).

2. P.-A. Moreau, E. Toninelli, P.A. Morris, R.S. Aspden, T. Gregory, G. Spalding, R.W. Boyd, and M.J. Padgett, "Resolution limits of quantum ghost imaging". *Optics Express* **26**, 7528, (2018).

3. P.-A. Moreau, P.A. Morris, E. Toninelli, T. Gregory, R.S. Aspden, G. Spalding, R.W. Boyd, and M.J. Padgett, "Experimental limits of ghost diffraction Popper's thought experiment". *Scientific Reports* **8**, 13183, (2018).

4. E. Toninelli, P.-A. Moreau, T. Gregory, A. Mihalyi, M. Edgar, N. Radwell, and M.J. Padgett, "Resolution-enhanced quantum imaging by centroid estimation of biphotons". *Optica* **6**, 347, (2019).

5. P.-A. Moreau, E. Toninelli, T. Gregory, and M.J. Padgett, "Imaging with quantum states of light". *Nature Review Physics* **1**, 367-380, (2019).

6. P.-A. Moreau, E. Toninelli, T. Gregory, R.S. Aspden, P.A. Morris, and M.J. Padgett, "Imaging Bell-type non-Local behaviour". *Science Advances* **5**, eaaw2563, (2019).

7. E. Toninelli, P.-A. Moreau, T. Gregory, and M.J. Padgett, "A model for quantum imaging and sensing experiments based on the detection of correlated biphotons using a photon-counting camera". arXiv:1911.10562 [physics.ins-det] (2019).

8. T. Gregory, P.-A. Moreau, E. Toninelli, and M.J. Padgett, "Imaging through noise with quantum illumination". *Science Advances* **6**, eaay2652, (2020).

9. S.D. Johnson, P.-A. Moreau, T. Gregory, and M.J. Padgett, "Perspective: How many photons does it take to form an image?". *Applied Physics Letters* **116**, 260504, (2020).

10. T. Gregory, P.-A. Moreau, S. Mekhail, O. Wolley, and M.J. Padgett, "Improved Performance Of The Quantum Illumination Protocol By Noise Subtraction". *Scientific Reports* **11**, 21841, (2021).

11. O. Wolley, T. Gregory, S. Beer, T. Higuchi, and M.J. Padgett, "Quantum imaging with a photon counting camera". Currently Under Review

12. T. Gregory, M.P. Edgar, G.M. Gibson, and P.-A. Moreau, "A Gigapixel Computational Light-Field Camera". arXiv:1910.08338 [physics.optics] (2019).

Conference Proceedings and Presentations

1. T. Gregory, P.-A. Moreau, E. Toninelli, and M.J. Padgett, "Contrast Enhanced Imaging Using Quantum Correlations". Presented at IONS Scandinavia, Danmarks Tekniske Universitet, Copenhagen, Denmark (2018) (Poster Presentation).

2. T. Gregory, P.-A. Moreau, E. Toninelli, and M.J. Padgett, "Contrast Enhanced Imaging Using Quantum Correlations". Quantum Information and Measurement V: Quantum Technologies, OSA Technical Digest T5A.65, (2019). Presented at Quantum Information and Measurement V: Quantum Technologies, Sapienza Università di Roma, Rome, Italy (2019) (Poster Presentation).

3. T. Gregory, P.-A. Moreau, E. Toninelli, and M.J. Padgett, "Full-Field Imaging With Quantum Illumination ". Presented at Photonics North 2020 Niagara Falls, ON, Canada, 2020 (Online Presentation).

4. M.J. Padgett, E. Toninelli, T. Gregory, and P.-A. Moreau, “Beating classical imaging limits with entangled photons,” Proc. SPIE 10934, 109341R-1–109341R-6 (2019). Includes preliminary work from item number 7 in publications list. Presented by M.J. Padgett 1st March 2019.

5. T. Gregory, P.-A. Moreau, E. Toninelli, and M.J. Padgett, "Full-Field Imaging With Quantum Illumination ". Presented at PhotonX 2020 (Poster Presentation).

Abbreviations

AWP	Klyshko Advanced Wave Picture
BBO	β-barium borate
CCD	Charge Coupled Device
CHSH	Clauser, Horne, Shimony, and Holt
CIC	Clock-Induced Charge
EMCCD	Electron-Multiplying Charge Coupled Device
EPR	Einstein-Podolsky-Rosen
FWHM	Full-Width Half-Maximum
ICCD	Intensified Charge Coupled Device
PPKTP	Periodically Poled Potassium Titanyl Phosphate
ROI	Region Of Interest
SNL	Shot noise Limit
SPAD	Single Photon Avalanche Detector
SPDC	Spontaneous Parametric Down-Conversion
SQL	Standard Quantum Limit
UoG	University of Glasgow

Chapter 1

Introduction

1.1 Preamble

The utilisation of quantum correlations allows the classical limits of imaging to be surpassed. This allows the development of new imaging systems that are capable of imaging with improved contrast, increased spatial resolution, and an enhanced ability to reject background noise. These advantages have the potential to greatly improve imaging under a low-photon flux and will therefore find application in biological imaging and covert imaging schemes. While the theoretical advantages of using quantum correlations has previously been demonstrated, there remains work to be done in realising imaging schemes that utilise these correlations for deployment in real-world settings. Therefore the development of imaging schemes that are capable of exploiting the advantages presented by quantum sources of illumination require research in order to ascertain their limitations and applicability. The continuing improvements in detector technology with regards to the development of single-photon-sensitive array detectors in addition to those that incorporate time-tagging will continue to move implementations of the aforementioned applications from lab-based ideal settings towards real-world implementations.

The work presented here was conducted in an attempt to answer the question:
"What is the potential quantum advantage in noise rejection that can be achieved when using a quantum source of illumination over a classical source when imaging under a low-photon flux?"

To answer this question a number of different imaging schemes were developed that sought to explore the potential enhancements that may be achieved using a quantum source of illumination. Such a source of illumination remains subject to both quantum mechanics and conservation laws and this knowledge may be exploited to extract a quantum advantage. Results will be presented here for a number of different imaging schemes that were designed to assess the achievable quantum advantage with regards to image contrast and background noise rejection.

The remainder of this introduction will describe the theory of the quantum sources of illumination that we use and will review the development of the field of quantum imaging such that the works presented in this thesis may be placed in the context of prior and contemporary work.

1.2 The Photon and Quantum Mechanics

The development of quantum mechanics was initiated by problems with the classical theory of light in describing the electromagnetic radiation emitted from a black-body, the photoelectric effect, and the photoluminesence of chemicals, amongst others. In seeking a solution to the black-body radiation problem, Planck hypothesised that the energy radiated or absorbed by a system is discretised as an integer multiple of $h\nu$ in which ν is the frequency of the emitted or incident radiation [1]. Einstein then further developed this idea of quantisation of energy into the form of a light quanta, a quanta of energy that is localised in space and indivisible. Such a body can only be emitted or absorbed in its totality, thereby giving rise to the concept of the photon [2]. This concept of a photon or a quanta of energy localised in space differs from the wave representation of light as formalised by Maxwell [3] in which the energy spreads throughout a volume that increases with respect to time. Despite this apparent difference in the distribution of the energy of the light field the two representations remain complementary because the wave representation may be viewed as a time averaged observation. In understanding an experiment in the field of quantum optics and quantum enhanced imaging it may be optimal to view the light field as acting as either a wave or a particle. Either may be considered a valid interpretation due to the complementary nature of the wave-particle duality of light and it must be so as to match

observations already made [4]. This wave-particle duality was then hypothesised to apply to particles with mass by de Broglie [5]. In his work it was assumed that the photon (or light quanta) is a particle with a finite mass, a point which was unclear at the time [6]. Regarding the ability to localise a particle, this was found to be fundamentally limited by the uncertainty principle which prevents a full description of the state in a classical sense as non-compatible observables do not commute [7].

The development of the complementary mathematical frameworks that underlie the theory of quantum mechanics by Heisenberg, Jordan, and Born [8–10], and Dirac [11], who developed the matrix formulation, and Schrödinger [12], who developed the wave formulation, eventually led to the determination that quantum mechanics is a statistical theory [13–16]. This interpretation of quantum mechanics led to discussions regarding the philosophical implications and questions on the issue of completeness [17–20], a subject that shall be touched on in the following section.

As a result of the works discussed here, the concept of the photon was conceived and quantum mechanics was formulated and this allows the state of a photonic system to be described. Now we must consider what advantages may be had in considering a system of photons in a quantum mechanical theory.

1.3 Quantum Entanglement

While the new theory of quantum mechanics (whose development was described in the preceding section) served to explain many of the problems upon which the classical theory floundered, there were questions regarding the completeness of the theory. In particular because quantum mechanics is inherently statistical in nature as the wavefunction of a system may only be used to determine the probabilities of results. This led to the famous Einstein-Podolsky-Rosen (EPR) paper in 1935 in which the authors proposed a thought experiment to illustrate their theory that quantum mechanics was incomplete because in their own words: "every element of the physical reality must have a counterpart in the physical theory" [17]. This was predicated on their belief that for a physical theory to be complete it should be possible to predict each physical quantity with certainty. In quantum mechanics this is not possible for observables with non-

commuting operators as there is a fundamental limit as dictated by the Heisenberg uncertainty principle [7]. In the thought experiment proposed by EPR a pair of subsystems corresponding to particles A and B figure 1.1a), that had interacted at some time denoted t_0 such that their properties become correlated but do not interact thereafter as they are then spatially separated 1.1b). A pair of non-commuting operators are then chosen, here chosen to correspond to observables position and momentum, and once a measurement of the position of particle A is performed at time t_1 figure 1.1c) the position of particle B is also known. However, this measurement of the position of particle A then precludes the prediction of a definite value for the momentum on particle B without making another measurement at some later time t_2 figure 1.1d) and further altering the state of the system. This results in the knowledge regarding the value of the position being destroyed. In the words of EPR, it is the case that under the theory of quantum mechanics "when the operators corresponding to two physical quantities do not commute the two quantifies cannot have simultaneous reality", which prompted their argument for quantum mechanics being incomplete. While the EPR paper largely represented an argument regarding realism within quantum mechanics, Einstein also had reservations based on the separability of the two particles and also regarding local causality which he combined into the separation principle in his correspondence with Schrödinger [21, 22]. In the letter Einstein stated that the two particles A and B within the EPR thought experiment should have separate and real states that are independent of one another after the collision, i.e that the state of the system post collision (AB) is a product of the states of particles A and B, and therefore that: "the real state of B thus cannot depend upon the kind of measurement I carry out on A". He also argued for the independence of particles that are spatially distant such that "an external influence on A has no immediate effect on B" which is an argument for local causality. Schrödinger responded with a three-part paper in which he described an interpretation of quantum mechanics and the wavefunction that rejected local realism and also rejected the separability argument of Einstein. He argued that for two particles that interact their wavefunctions become entangled and are non-separable [19, 20, 23, 24]. Schrödinger described the characteristic of entanglement stating that "I would not call [entanglement] *one* but rather *the* characteristic trait of quantum mechanics, the one that enforces its entire departure from classical lines of thought" [20]. Entanglement and

the non-local correlations that it exhibits serves to set quantum mechanics apart from classical interpretations as there is no classical equivalent. There have been claims as to the existence and observation of "classical entanglement", but by the very works in which it is defined, it is stated that it can not replicate the non-local entanglement between multiple particles that is the defining point of entanglement in quantum mechanics [25–27]. The term is used to describe a system in which a single particle is in a superposition of states and it is not possible to extend to the entanglement of multiple particles.

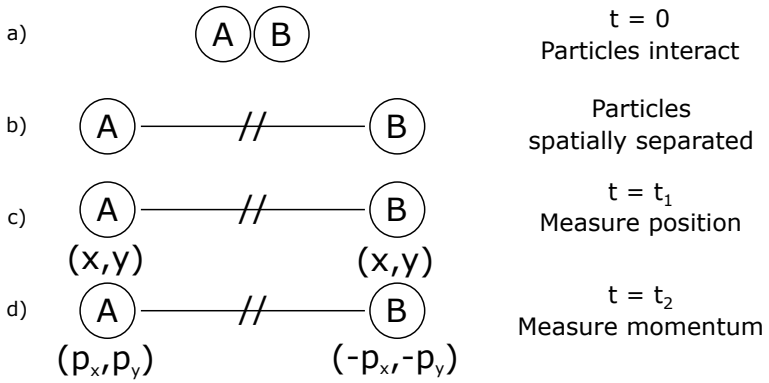

Figure 1.1: **Diagram of the EPR thought experiment.** A pair of subsystems corresponding to particles A and B that interact at time t_0 such that their properties become correlated a) and are then spatially separated b). A pair of non-commuting operators are then chosen, here chosen to correspond to observables position and momentum. Once a measurement of the position of particle A is performed at time t_1 c) the position of particle B is then also known. This measurement of the position of particle A then precludes the prediction of a definite value for the momentum on particle B without making another measurement at some later time t_2 d)

The question as to whether quantum mechanics was complete and reservations regarding its interpretation continued to trouble physicists [18, 28]. In order to address the issue surrounding realism, Bohm formulated a version of quantum mechanics with hidden variables. This model sought to satisfy the issues that EPR had with quantum mechanics not being able to afford a simultaneous reality to observables that correspond to non-commuting operators [29, 30]. Einstein had also previously attempted a hidden variable theory that modified quantum mechanics into a deterministic theory in an unpublished work in 1927 but withdrew it just prior to publication due to his doubts about his theory regarding the interdependence of particle trajectories within a multi-particle system [31, 32]. In such hidden variable theories the limiting factor with regards to the precision to which measurements may be made is due to practical limitations

and not inherent to the underlying theory of quantum mechanics. Von Neumann had previously worked to show that a hidden variable theories were not compatible with the theory of quantum mechanics [33] but it was not until Bell that a means to test the compatibility of experimental results with a local hidden variable theory was proposed. Bell, using the proposed experiment of Bohm and Aharanov to describe EPR as an example [34], determined that no local hidden variable theory could replicate the statistical predictions of the quantum mechanical theory [35] and derived inequalities that if violated for a given experiment show that the results can not support a local hidden variable theory. This theorem was found to apply to local hidden variable models that can be either deterministic or probabilistic in nature [36–38]. The results of Bell were backed by further proofs [39–41] and after generalising the Bell inequality Clauser, Horne, Shimony and Holt (CHSH) proposed an experiment by which quantum mechanics could be tested that utilised available technology [42]. This experiment was executed by Freedman and Clauser [43] utilising photons from an atomic cascade in calcium which was found to have polarisation correlations and which had also been used in a Bell-type experiment [44]. The results of this experiment, alongside those of many others show a violation of the Bell inequality and therefore support the hypothesis that quantum mechanics cannot contain local hidden variables [43, 45–51]. Tests for theories that require the existence of non-local hidden variables have also been formulated [52–55] and have also been violated in a similar manner by experiment [56–59]. The interpretation of quantum mechanics and the nature of quantum non-locality remains a subject of interest as evidenced by the works published in response to the questions posed by Popper [60–65]. See also the work of Genovese et al.(2019) [66] regarding quantum non-locality.

To formalise that which has been discussed in this section a pure state of the two quantum systems A and B prior to their interaction in the EPR thought experiment is defined as per equation 1.1. This represents a system that is not entangled as the states are separable because the wavefunction of the combined system is a product of the states of the subsystems A and B. After interacting and after separation the state of the system becomes an entangled state as per equation 1.2 and cannot be represented as a product of two separate states representing

subsystems A and B.

$$|\psi\rangle = |\psi\rangle_A |\psi\rangle_B \tag{1.1}$$

$$|\psi\rangle = \frac{1}{\sqrt{2}}(|0\rangle_A|0\rangle_B + |1\rangle_A|1\rangle_B) \tag{1.2}$$

The work presented in this thesis does not utilise the full extent of entanglement and rely on the correlations in the position and momentum of photon-pairs. Such correlations that may be found to violate the inequality represented in equation 1.3 are labelled as EPR entangled states [67–72].

$$\Delta^2_{min}(x_1|x_2)\Delta^2_{min}(p_1|p_2) \geq \frac{\hbar^2}{4} \tag{1.3}$$

After defining quantum mechanics and describing entanglement (see [73, 74] for more in depth description) a source of entangled particles is required to exploit the properties of entanglement and also to perform tests on its completeness such as those proposed by Bell. Photons are a prime candidate for such tests because they do not mechanically interact with other photons, are simple to detect (should a reasonable wavelength be chosen), and are not sensitive to quantum decoherence as they are not susceptible to environmental factors in the same manner as are charged particles [75]. Quantum entangled photons have a vast range of applications including quantum computing, quantum communications, quantum metrology and sensors, and quantum imaging [75–84]. The experiments presented in this thesis rely on our utilising the spatial correlations between entangled photon-pairs to perform quantum enhanced imaging and in the following section a source of entangled photon-pairs that exhibit such correlations shall be detailed.

1.4 Spontaneous Parametric Downconversion

As stated in the previous section cascaded two photon emission processes between energy levels in calcium atoms have been found to exhibit correlations in polarisation [43–47]. However,

the direction of emission of the photons in these cascades will be random thereby limiting the efficiency of any system which employs these cascades as a photon source and also limiting their usefulness in experiments which seek to exploit EPR correlations. After the invention of the laser, which allowed monochromatic beams of high intensity to be generated, it was discovered that pumping a dielectric material with such high intensity beams allows access to an increased number of different frequencies. These frequencies are generated by exploiting the non-linearities in the dielectric material [85–87]. The non-linearities in the material that is being pumped by the laser result in a non-linear response in the dipole moment per unit volume or polarisation (P) within the crystal to the incident electric field (E) as per equation 1.4 in which χ is the dielectric susceptibility of the medium [88]. The values for the higher order susceptibilities $\chi^{(n)}, n \geq 2$ are small when compared to the first-order linear susceptibility $\chi^{(1)}$. For comparison in condensed matter $\chi^{(1)}$ is of the order of 1 m/V while $\chi^{(2)}$ is of the order 1 pm/V, 12 orders of magnitude smaller [88]. Therefore to observe these non-linear effects requires large incident electric fields. $\chi^{(2)}$ effects such as those discussed here may only occur in crystals that do not display an inversion symmetry and are therefore noncentrosymmetric [88].

$$P(t) = \varepsilon_0[\chi^{(1)}E(t) + \chi^{(2)}E^2(t) + \chi^{(3)}E^3(t) + ...] \tag{1.4}$$

This effect was utilised in order to observe optical harmonics: second harmonic generation [89–92], sum frequency generation [93,94], and difference frequency generation [95,96]. These processes are χ^2 effects which are three-wave mixing processes and discussions shall be limited in this thesis to these second order effect. Higher order processes are not of import in the works presented here, see Nonlinear Optics by Boyd for a full description of these and higher order processes [88]. Second harmonic generation is the process in which a pair of low frequency pump photons are upconverted into a single output photon of higher frequency. Parametric amplification is the time reversed process in which a single high frequency pump photon is downconverted into a pair of low frequency photons so called the signal and idler photons. A diagram of both processes is displayed in figure 1.2 for comparison. Parametric amplification was developed as a stimulated process in which a weak signal beam is amplified [86, 97–107].

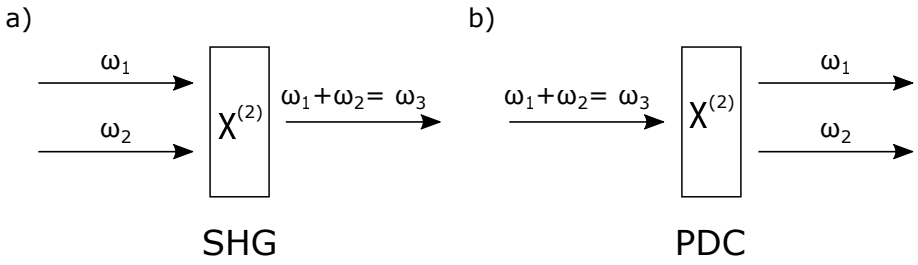

Figure 1.2: **Diagram of SHG and PDC frequency conversion.** Diagram of a) Second Harmonic Generation (SHG) in which a pair of low frequency photons of frequency ω_1 and ω_2 are upconverted into a single high frequency photon of frequency ω_3 within a $\chi^{(2)}$ non-linear crystal and b) parametric amplification, the time-reversed complement of SHG in which a single high frequency photon of frequency ω_3 is downconverted into a pair of low frequency photons with frequencies ω_1 and ω_2 within a $\chi^{(2)}$ non-linear crystal. Both processes are subject to conservation of energy and therefore $\omega_1 + \omega_2 = \omega_3$ in the case of a single frequency conversion process.

Stimulated emission, however, is not desirable in the case of quantum optics and quantum imaging experiments in which each photon-pair is required to be independent of all others. This independence requires that $n \ll 1$ photons per mode are generated for the coupled signal and idler modes. This is to ensure that each of the individual photon-pairs are generated independently of other photon-pairs in time and are therefore correlated as each pair is then independently subject to energy and momentum conservation laws as they are simultaneously generated [108, 109]. The independence of the photon-pairs is important in systems that rely on entanglement as this means that there is an uncertainty in the state of the photons and therefore in order to achieve this the spontaneous emission of fluorescence is required. The spontaneous annihilation of a pump photon and the creation of the signal and idler photons may be interpreted as energy being transferred into resonant modes of the system via zero-point fluctuations in the modes of the signal and idler which are coupled due to energy and momentum conservation laws [85, 110–117]. The conversion efficiency for the combination of frequencies of the pump, the signal, and the idler photons is dictated by the Manley-Rowe relations for non-linear systems [118, 119]. This spontaneous emission has also been interpreted as the quantum noise of a linear (phase preserving) amplifier [120]. A parametric process, such as that described here, is one in which the final quantum mechanical state of the system is identical to the initial quantum mechanical state. Such processes utilise virtual energy levels which exist as a result of the uncertainty principle. [88, 121]. In a parametric process the angular frequencies of the pump

(ω_p), signal (ω_s), and idler (ω_i) photons are related as per equation 1.5 due to the principle of the conservation of energy. Spontaneous Parametric Down-Conversion (SPDC) is the name given to this spontaneous parametric process in which a single pump photon is downconverted into an entangled photon-pair consisting of the signal and the idler photons. SPDC was observed a short time after the aforementioned works that detailed the underlying theory [122–125].

$$\omega_p = \omega_s + \omega_i \tag{1.5}$$

The process of SPDC emission of photon pairs is dependent on meeting the phase matching conditions through the appropriate configuration of the crystal, such that energy is transferred from the pump beam to the downconverted beams. This process is subject to momentum conservation as per equation 1.6 in which the wavevectors for the pump, signal, idler photons represented as ($\mathbf{k_p}$), ($\mathbf{k_s}$), and ($\mathbf{k_i}$) respectively [126, 127]. In order for the phase-matching condition to be achieved the phase of the pump, signal, and idler must be in-phase through the length of the crystal [85, 126, 127].

$$\vec{k_p} = \vec{k_s} + \vec{k_i} \tag{1.6}$$

Should the phase matching condition be met the downconverted photon-pair may be emitted in a collinear fashion in which the signal and idler photons are emitted in an identical direction to the pump as in figure 1.3a or non-collinear fashion in which the signal and idler are emitted with a transverse momentum that is equal in magnitude and opposite in direction as in figure 1.3b. In the case of non-collinear phase matching there exists a longitudinal wavevector mismatch Δk_z in the direction of pump propagation, this mismatch is related to the emission angle θ of the photons relative to the direction of propagation of the pump. In the near-collinear regime that is used in the work presented here the range of angles over which the downconverted photons are emitted is $L\Delta k_z \lesssim \pi$ for a crystal of length L. It follows that the emission angle θ is related to the wavevector mismatch Δk_z by equation 1.7 [128]. The efficiency of the downconversion process is also somewhat dependent upon the wavevector mismatch and is scaled by $sinc^2(L\Delta_z/2)$ [128]. For near-degenerate downconversion this value is close to unity and the rate of downconversion

R_{SPDC} is of the order 10^{-8} and scales as in equation 1.8 [129]. In which $d_{eff} = \frac{1}{2}\chi^2_{eff}$ is the effective coefficient for nonlinear interaction, P_p is the pump power, and L_z is the length of the downconversion crystal [121].

$$\Delta k_z = k_p - 2cos(\theta)k_s \approx (\frac{\theta^2}{2})k_p \tag{1.7}$$

$$R_{SPDC} \propto d^2_{eff} P_p L^2_z \tag{1.8}$$

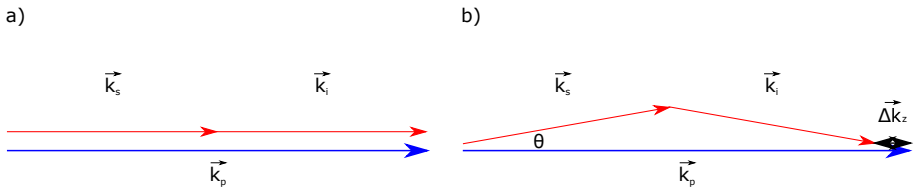

Figure 1.3: **Diagram of collinear and near-collinear phase matching** Diagram of phase matching. a) collinear phase matching in which the wavevectors $\vec{k_i}$ and $\vec{k_s}$ are collinear with the pump $\vec{k_p}$. b) near-collinear phase matching in which the downconverted signal and idler are nearly collinear with the pump but for which a small momentum mismatch vector $\vec{\Delta k}$ exists.

As SPDC represents a three-wave mixing process, there are waves of three different frequencies in the case of non-degenerate downconversion or two different frequencies in the case of degenerate downconversion that need to be phase matched throughout the crystal. In degenerate downconversion the downconverted signal and idler photon frequency spectra are centered on the same frequency $\omega_s = \omega_i = \omega_p/2$, whereas in non-degenerate downconversion the central frequencies of the signal and idler photon frequency spectra can differ so long as the combination of frequencies obeys the principle of energy conservation. The successful phase matching of two or three waves of differing frequency throughout the non-linear crystal is dependent on the refractive index of the material at the different frequencies represented as per equation 1.9. In order to achieve this phase matching condition birefringence is often utilised to compensate for the effects of chromatic dispersion.

$$\frac{n(\lambda_p)\omega_p}{c} = \frac{n(\lambda_s)\omega_s}{c} + \frac{n(\lambda_i)\omega_i}{c} \tag{1.9}$$

Birefringence is a property of materials where the refractive index is dependent not only on

the wavelength of the light, but also on its polarisation. In the work presented in this thesis a β-barium borate (BBO) crystal (a negative uniaxial crystal that exhibits birefringence [130]) is used as the downconversion source and the phase matching condition is tuned by rotating the crystal. Rotation of the downconversion crystal serves to alter the angle between the polarisation of the incoming pump beam and the optic axis of the crystal thereby altering the magnitude of the components of polarisation of the linearly polarised pump, signal, and idler that are parallel to the ordinary and extraordinary axes of the crystal [88, 131]. For uniaxial crystals the ordinary and extraordinary axes are defined relative to the their optic axis of the crystal [88]. The ordinary axis defines the polarisation perpendicular to the plane that contains the optic axis of the crystal and the propagation vector of the pump beam k_p and which is subject to refractive index n_o. The extraordinary axis defines the polarisation in the plane that contains the optic axis of the crystal and the propagation vector of the pump beam k_p and which is subject to refractive index n_e. The phase-mismatch vector can be changed by rotating the optic axis of the crystal relative to the incident pump beam [88, 91, 106, 123, 125, 130, 132, 133], or by altering the temperature of the crystal also results in an altered fluorescence spectrum [122, 125, 134–139]. A number of works have been written regarding the modelling the SPDC process in greater detail [128, 140–143]. Work has also been performed in looking at methods to create photonic crystals of differing geometry and materials in order to improve conversion efficiency [144] and to allow photon-pairs with greatly different frequencies to be generated [145].

There exist two types of phase matching for SPDC within a nonlinear crystal with ordinary (o) and extraordinary (e) polarisation axes, these are labelled type-I in the case in which the two downconverted beams are parallel to one another and orthogonal to the pump beam ($e \mapsto o + o$ or $o \mapsto e + e$), and type-II in the case in which the two downconverted beams are orthogonal to one another ($e \mapsto e + o$ or $o \mapsto e + o$) [126]. In SPDC from type-I phase matching, the photon-pairs are emitted on a single cone with opening angle defined by the angle between the crystal optic axis and the direction of propagation of the pump beam, with the photon-pairs emitted opposite to one another about the pump beam in order to ensure transverse momentum conservation [146–148]. In the case of non-degenerate emission, the two photons are emitted with frequencies that are symmetric about the degenerate frequency but with angles that are non-

symmetric [149]. In SPDC from type-II phase matching the signal and idler form two spatially separated beams whose overlap can be modified by adjusting the angle between the crystal optic axis and the direction of propagation of the pump beam. This separation is due to the crystal birefringence [146,148]. The differences in the form of the emission for type-I and type-II SPDC is shown in figure 1.4. As in the case of SPDC from type-II phase matching the birefringence of the downconversion source can lead to walkoff effects as waves of differing polarisation diverge. This effect increases as the length of the crystal increases [88]. In the far-field of the downconversion crystal the signal and idler beams may be seen as a beam or an annulus. The width of this annulus is proportional to the bandwidth of the emitted photons. This bandwidth is linked to the length of the downconversion crystal because the phase matching condition can be met across a greater range of frequencies as the length of the downconversion crystal is reduced [128, 147]. The property of birefringence can be approximated in a non-birefringent material by using a downconversion source that has the optic axis of the crystal periodically inverted in order to achieve what is referred to as quasi-phase matching. This is the case for the periodically poled potassium titanyl phosphate crystal (PPKTP) [88]. Downconversion sources can use quasi-phase matching to generate SPDC using a type-0 downconversion source. For type-0 phase matching the two downconverted beams are parallel to one another and to the pump beam ($o \mapsto o + o$ or $e \mapsto e + e$) [88].

The false colour image displayed in figure 1.5 shows SPDC from a downconversion source with type-II phase matching with a bandwidth that encompasses the three exposures taken with 5 nm wide filters centered at 681 nm, 702 nm, and 725 nm [150]. It may be seen that the blue-shifted photons in one beam are momentum anti-correlated with red-shifted photons in the other beam (shifted relative to the central green frequency in this image) due to conservation of energy and conservation of momentum constraints on the generated photon pairs.

The photon-pairs generated by SPDC are entangled in position, momentum, time, frequency, and also OAM. Correlations between photons from an SPDC source in both the spatial and the temporal domain were first observed by Burnham and Weinberg [109]. Entangled photon-pairs generated via SPDC have been proposed [151–153] and utilised in a number of Bell-type experiments and have been found to violate the Bell inequalities [51, 154–168]. A large body of

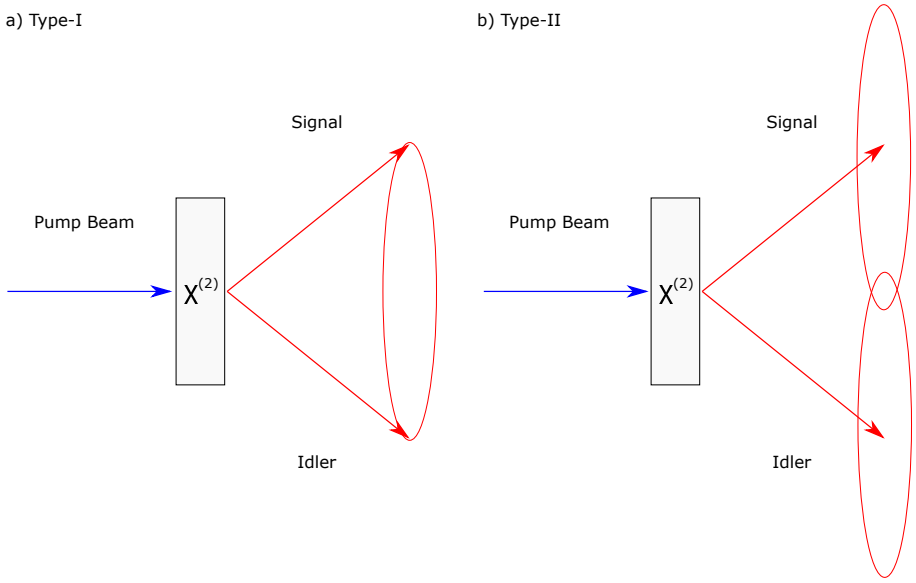

Figure 1.4: **Diagram of the downconverted beams emitted via SPDC in the case of type-I and type-II phase-matching.** Diagram of Spontaneous Parametric Down-Conversion (SPDC) produced by a) Type-I phase matching and b) Type-II phase matching in which the signal and idler beams are spatially separated in the far-field of the crystal. In the SPDC process a single high frequency pump photon is spontaneously downconverted into a pair of low frequency photons within a non-linear crystal. In this diagram non-collinear downconversion is shown and the signal and idler do not co-propagate with the pump beam. The photons are generated in the same location within the crystal and so are correlated in position and because the transverse momentum of the signal and idler photons are equal in magnitude and opposite in direction they are anti-correlated in momentum.

work investigating the strength of the correlations from SPDC sources has been performed with the temporal [109, 169–171], intensity [172], frequency [173], spatial [174–180], and OAM [181–187] correlations being subject to investigation and experiment [72]. The extent of the spatial correlations from a SPDC source and also details regarding the detector technologies used to observe these correlations are described in Chapter 2.

1.5 Quantum-Enhanced Imaging

A reliable source of quantum states of light has not only allowed experiments, such as those described above, to test quantum mechanics to be realised, but has also led to a multitude of different ideas designed to allow the correlated nature of the light source to be leveraged to enhance imaging schemes beyond the classical limit [72, 75, 188–190]. The question that is asked in this work is: how can the spatial correlations between the entangled photon-pairs produced by

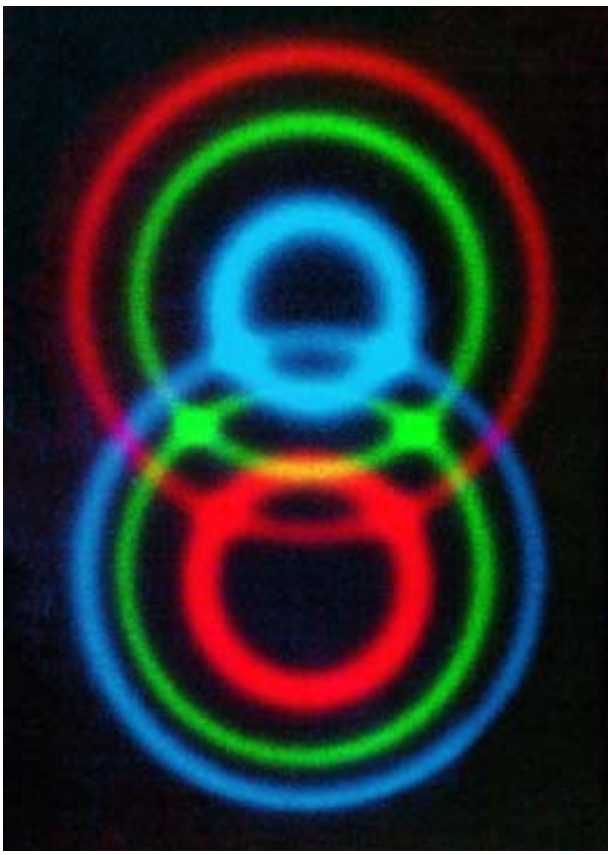

Figure 1.5: **SPDC rings from downconversion source with type-II phase matching** SPDC with a bandwidth that encompasses the three exposures taken with 5 nm wide filters centered at 681 nm, 702 nm, and 725 nm to display the frequency distribution in the downconverted beams. Image from [150].

SPDC be harnessed to ultimately enhance imaging over the corresponding classical case? Here a brief overview of some quantum imaging schemes which utilise the spatial correlations between SPDC photon-pairs will be presented alongside their corresponding classical analogues thereby allowing a comparison of the different implementations to be made and the advantages of implementing quantum schemes to be presented. Presenting these prior works will describe the unique advantages that quantum imaging schemes have over corresponding classical schemes and will allow the experimental work presented in Chapters 3, 4, and 5 to be represented in the context of quantum imaging works performed to date.

The first implementation of an imaging scheme that utilised these spatially correlated photon-pairs employed single photon avalanche photodiodes (SPADs) as the detector of choice [191–193]. However, using such non-spatially resolved detectors (referred to as bucket detectors) requires that they be used in conjunction with some form of raster scanning or computational

structured illumination techniques which thereby renders imaging applications, or any application that requires using spatial correlations, time-inefficient [75,194]. Scanning techniques were employed by Pittman et al. (1995) in realising a quantum ghost imaging setup (as proposed by Klyshko [195]) that employed SPDC as a source of spatially correlated photon-pairs to perform coincidence detection of photon events between a pair of SPADs in two spatially separated arms [191]. More recent implementations of quantum ghost imaging use a single bucket detector in the idler arm to herald a single photon sensitive array detector in the signal arm and such setups are capable of acquiring a ghost image in a matter of hours [65,196,197,197–199]. These more recent realisations of ghost imaging setups use a spatially resolved detector in the signal arm to enable imaging across the full field of view without limitations imposed by the number of pixels through which a scanning detector must separately measure which limits efficiency to $1/n$ for n pixels [196–198]. Ghost imaging is not a purely quantum phenomenon [200] and has classical analogues in the form of pseudo-thermal ghost imaging or computational ghost imaging which rely on correlated light fields [201–211]. Unlike the case of quantum ghost imaging for which the contrast may reach a value of 1, in the case of classical ghost imaging the achievable contrast is limited to $1/2$ [212]. This limitation is due to the spatial extent of structured light features although this can be compensated for by performing background subtraction techniques [205, 212, 213]. There are also limits in the achievable SNR for classical ghost imaging when compared to quantum ghost imaging at low light levels (< 1 photon per pixel per frame) [214]. However, in the case of quantum ghost imaging there is the possibility to use non-degenerate downconversion to allow the imaging of an object at wavelengths for which array detectors are unavailable or their use unfeasible due to cost, operational temperature requirements, or available spatial resolution. Such a quantum ghost imaging experiment was performed by Aspden et al. (2015) in which an object was interrogated by infra-red photons at 1550 nm and the image was collected by detecting visible photons at 460 nm using an array detector [198]. Other implementations of ghost imaging using non-degenerate photon-pairs produced by SPDC have been demonstrated [215, 216]. Should the differences in the wavelengths of the downconverted photon-pairs be engineered such that the signal wavelength lies in the THz waveband and the idler in the visible then THz ghost imaging may be realised [217, 218]

or potentially for ghost imaging using x-rays [219–221]. Quantum ghost imaging of objects by reflection [222] and through turbulent media [223] have also been performed thereby demonstrating strengths of such an imaging scheme. Quantum ghost imaging also allows interaction free detection to be implemented using a quantum scheme [224, 225]. In an interaction free detection scheme, an interferometer is constructed and a detector placed at the output port tuned for destructive interference. Should an object be placed into one of the arms and a photon detected by the detector located at the port tuned for destructive interference, then the photon may be said to have not interacted with the object, however, the object is still detected without the photon being lost [226–234]. Interaction-free ghost imaging has further advantages over quantum ghost imaging in that a comparable SNR can be achieved for a lower photon-flux and may therefore have applications in low-light level imaging in which limiting photon absorption is vital [224, 225]. A thorough review of quantum and classical ghost imaging can be found in Moreau et al. (2017) [194] and Shapiro and Boyd (2012) [211].

A further extension of quantum ghost imaging is imaging with undetected photons in which the idler photon need not even be detected in order to image the object with which it interacts [235–237]. This is achieved by pumping a second non-linear crystal and feeding the idler beam from the first non-linear crystal into it and then overlapping and interfering the two indistinguishable signal beams to obtain information regarding the object probed by the undetected idler photons. Pumping the second non-linear crystal with the idler beam from the first non-linear crystal serves to induce coherence in the emitted idler beam, which by extension means that the two signal beams generated in the first and second crystal are coherent [238–241]. This induced coherence is the result of the superposition of the idler waves within the second non-linear crystal which makes their source indistinguishable and by extension induces coherence. Placing an object into the idler beam from the first non-linear crystal and before the second non-linear crystal and then interfering the signal beams allows an object to be imaged using the idler photons that remain undetected as the phase and transmission properties of the object are transferred to the signal beam emitted by the second non-linear crystal by the the idler beam from the first crystal that has interacted with the object. The visibility of the quantum interference between the two signal beams is limited by the indistinguishability of the signal beams at

the beamsplitter. This may be reduced by the object placed in the idler beam having a finite absorption which reduces the coherence between the two signal beams thereby introducing some distinguishability and reducing the visibility [240, 242]. Imaging with undetected light has been experimentally demonstrated in the non-degenerate case in which the object was probed by the idler beam at 1515 nm and the signal beams that are interfered and detected by the camera are at 820 nm [235]. Imaging with undetected photons presents an advantage over quantum ghost imaging as no detector is required at the wavelength of the idler beam which probes the object. However, there are drawbacks in applying this technique due to it being an interferometric technique and therefore the complexity of the system and its susceptibility to mechanical and thermal noise is increased. Such a setup has applications beyond imaging and has been used to measure correlations between photon-pairs [243, 244]. Induced coherence from a signal beam may also be found in the stimulated emission regime [245, 246]. A classical analogue of this technique also has been demonstrated and has been theorised to be able to outperform the quantum scheme with regards to contrast and SNR even for objects of low transmittance [247, 248].

As alluded to in the above discussion on ghost imaging, quantum enhanced imaging possesses advantages over classical schemes in imaging at low light levels. Imaging under such illumination conditions are required when interrogating biological samples sensitive to large photon fluxes through heating or photochemical effects [249, 250] or when operating for the purposes of certain security and defence applications for which covert observation may be a requirement. However, when imaging under a low photon flux the presence of detector and background noise presents a problem as these noise sources become evident and degrade the resulting image. Furthermore, the shot noise on N detected events is equal to $\sqrt{N}$ and therefore as the number of detected signal events is reduced towards zero then the signal can become lost in the noise on the signal. The presence of noise in an image degrades its quality and reduces the information that can be extracted from it. An imaging method that is capable of rejecting noise while keeping information regarding the scene that is being imaged would allow low light level imaging to be readily applied. The signal and idler beams that comprise the photon-pairs generated by SPDC are subject to the same intensity fluctuations and therefore sub-shot-noise behaviour may be observed in the intensity correlations between the two

beams [149, 251–256]. The presence of intensity correlations allows some of the noise resulting from intensity fluctuations in the beam used to probe the object to be removed and an improved estimate of the probed object absorption to be made relative to what could be achieved using a classical scheme [253, 257]. Due to the presence of spatial correlations between the downconverted photon-pairs the intensity fluctuations at a given position within the beams are correlated thereby allowing sub-shot-noise imaging methods to be applied to imaging weak amplitude (low absorption) objects [188, 258, 259] and weak phase objects [260]. A sub-shot-noise imaging scheme has been applied in the context of a wide-field microscope [261]. Sub-shot-noise imaging allows the imaging of low-absorption objects for which the correlations between the two beams are maintained, in the case of increased absorption the quantum advantage in using the sub-shot-noise statistics will be lost [262]. Other metrics used to estimate the absorption of objects that use a combination of all the detected events (both quantum correlated and also uncorrelated), show a quantum advantage for objects presenting absorption of up to 50% at the probe wavelength and have been demonstrated in an imaging context where the two beams are detected using a CCD camera [262, 263].

Sub-shot-noise imaging techniques are used to remove noise sources that are not correlated with the intensity fluctuations within the downconverted beams. However, as is the case with many quantum enhanced imaging schemes, they rely on the utilisation of quantum proprieties after the target object has been probed and as a result are sensitive to the effects of decoherence. Decoherence presents itself via the introduction of environmental noise and losses and leads to the severe degradation of any quantum enhancement [75, 264]. This is the case for many quantum imaging schemes which are limited in their scope to imaging under low-noise and high-detection efficiency (low loss) conditions, and to the sensing of low-absorption target objects. Such limitations prevent the application of many of these schemes in real-world environments as the quantum enhancement is minimised or lost. Quantum illumination protocols allow a quantum advantage to continued to be realised in the presence of environmental noise and losses. The noise sources that background light and sensor noise represent serve to reduce the resulting image contrast. To overcome this degradation of image quality in the presence of background light and sensor noise, quantum illumination protocols have been theorised [265–267] that ex-

ploit the correlations between entangled photon-pairs. A communications protocol proposed by Mandel (1984) [268] describes the principle of using correlations between photon-pairs to effectively discriminate the presence of a signal within a high background events and that the signal could be hidden within the background in order to make the signal interception-proof. A similar approach with regards to quantum ranging and imaging led to the development of the quantum illumination protocol by Lloyd (2008) [265] that would be capable of outperforming classical schemes of the corresponding energy. The quantum illumination protocol was then generalised to Gaussian states by Tan et al. (2008) [266]. This generalisation showed that the quantum illumination protocol in which the thermal noise background is treated as being in a Gaussian state and the entangled signal and idler photon-pairs treated with quantum statistics demonstrates an advantage of 6 dB in the error probability relative to the optimal coherent state system thereby allowing a practical version of the quantum illumination protocol to be designed. The resulting enhancement in the performance of the quantum illumination scheme over the corresponding classical illumination scheme increases as the levels of noise and losses in the imaging system increase. Further work in developing the quantum illumination protocol describes how to ascertain the presence of a target object within a noisy and lossy environment that destroys the initial entanglement between the photon-pairs [267, 269–273]. This is possible due to classical states not being able to replicate the output state of entangled photon-pairs and therefore these entangled photon-pairs may still be distinguished despite the presence of losses [266, 270, 271]. The quantum illumination protocol has been demonstrated by Lopaeva et al. (2013) [274–276], to determine whether a semi-transparent object (in this case a beamsplitter) is either present or absent, through the exploitation of detected intensity correlations which originate from spatially correlated photon-pairs in the presence of an uncorrelated thermal light source. That demonstration was restricted to the detection of the presence or absence of a target object as opposed to performing imaging. In the context of imaging, England et al. (2019) [277] demonstrated the quantum illumination protocol using spatially correlated photon-pairs and raster-scanning of the object within the single-mode probe beam. Quantum illumination protocols have also been implemented in full-field imaging schemes [278, 279]. Quantum illumination protocols have also been demonstrated in the near-infrared regime using the spectro-temporal correlations

between entangled photon-pairs [280]. Beyond the field of imaging, quantum illumination has applications in the field of quantum metrology [281], quantum information and communications protocols for secure communication [268, 282, 283] as such a protocol may serve to secure communication against passive eavesdropping techniques that leverage the presence of noise and losses inherent in the system. Further proposals to apply quantum illumination in the microwave domain with respect to the development of quantum radar have also been made [284–286]. Another method that use the properties of photon-pairs to reject uncorrelated noise when performing imaging include Heralded imaging in which the temporal correlations between photon-pairs are used to reject technical detector and background noise through time-gating the detector therefore allowing images to be constructed using a reduced number of photons. Heralded detection schemes have been applied in ghost imaging schemes [197], absorption measurement [287, 288], and have been proposed for quantum radar and lidar implementations [284, 289].

Further to quantum enhanced imaging offering advantages in image contrast and background noise rejection, improvements in spatial resolution may also be achieved. In classical imaging systems the achievable spatial resolution is limited by the diffraction limit for an imaging system as investigated by Abbe and Rayleigh [290, 291]. The diffraction limit can also be surpassed through detecting the correlations between N photons which can allow an improvement in resolution of up to $1/\sqrt{N}$ which represents the standard quantum limit (SQL). The SQL can be reached by N-photon detection using both quantum [292, 293], and classical [294–296] light sources. A resolution enhancement scheme that uses a SPDC source of photon-pairs is capable of achieving a $1/\sqrt{2}$ resolution enhancement by performing centroid measurements on the detected photon-pair events. Centroid estimation [297, 298] was originally developed in the context of quantum lithography [299–301] which is a quantum interference technique that is capable of Heisenberg ($1/N$) resolution scaling using NOON states [299]. An implementation using SPDC photon-pairs in which the object is placed in the pump beam allows the pump beam resolution to be recovered by performing centroid estimation on the detected photon-pairs to give an apparent $1/N$ enhancement relative to the expected resolution limit for the wavelength of the downconverted photon-pair has also been achieved [302]. A number of other classical schemes have been developed to allow the diffraction limit to be surpassed including through

the use of computational means [303], the use of fluorescence [304–311], and correlation measurements [312–315]. Other schemes that utilise quantum light sources utilise fluorescence from colloidal quantum dots [316,317], nitrogen-vacancy colour centres within a diamond [318–320], and single-photon emitters [321]. The quantum and the classical have also been combined [322]. Many of these schemes the use of high-light levels or the use of fluorophores and chemical dyes is required, all of which affect the sample chemistry and which also physically move over the time that an image is acquired [310]. A low-light resolution enhanced imaging technique that does not use foreign agents or bodies would allow live samples to be imaged in a manner which does not interfere with their normal operation.

In this chapter an overview was presented of a number of imaging applications for which quantum imaging techniques offer an enhancement over the corresponding classical imaging schemes. However, many of the above schemes also have classical analogues which may initially appear to negate the need to construct complex quantum imaging implementations which are limited by the need to detect quantum correlations. Quantum enhanced imaging schemes come into their own in implementations in which the level of illumination is of concern, perhaps as a requirement of imaging light-sensitive samples or due to operating in a covert scheme that requires illumination and detection under a low photon flux, or in the case of exploiting correlations between non-degenerate wavelengths then classical schemes are unable to perform. The aforementioned experiments that aim to perform quantum enhanced imaging have the potential to improve image quality, however, these demonstrations have largely been confined to the laboratory because the carefully prepared quantum states are sensitive to decoherence and noise. In the subsequent Chapters 3, 4, and 5 work shall be presented that demonstrates how the use of a quantum light source may be used to perform low-light level imaging in non-ideal conditions in the face of external environmental noise which will enable quantum imaging schemes and technologies to be realised in real-world applications. A more broad review of quantum imaging schemes including those detailed here can be found in Moreau et al. (2019) [75].

1.6 Walkthrough

Here I will give a brief introduction to the topics that will be presented in the chapters that follow.

Chapter 2: In this chapter the parts of the experimental setup that are common throughout the experiments peresented in this thesis will be described. The strength of the spatial correlations and the effect of the heralding efficiency will be detailed. The choice of array detector will also be justified.

Chapter 3: In this chapter a quantum imaging scheme that demonstrates a contrast advantage will be described. This work was presented at IONS Scandinavia, Danmarks Tekniske Universitet, Copenhagen, Denmark (2018) and at Quantum Information and Measurement V: Quantum Technologies, Sapienza Università di Roma, Rome, Italy (2019).

Chapter 4: In this chapter the first implementation of a full field quantum illumination protocol will be described. This imaging scheme demonstrates an advantage in the presence of detector and environmental noise and losses. This work was published under the title "Imaging through noise with quantum illumination" in *Science Advances* [279].

Chapter 5: In this chapter an improved quantum illumination protocol is presented. This improvement is achieved through the combination of quantum and classical data. This work was published under the title "Improved Performance Of The Quantum Illumination Protocol By Noise Subtraction" in *Scientific Reports* [323].

Chapter 6: In this chapter methods to extract increased volumes of information from the acquired frames are investigated.

Chapter 7: In this chapter a summary of the work present in this thesis shall be given alongside a discussion of potential future projects that further this work.

Chapter 2

Experimental Methods

2.1 Introduction

Of the work presented in this thesis, there exists a commonality in the experimental methods and apparatus used. Therefore in this chapter that which is common throughout the work presented in this thesis shall be detailed with any deviations particular to any specific experiment discussed in the appropriate chapter. Firstly the downconversion source used to perform the experiments will be described in section 2.2 and then the nature of the correlations generated by SPDC will be detailed in section 2.3. Finally in section 2.4 the detectors used in the experimental work presented here will be described in terms of their underlying technology and how this affects the noise characteristics of the different detector technologies.

2.2 Downconversion Sources

The downconversion sources comprises a BBO non-linear crystal cut for spontaneous parametric downconversion at 710 nm pumped by a laser beam at 355 nm. The laser used throughout the quantum optics experiments is a JDSU xCyte CY-355-150 Nd:YAG laser with 355 nm output at 160 mW with pulse repetition 100 ± 10 MHz and with a pulse width of ≈ 10 ps. The frequency tripling process used to generate the laser light entails taking the output of the Nd:YAG laser at 1064 nm and using appropriately cut χ^2 non-linear crystals to perform first frequency doubling

by second harmonic generation which will generate light at 532 nm and then sum frequency mixing 355 nm [324–326]. As a result the light that is output will consist of lines at 1064 nm and 532 nm in addition to that which we desire at 355 nm. These additional lines must be filtered out from the beam prior to it being incident upon the downconversion crystal in order to prevent the generation of unwanted fluorescence.

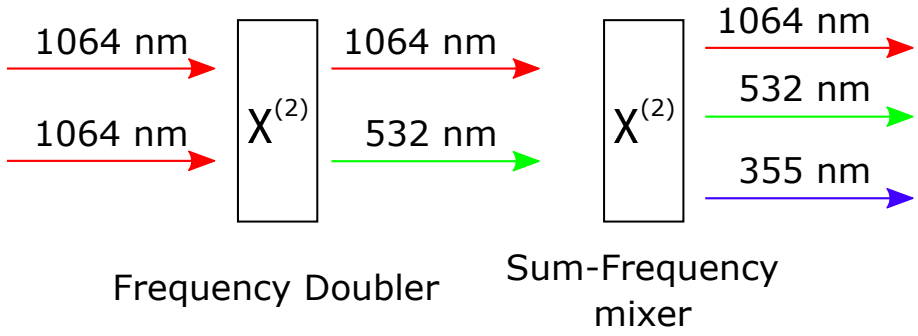

Figure 2.1: **Diagram of the generation of** 355**nm light by an Nd:YAG laser.** The frequency tripling from 1064nm to 355nm is achieved by performing frequency doubling and then sum frequency mixing both of which are SHG processes as described in 1.2.

For the experiments presented in this thesis the optical setup prior to the downconversion crystal is identical and arranged as in figure 2.2. The laser beam is initially spectrally filtered using a cold mirror to remove spurious laser lines that remain from the frequency tripling process and then spatially filtered using a 50 mm 50 μm 200 mm spatial filter to expand the pump beam and collimate it such that a beam with an approximately Gaussian profile of beam waist diameter of $\sim$ 10 mm is incident upon the downconversion crystal. The significance of the size of the pump beam will be discussed in the following section 2.3. A software controlled rotatable half-wave plate is used to rotate the polarisation of the pump beam using birefringent properties of the material. The half-wave plate has, much like the downconversion crystal, different refractive indices along orthogonally orientated axes of polarisation (labelled the fast and slow axes), thereby resulting in a difference in velocity for the components of a light beam which are polarised along each of these axes. Using a half-wave plate the polarisation of the incident beam is rotated through an angle defined as twice the angle between the incident beam's polarisation and the fast (optical) axis of the waveplate. A wire-grid polariser is then used to select the polarisation component that is perpendicular to the wires. The combination of the half-wave plate and a wire-grid polariser allows the intensity of the incident pump beam, and consequently

that of the generated SPDC beams, to be modified. The laser beam is then spectrally filtered using an interference filter centred on 355 nm with a bandwidth of 30 nm (Semrock Brightline FF01-356/30-25), this is in order to filter out background light and any remaining spurious laser lines. After filtering the pump beam spatially, spectrally, and then with regards to polarisation the pump beam is then quite ready to interact with the downconversion source. The downconversion crystal used in this work was a 3 mm thick β-barium borate (BBO) crystal cut for type-II phase matching and degenerate downconversion at 710 nm with a 5° opening angle. Post-crystal a pair of dichroic mirrors (Chroma T455lpxt dichroic mirrors, cut-off wavelength 455 nm, 45° angle of incidence) are located in order to remove the pump beam and transmit the SPDC photon-pairs generated at the degenerate wavelength of 710 nm. Two high-transmission 10 nm bandwidth interference filters are placed before the camera to select the SPDC photon-pairs about the degenerate frequency of 710 nm (Chroma ET710/10m interference filters, 98% transmission at 710 nm).

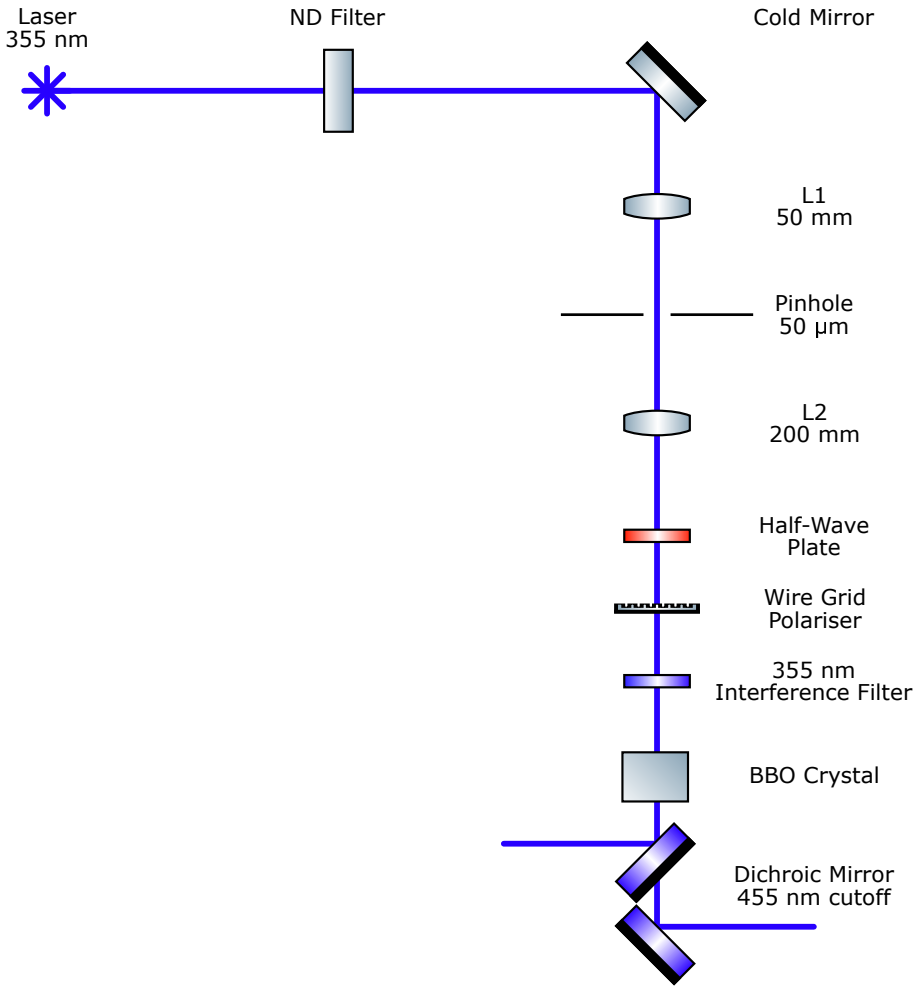

Figure 2.2: **Diagram of the quantum illumination setup pre-crystal.** Prior to interacting with the downconversion crystal the 355 nm pump beam is reduced in intensity and both spatially, spectrally, and polarisation filtered such that a Gaussian beam of appropriate diameter, polarisation, and wavelength is incident on the downconversion crystal.

Observing the downconverted beams in the far-field of the downconversion crystal they are spatially separated owing to the crystal birefringent effects as described in 1.4. In the far-field of the downconversion crystal the downconverted beams form two spatially separated rings that can be expanded or collapsed by adjusting the phase-matching through altering the orientation of the downconversion crystal relative to the pump beam. The width of these rings corresponds to the range of allowed frequencies or equivalently the bandwidth of the system [128]. An interference filter placed onto the camera selects the downconverted photon-pairs about 710 nm with a 10 nm bandwidth. The downconverted beams can have slightly different profiles if the interference filter is not exactly centered at the degenerate frequency. In order to compensate for this a second interference filter is inserted and by tilting it slightly the bandpass is shifted slightly

to lower wavelengths and results in more equally sized beams. Only a slight tilt is appropriate because large angles will not only shift the bandpass but also lead to significant distortion. The combination of two interference filters in this manner serves to narrow the overall bandpass slightly.

2.3 Spatial Correlations

In the work presented in this thesis the spatial correlations between the photon-pairs are of great import and therefore their measurement and theoretical extent shall be described. The photon-pairs are correlated in time as they are generated simultaneously and the correlations have been observed and found to be generated with sub pico-second time intervals [109, 170–172]. This time correlation is limited by the time resolution of the detectors used or the downconverted light bandwidth [169]. The array detectors used in the work presented here have a time resolution of the order of 10 ms but with a photon bandwidth of $\Delta\lambda = 10\,\text{nm}, \tau = 2 \times 10^{-14}$ s the extent of the time correlations is such that the correlated photon-pairs will not be present across frames acquires at different instances of time. This does however, mean that the photon-pairs may not be distinguished from environmental noise by time gating the detector. Spatial correlations have been observed in the form of position correlations in the image plane of the downconversion crystal and as momentum correlations in the far-field plane of the downconversion crystal using single photon sensitive detectors such as APDs and SPADs or an array of few detectors incorporating raster scanning techniques [69, 70, 109, 174, 187, 327–330]. Experiments have also been conducted by implementing compressive sensing techniques, however, reconstruction algorithms can be sensitive to noise [331]. Multi-pixel array detectors allow both full-field imaging and a great reduction in acquisition time to be achieved by parallelised detection through the large number of pixels they possess (around $300,000 - 1,000,000$ pixels), and the development of ICCD (Intensified Charge Coupled Device) cameras and EMCCD (Electron-Multiplying Charge Coupled Device) cameras have allowed spatial correlations between SPDC photons to be observed. The first work reporting the observation of spatial correlations using a spatially resolved detector used an ICCD camera [176]. In that work the resulting images were

somewhat noisy and the results limited due to camera efficiency and dark noise, and as a result some subsequent works operated in a high-gain downconversion regime so as to allow the spatial correlations to be observed more easily. Operating in this regime increases the intensity of the downconverted beams but results in an increased noise level as the beams no longer solely consist of photon-pairs but also consist of higher order correlations. The increased intensity of the PDC beams enabled spatial correlations to be observed using a conventional CCD camera [177], and also using an ICCD camera [176, 332, 333]. In the low-gain regime, that is the regime in which spontaneous emission dominates, the spatial correlations were observed to exhibit sub-shot-noise behaviour when imaging was performed using an EMCCD camera [149] and the correlations have been characterised and the photon-pairs generated by SPDC by both type-I and type-II downconversion have been found to display EPR-type entanglement [179, 180, 334, 335]. The camera technology is such that these EPR-type correlations can be observed in a single pair of EMCCD camera frames of exposure 0.03 s without the need for temporal averaging [336]. The technology and noise behaviour of the single photon sensitive detector arrays that were mentioned above and which were used in the work presented here will be described in section 2.4.

In detecting the photon-pairs incident upon an array detector positioned in the image plane of the downconversion crystal the photon-pairs arrive at the same pixel position as they are generated in the same position within the downconversion source as per figure 2.3a) while in the far-field the photons arrive in anticorrelated pixel positions due to momentum anticorrelations as per figure 2.3b) for type-I downconversion and as per figure 2.3c) for type-II downconversion. These correlations are subject to the constraints described below.

The spatial correlations in SPDC beams are measured by looking at the detected intensity correlations. In the image plane of the downconversion crystal an autocorrelation is performed to assess the correlations, and in the far-field plane of the downconversion crystal a cross-correlation between momentum anticorrelated portions of the downconversion beam(s) is performed. The resulting intensity correlation consists of two components. The first component is the Gaussian pedestal that represents accidental correlations between uncorrelated event-pairs

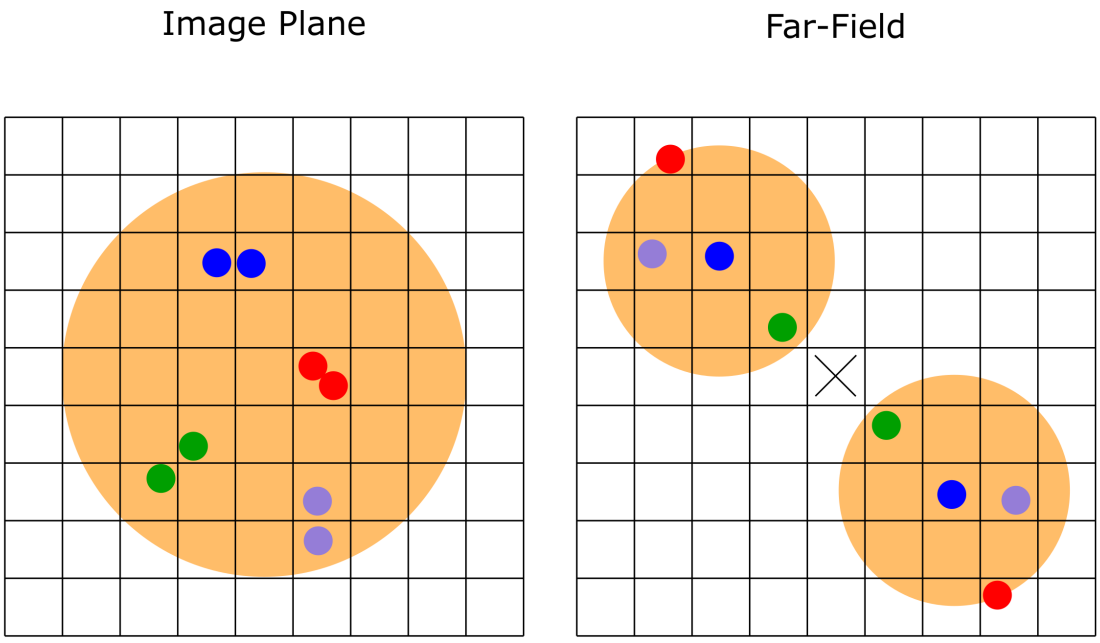

Figure 2.3: **Diagram of the spatial correlations between photon-pair events incident upon an array detector.** Photon-pair events detected in the image-plane of the downconversion crystal are detected close to one another because the photons are generated in the same position within the crystal (left) and in the far-field plane of the downconversion crystal the photon-pairs are detected in diametrically opposite positions to one another because the photons are generated with transverse momenta that are equal in magnitude and opposite in direction. In this figure the colours denote photons that comprise a pair and has no relation to wavelength distribution of photons in the SPDC beams.

as displayed in figure 2.4a) and the second component is the correlation peak that comprises the correlations between photon-pairs as displayed in figure 2.4b) [337]. The Gaussian pedestal is present in the intensity correlation regardless of whether any correlations are present as it represents the distribution of randomly correlated event pairs. These randomly correlated event pairs are present due to random correlations between detector noise events, environmental noise events, and downconverted photon-pairs subject to one of the pair being subject to losses. The volume of the correlation peak is equal to twice the average number of real photon-pairs $\langle N_p \rangle$. The volume of the Gaussian pedestal is $\langle N_t \rangle^2 + \langle N_t \rangle$ in which $\langle N_t \rangle$ is the average total number of events in the frames.

An example of a correlation peak calculated from $250,000$ real EMCCD camera frames is presented in figure 2.5. As the number of frames analysed is increased the noise that is evident on the Gaussian pedestal portion of the correlation peak is reduced as it is averaged out. The

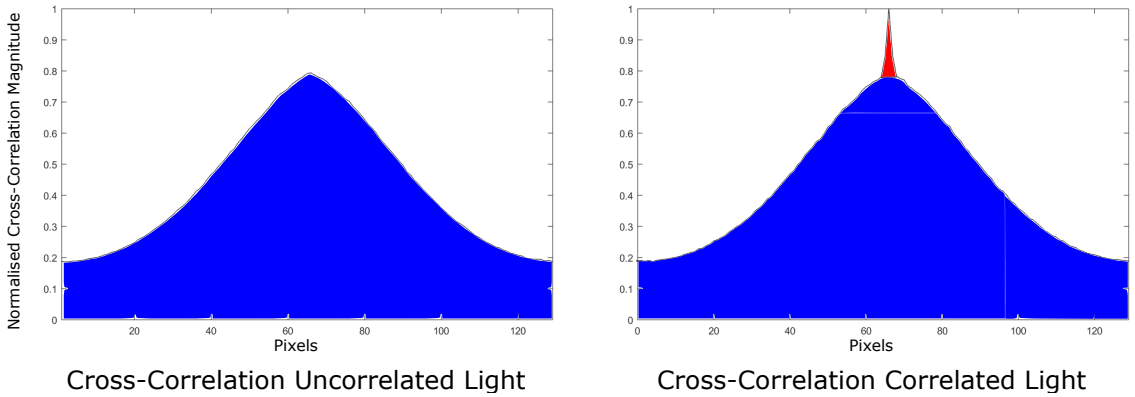

Figure 2.4: **Diagram of a correlation peak from simulated data.** Diagram showing the components of the correlation peak obtained by performing a cross-correlation between two simulated SPDC beams that are a) uncorrelated and b) correlated. In the case of the two beams exhibiting spatial correlations there exists a correlation peak (coloured red) that sits atop the Gaussian pedestal (coloured blue). The Gaussian pedestal is the result of performing a cross-correlation on a distribution of randomly correlated events which is equivalent to the case of uncorrelated beams. The uncorrelated data is calculated by taking the two regions of the array that the cross-correlation is performed on from subsequent frames.

size of this peak has been calculated to have an average FWHM of $\sigma = 3.51 \pm 0.12$ pixels.

The size of the detected correlation peak is limited by the strength of the transverse spatial correlations between the signal and idler photons. For near-collinear and near-degenerate downconversion the strength of the correlations can be approximated in a simple manner using the near-paraxial approximation and assuming near-uniformity of the refractive index of optical materials for narrow frequency bands [121].

In the image plane of the downconversion crystal the strength of correlations represented in equation 2.1 is dictated by λ_p the wavelength of the pump beam and the length of the downconversion crystal L due to divergence of the downconverted photon-pairs generated at different points within the crystal [180, 194, 338]. $\alpha = 0.455$ is a constant to account for approximations made in the calculation [121, 142, 180, 335, 339].

$$\sigma_{x,y} = \sqrt{\frac{\alpha L \lambda_p}{2\pi}} \tag{2.1}$$

In the far-field of the downconversion crystal the uncertainty in the momentum of the downconverted photon-pairs results from the uncertainty in the transverse momentum of the pump beam. The relationship strength of transverse momentum correlation is presented in equation

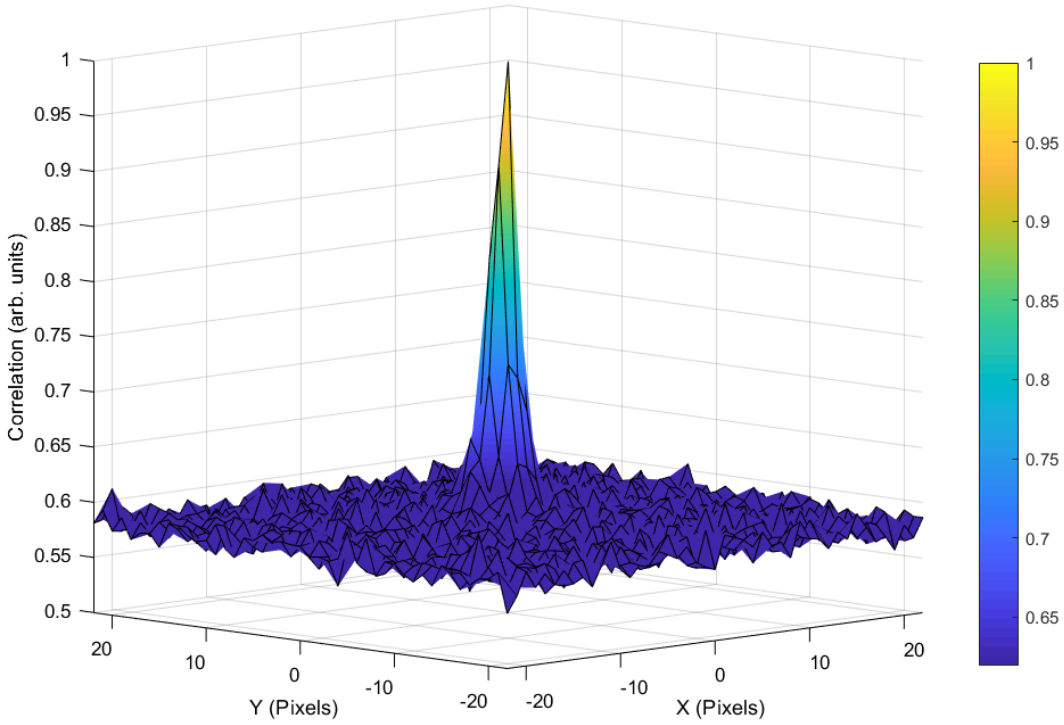

Figure 2.5: **Diagram of a correlation peak from experimental data.** Diagram of the correlation peak calculated from 250,000 frames for an experiment setup in a type-II configuration. The detected SPDC illumination level was set at ~ 0.0016 events per pixel per frame.

2.2 and is dictated by w_p the size of the pump beam, k_p the momentum of the pump beam, f the focal length of the lens used to perform the Fourier transform from the output plane of the crystal [194, 338, 340]. The spread in the momentum uncertainty of the downconverted photon-pairs is inversely proportional to the width of the pump beam w_p, for this reason when utilising correlations in the far-field a pump beam with a large beam waist and using a short focal length lens is desirable.

$$\sigma_{p_x,p_y} = \frac{4f}{k_p w_p} \tag{2.2}$$

These approximations have been shown to determine the size of the correlation peak by numerical simulation [121, 142, 341]. The actual detected width of the correlation peak may be larger than the theoretical size due to the limited numerical aperture of the optical system,

defocus effects, optical aberrations, and also due to the finite width of the spectral bandpass which allows an increased range of frequencies that have different angles of emission thereby leading to broadening of the correlation peak [334]. This enlargement of the correlation peak as a result of accepting a finite range of frequencies is due to accepting an increased range of wavevectors for which there is an increased mismatch wavevector $\Delta\mathbf{k}$ [334, 342].

2.3.1 Poissonian Statistics

The photon-pairs generated by SPDC are independent of one another due to the spontaneous nature of the process as described in section 1.4. As a result of the time independence the generation of the photon-pairs is Poissonian in nature [121]. The detection of the photons is also governed by Poissonian statistics and therefore limited by shot-noise. The detection of photons in a classical beam is limited by the shot-noise which for the detection of N photons the standard deviation is equal to the $\sqrt{N}$ [129]. This shot-noise limit is the limiting level of intensity fluctuations for a coherent state which represents an ideal laser beam. In practice due to noise in both the source and the detector, the detected statistics will be above the shot-noise limit. In the case of a thermal or chaotic source the statistics may well be far above the shot-noise limit because the mean number of photons N itself is also subject to variations in time. Quantum states can be distinguished from classical states by the statistics because, although the signal and idler beams exhibited by SPDC when detected individually exhibit Poissonian statistics, sub-shot-noise statistics may be observed in the correlations between the beams [149, 251–256]. This correlation may be assessed by measuring the joint fluctuations in the correlated regions of the SPDC beams as the intensity in these correlated regions will fluctuate in the same manner with respect to time so the difference in the detected intensities of the correlated regions will tend towards zero but are still subject to noise from external sources and the detector so this limit may not be reached [75]. The sub-shot-noise nature of SPDC beams has been demonstrated [149, 258, 343] and has also been shown in the high-gain regime that the PDC beams exhibit sub-shot-noise behaviour [254–256, 332, 333, 344–347]. The sub-shot-noise nature of SPDC beams has also been applied in the context of imaging [258].

This sub-shot-noise nature of SPDC beams is demonstrated for our experimental setup in figure 2.6 below. This nature is quantified by calculating the degree of correlation between the SPDC beams. The degree of correlation between the two regions of interest (here labelled A and B) is presented in equation 2.3. This value is calculated as the ratio between the variance of the difference in the number of events registered in regions A and B, and the average of the sum of events registered in these two regions. This value is calculated for blocks of 50 frames for a total of 25,000 frames in an illumination regime where the rate of thresholded events is ~ 0.15 events per pixel per frame. The shot-noise limit corresponds to a degree of correlation of $\sigma = 1$ shown by the black line in figure 2.6.

$$\sigma = \frac{Var(A-B)}{\langle A+B \rangle} \tag{2.3}$$

For uncorrelated signal and idler beams (represented by blue points) the average degree of correlation is above the shot-noise limit, whereas for correlated signal and idler beams (red points) the average degree of correlation is below the shot-noise limit. This result indicates that the use of correlated light enables noise reduction below the shot-noise limit which presents an advantage in applications such as sub-shot-noise imaging [258] and shadow sensing [348]. The average degree of correlation for correlated signal and idler beams is 83% and therefore the quantum efficiency of the experimental setup is determined to be 17% as the quantum efficiency $QE = 1 - \sigma$ [258, 343, 348]. This data was obtained prior to the insertion of the non anti-reflection coated microscope slide slip cover that is in the setup for the data presented in Chapters 4 and 5.

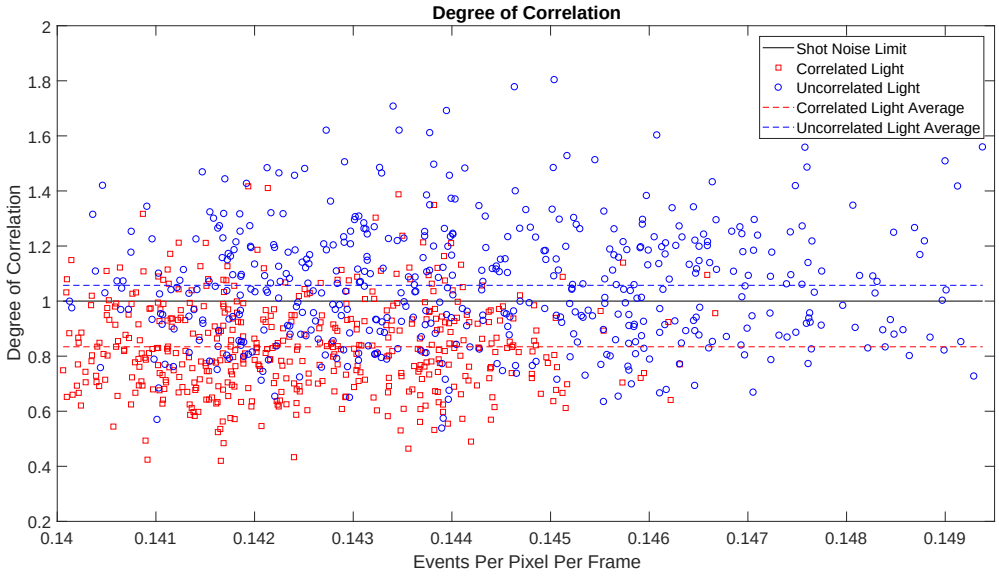

Figure 2.6: **Plot of the degree of correlation for the experimental setup.** Plot of the degree of correlation for the experimental setup. Points representing correlated light are in red while those representing uncorrelated light are in blue. Mean values are represented by the dashed lines in their respective colours and the shot noise limit where $\sigma = 1$ is shown as a black line.

2.3.2 Klyshko Advanced Wave Picture

The strength of the spatial correlations between the signal and idler beams generated by SPDC is affected by the optical system through which the two beams are transmitted. The strength of the correlations can be calculated from the two-photon wave function [70, 349] but can also be determined from a classical geometrical argument [195,350]. The Klyshko Advanced Wave Picture (AWP) was originally developed with regards to ghost imaging type experiments in which the signal and idler beams are separated into different arms and detected using single photon sensitive detectors as displayed in figure 2.7a). In the AWP one of the detectors is replaced by a source which serves to mimic back propagation of the signal beam back through the signal arm of the optical system towards the downconversion crystal which acts as a mirror (should the phase matching condition is met) and reflects the beam into the idler arm towards the idler detector as displayed in figure 2.7b). The detected intensity at the signal detector in this arrangement is then proportional to the rate of correlations in the two detector configuration for detecting SPDC correlations. The AWP has been demonstrated in ghost imaging experiments and is a common method alignment in systems in which the SPDC beams are separated into

separate arms [191, 193, 351, 352]. The AWP is also valid in theory for experiments in which both beams pass through an identical optical system and are detected on an array detector, it is not a practical alignment tool. While the AWP is not directly applied in the alignment of the experimental systems presented in this thesis, it remains of interest as familiarity with the AWP allows intuitive understanding of the experimental results for the quantum enhanced imaging experiments utilising SPDC that are presented here. The AWP is an application of the retrodictive property of quantum systems in which the state of a quantum system may be back-propagated from the measured state of the system [353–356] and may also seen by applying predictive quantum theory combined with Bayesian methods [357].

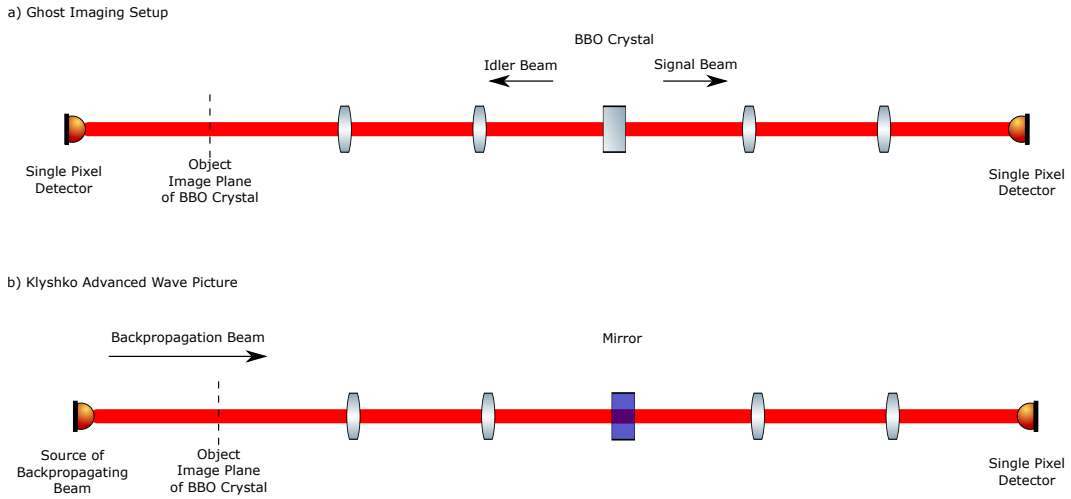

Figure 2.7: **Klyshko Advanced Wave Picture applied to ghost imaging.** a) A standard ghost imaging configuration in which the signal and idler beams generated in the downconversion crystal are separated into two different arms and detected using two separate detectors. b) Klyshko Advanced Wave Picture in which one of the detectors is replaced by a light source and the BBO crystal acts as a mirror.

2.4 Detector Technologies

While the theoretical extent of the spatial correlations between SPDC beams may be determined from the equations presented in the preceding section of this chapter, in order to utilise these correlations detectors that are capable of detecting single photons are required. In a bright light regime with conventional scientific cameras the spatial correlations between the SPDC beams can be observed [177, 332, 333], however, such cameras are not sensitive enough to detect single

photons. Therefore, schemes that utilise correlations between single pairs of photons may not be realised using such detectors. This is due to the noise level being such that there are always a number of electrons in each of the CCD pixel wells even when the sensor is cooled. As a result the single photo-electron released by a single photon striking the detector will not be observable above the underlying technical noise of the camera thereby restricting the extent of quantum behaviour that may be observed using such technology [75].

The detection of single photons, and by extension individual photon-pairs, allows spatial correlations to be utilised in imaging applications. Two technologies based on using CCD array detectors were developed which enable the detection of a signal resulting from the incident of single photons. These two technologies are Electron-Multiplying CCD cameras and Intensified CCD cameras and both will be described in detail in the remainder of this chapter. The use of array detectors allows parallelised detection to be employed thereby offering improved time-efficiency over pinhole scanning techniques which were initially employed in the detection of spatial correlations using single element detectors such as SPADs [156, 192, 358]. More recently small numbers of SPADs have been combined and used as spatially resolved array detectors [359–364]. SPAD array detectors will likely replace the EMCCD and ICCD cameras used in the work presented here as the noise levels, sensitivity, and readout speeds of SPADs can be much improved over CCD technologies. Quantum correlations have been observed using SPAD arrays [365, 366]. The one factor in which they remain deficient is in the fill-factor, that is the ratio of a pixel's light sensitive area to its total area, but this is improving with SPAD array detectors of up to 61% fill-factor now being reported [363]. In the experimental work presented in this thesis EMCCD and ICCD detectors were employed and hence, these technologies will be described here, as will their respective advantages with regards to noise behaviour.

2.4.1 EMCCD Cameras

An Electron-Multiplying CCD camera (EMCCD) differs from standard CCD Camera technology in that it offers a high quantum efficiency which allows single-photon detection and photon counting to be performed [178, 367]. In a standard CCD sensor a photon striking the silicon detector releases electrons that are stored within a potential well, each potential well that com-

prises a pixel of the detector array is read into a readout register by applying a voltage to move the charge in each pixel vertically into the readout register then horizontally to the output. EM-CCD technology has an additional gain register prior to the CCD readout electronics which serves to amplify the electrons stored within the potential wells prior to readout which prevents the readout noise from the output amplifier from also undergoing amplification [368–370]. This additional gain register allows amplification of photo-electrons originating from single-photons to rise above the readout noise floor of the camera [367]. At each stage of the amplification process the electrons in the EM gain register potential wells are accelerated under a high voltage into the next potential well in the register and at each stage there is a probability of an impact ionisation of $0.01-0.015$ which for 600 stages in the gain register results in an overall amplification of the signal by $\sim 400-7600$ [178]. The amplification prior to readout can allow single photon events to be detected by allowing them to rise above the readout noise floor of the camera [367]. However, it must be understood that in the case of the EMCCD camera the amplification process serves to amplify all of the electrons present in each of the CCD pixel wells regardless of whether they be photo-electrons, thermal noise electrons, or electrons generated in charge transfer (Clock-Induced Charge (CIC)). The amplification process is probabilistic and leads in a reduction in the SNR by a factor of up to $\sqrt{2}$ depending on the number of stages in the amplification process and the gain [371]. For typical values for an EMCCD this reduction is close to $\sqrt{2}$ [372]. A schematic of the EMCCD camera readout is displayed in figure 2.8.

The data presented in this thesis was obtained under a low-light level regime in which $\ll 1$ photons per pixel per frame were incident on the detector. Under such illumination conditions a simple threshold is applied in which each frame is binarised by way of setting pixels with analogue counts greater than or equal to a given value as a 1 and those with analogue counts of less than this value set as 0. This is suitable because multiple photon events per pixel per frame is not a high probability event and so more complex photon-counting strategies are not required.

As can be seen in figure 2.9 the histogram of analogue counts for all pixels in $50,000$ frames comprises a Gaussian component which represents readout noise, and a linear component or tail that represents the clock induced charge. These components are present in both the dark frames (black line) and the bright frames (red line) as represented in figure 2.9. In the case of the

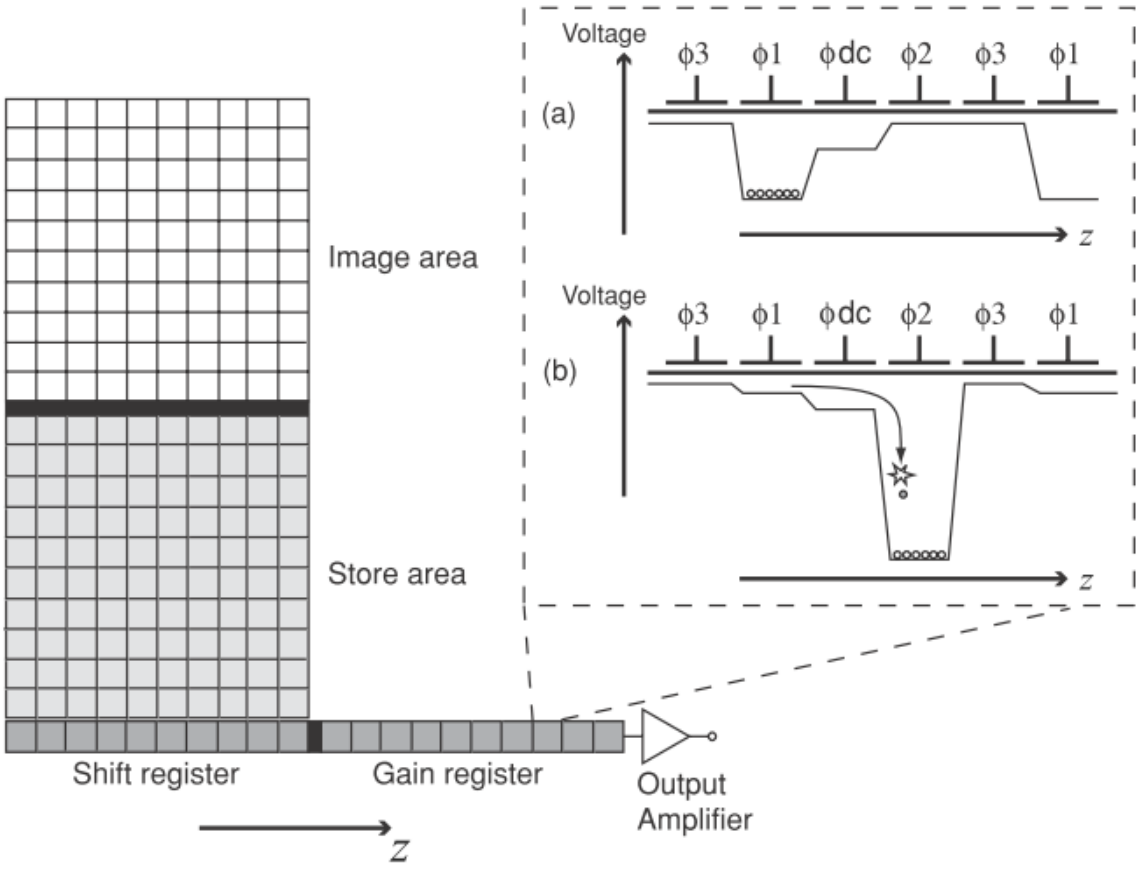

Figure 2.8: **Schematic of readout including additional EM gain register for EMCCD cameras.** Schematic of the physical CCD array (left) in which the electrons are transferred from the image area to the storage area prior to readout via the shift register. The EM gain register is before the readout amplifier such that the signal from electrons may be amplified without amplifying any output amplifier noise. Image of EM gain process (right) in which large voltage is applied at $\phi 2$ to accelerate the electrons and encourage electron multiplication by avalanche effects. Image from Zhang et al. (2009) [373].

bright frames, that is the sensor is under illumination, the linear component is slightly increased and it is here that photon events are represented. It is not possible to definitively separate the photon events from the signal events due to the significant overlap in analogue counts for pixels whether a photon is incident on the detector or not. In an attempt to separate the events that may correspond to real photon-pairs such that they may then be utilised to perform quantum enhanced imaging a threshold is applied. Pixels with an analogue count of value greater than this threshold are regarded as having registered an event, while those pixels with analogue counts less than this threshold are regarded as registering no event. Due to the overlap in the analogue counts for the cases of dark noise and under illumination there is a trade-off between the quantum efficiency

(that is the efficiency with which photons are detected and the pixel being regarded as having registered an event) and level of detector dark noise that is accepted by the thresholding process. In applying a threshold the acquired frames are binarised and the analogue threshold (T) was set to be greater than the mean of the analogue counts plus n standard deviations as per equation 2.4. The exact methods of thresholding for each set of data will be explained in the appropriate chapter. The threshold set on the data presented in figure 2.9 is $n = 3.5$ in which the statistics are calculated on a global basis.

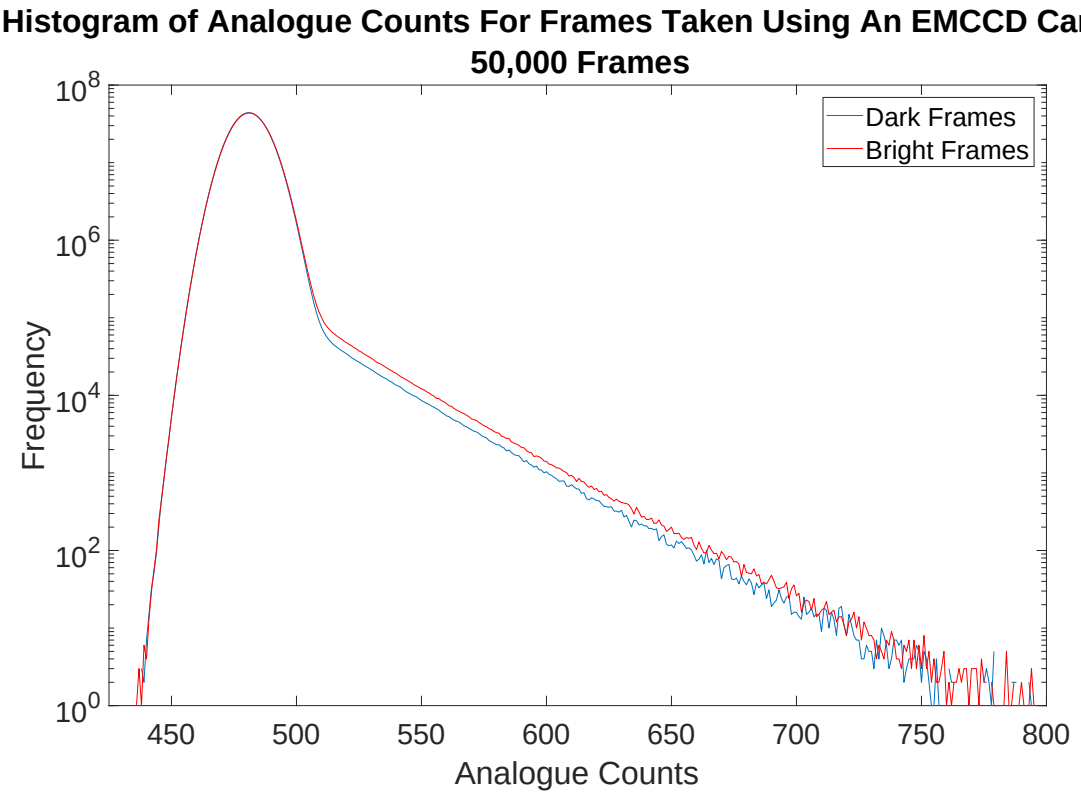

Figure 2.9: **Histograms of analogue counts for frames obtained using an EMCCD camera.** Histogram of analogue counts for dark frames taken with the camera shutter closed (blue line), and frames in which the camera shutter was open and the sensor is under SPDC illumination (red line). Histograms built from 50,000 frames. Bright frames obtained under illumination level in which SPDC photon events are equal to camera noise events for a threshold of $T = \mu + 3.5\sigma = 510$ analogue counts.

$$T \geq \mu + n\sigma \tag{2.4}$$

As mentioned previously, EMCCD cameras were used to measure spatial correlations and observe EPR paradox [179, 180, 334–336, 340, 373–375], to observe sub-shot-noise behaviour

[149, 348, 367, 376], and to perform quantum imaging [279, 293, 377].

2.4.2 ICCD Camera

An Intensified CCD camera (ICCD) is a CCD camera with an image intensifier located in front of the sensor. The image intensifier comprises a photocathode to convert incident photons into electrons, which are then accelerated and multiplied by impact ionisation under a high-voltage (500 V $-$ 1 kV) applied across a microchannel plate into a phosphor screen to reconvert the electrons into photons which are then detected by the CCD sensor [378, 379]. An ICCD camera acts to amplify the signal in a low-noise manner as only external photons incident on the intensifier undergo amplification. Also the intensifier may be time gated to fire on the order of nanoseconds thereby resulting in a short effective exposure time when compared to the CCD exposure time (which for our detector and camera settings was limited to the order of $\sim$ 10 ms) to limit incoming light from spurious sources [373, 380]. That the intensifier may be gated on such short time windows has allowed time of flight measurements with resolution of 10 ps to be performed using an ICCD camera [381]. A schematic of the intensifier is displayed in figure 2.10.

Due to the manner in which the photo-electrons are produced it is a more simple process to separate events that are noise internal to the camera and events that are due to external photons that have struck the intensifier. This is due to the analogue counts in a pixel that corresponds to a photo-electron being much larger than those that correspond to a pixel that only comprises camera noise. As may be seen in the tail in histogram of figure 2.11 the tail extends out to much larger analogue counts in the case of bright frames when compared to dark frames which is unlike the case of the EMCCD histogram. This is due to the signal enhancement scheme in the case of the ICCD camera occurring prior to the pixel readout which means that the thermal electrons in the pixel wells are not also amplified as is the case of the EMCCD camera. Also in the camera frames in the case of a photon striking the intensifier the sensor detects a large number of photons emitted by the phosphor screen which results in 'blooming'. Here a group of pixels detect the photons emitted by the phosphor screen because there is not a perfect coupling between a single microchannel and a corresponding independent pixel. This may be seen

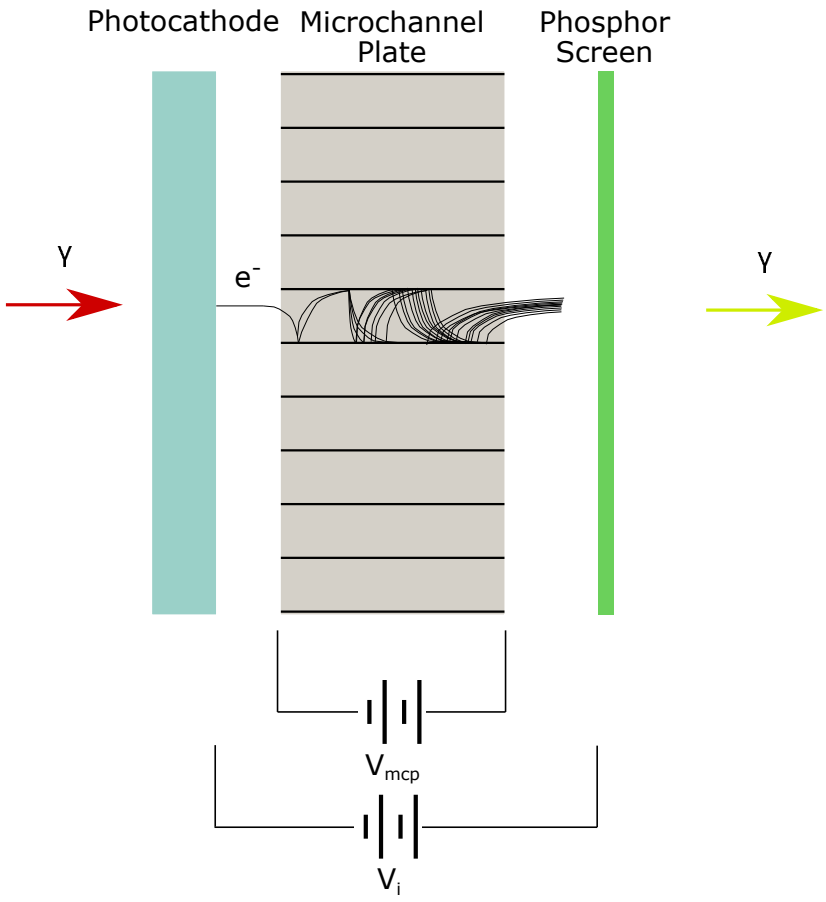

Figure 2.10: **Schematic of intensifier for ICCD cameras.** Photons strike the photocathode and are converted into electrons, a voltage applied across the intensifier V_i serves to accelerate these electrons towards a microchannel plate. A large voltage V_{MCP} is applied across the microchannel plate to accelerate the electrons further such that impact ionisation occurs and the number of electrons are multiplied. These electrons strike a phosphor screen and are converted back into photons which are then detected by a CCD sensor.

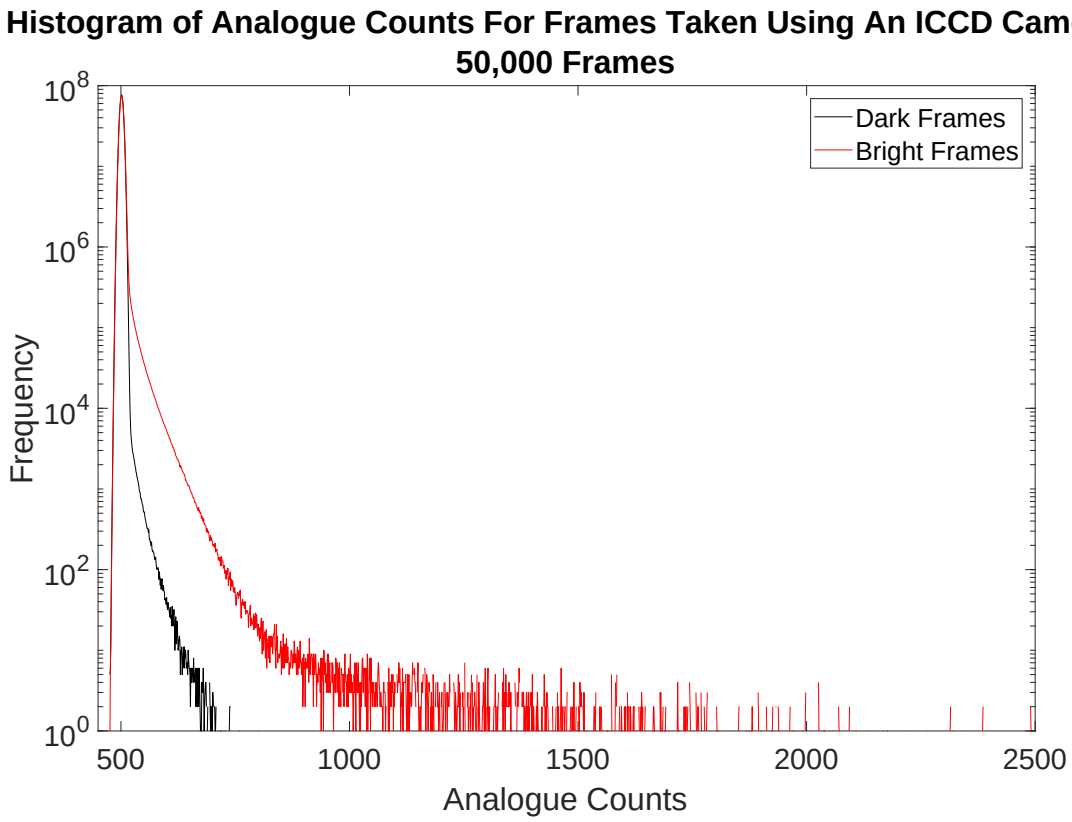

Figure 2.11: **Histograms of analogue counts for frames obtained using an ICCD camera.** Histogram of analogue counts for dark frames taken with the intensifier turned off (black line), and frames in which the camera intensifier was triggered and the sensor is under SPDC illumination (red line). Histograms built from 50,000 frames. Bright frames obtained under illumination level in which SPDC photon events are equal to camera noise events for a threshold of $T = 530$ analogue counts.

as equivalent to cross-talk effects but may be removed by applying a threshold to the images to separate these groups of pixels and then for each group or 'bloom' region determining the pixel with the largest value to be the 'true' position of the photon incident on the intensifier as displayed in figure 2.12.

As mentioned previously, ICCD cameras were used to initially observe and measure spatial correlations [176, 382, 383], and to perform quantum imaging [196–198, 351, 384–386].

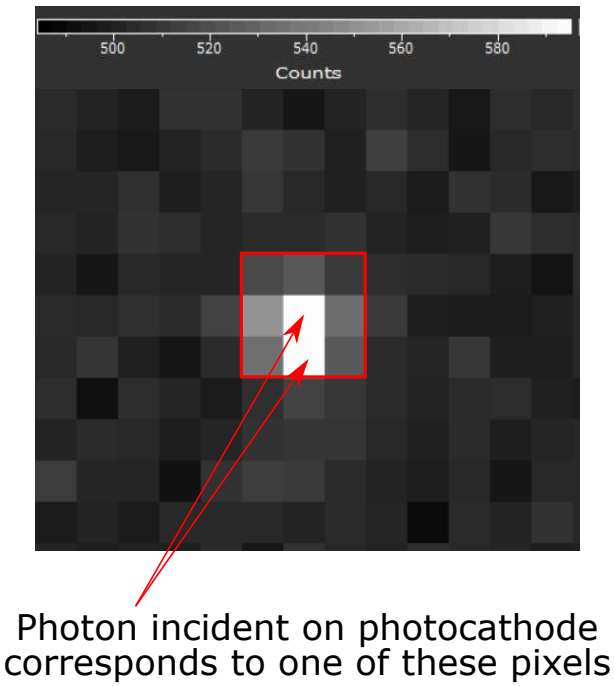

Figure 2.12: **Image of the blooming effect for ICCD cameras.** For ICCD cameras a single photon striking the photocathode results in a blooming effect on the CCD sensor as multiple photons are detected after the intensification process. Multiple pixels detect the intensified photon signal as seen here where the central 9×9 pixels surrounded by the red box appear to have an increased analogue count over the surrounding pixels. For each bloom the pixel with the largest analogue count will be determined to be the 'true' location of the photon incident upon the photocathode

2.4.3 Camera Selection

In order to ascertain the optimal camera technology to use in the experiments presented here in this thesis the EMCCD and ICCD camera technologies were compared. The EMCCD camera used in this work is an Andor iXon Ultra 888 with a 100% fill factor sensor comprising 1024×1024 pixels of dimension $13 \times 13\ \mu\text{m}^2$ [370]. To limit the thermal electrons generated in the CCD pixel wells the camera was cooled to $-90°C$ using a peltier cooling assembly. To reach this sensor temperature water cooling was employed with attention paid to the room temperature and humidity so as to avoid reaching the dew-point and causing condensation to form on the sensor. The stated quantum efficiency of the camera for the incident light with a wavelength of 710nm is stated to be around 77.75% at $-100°C$. The effective efficiency is reduced as the number of standard deviations n at which the threshold is performed on the analogue data is increased. The EMCCD camera settings that were found to be optimal in balancing the readout noise of the camera and the speed of acquisition [348, 387, 388] are as follows: vertical speed: 1.13 μs, vertical amplitude: normal, horizontal shift speed: 10 MHz, EMCCD gain: 1000, preamp gain: 1, exposure time: 0.014951 s. The exposure time used is the shortest exposure time for the given parameters and an acquisition region of 128×128 pixels. Due to the requirements of temperature stabilisation the camera cannot be run continuously due to continuous readout increasing the temperature of the sensor. As a result the camera is effectively throttled and blocks of 500 frames are acquired prior to performing a check on the sensor temperature and whether it remains stable. This serves to effectively double the time required to perform an acquisition when compared to a simple calculation of exposure time $\times$ number of frames.

The ICCD camera used in this work is an Andor iStar [379] with a sensor comprising 1024×1024 pixels of dimension $13 \times 13\ \mu\text{m}^2$. The camera was cooled to $-25°$C by air cooling to reduce the thermal electrons in the CCD pixel wells. The stated efficiency of the intensifier (Andor photocathode model 18U-A3) at room temperature for the incident light with a wavelength of 710 nm is around $\sim 30\%$. The total detector efficiency (photocathode plus CCD) for single photon detection will be lower. Work to determine the quantum efficiency of an ICCD with a photocathode of the same generation (Gen-3) was found to be around a third of the stated value of 28% for light at 780 nm after taking into account a reasonable threshold to apply to

the data [389]. The ICCD camera settings that were found to be optimal are as follows: vertical speed: 6.5 μs, vertical amplitude: normal, horizontal shift speed: 3 MHz, preamp gain: 1, exposure time: 0.025s which is the shortest exposure time for the given parameters and the given acquisition region of 128×128 pixels, and triggered using a signal generator running at 500 kHz.

Using the above settings for each of the ICCD and EMCCD array detectors an image of the quantum illuminated bird in a thermally illuminated net was acquired. The SPDC illumination ratio to thermal illumination ratio of the bird to the cage was ~ 0.8 in the case of the ICCD and ~ 0.9 for the EMCCD. In both cases the event rate for the SPDC illumination was set to equal the noise event rate of the array detector. Each of the images was assessed according to the metrics defined in Chapter 4 in which the improvement of the quantum enhanced image relative to the corresponding classical image is assessed. Further discussion on these metrics will be reserved for the appropriate chapter. The improvement in these metrics is greater when using the EMCCD than with the ICCD camera with regards to both noise rejection and distinguishability by $\sim 30\%$ and $\sim 69\%$ respectively. While the relative enhancement is greater for the image set captured using the EMCCD camera than for the image set captured with the ICCD camera, the quantum enhanced image constructed from frames captured by the ICCD camera exhibits greater contrast. That the ICCD is capable of improved imaging performance when compared to the EMCCD might indicate that using the ICCD detector technology would be the appropriate of choice of detector for the purposes of quantum imaging. However, the ICCD camera required 10 days to acquire 9.9 million frames to construct a final image containing 4586 events in total. This compares to the EMCCD camera which required 36 hours to acquire 2.4 million frames to construct a final image containing 58353 events in total. Therefore, it is much more time-efficient to use the EMCCD camera to perform imaging and to conduct testing of new ideas in addition to it taking much less time to optimise the system. It may also be seen by qualitatively assessing the resulting quantum enhanced images in figure 2.13 that the image obtained using the EMCCD camera exhibits greater contrast between the regions that are represented by the bird and the regions that are represented by the cage, and also displays greater image smoothness. As a result all subsequent data presented in this thesis is obtained using an EMCCD camera to

perform quantum enhanced imaging.

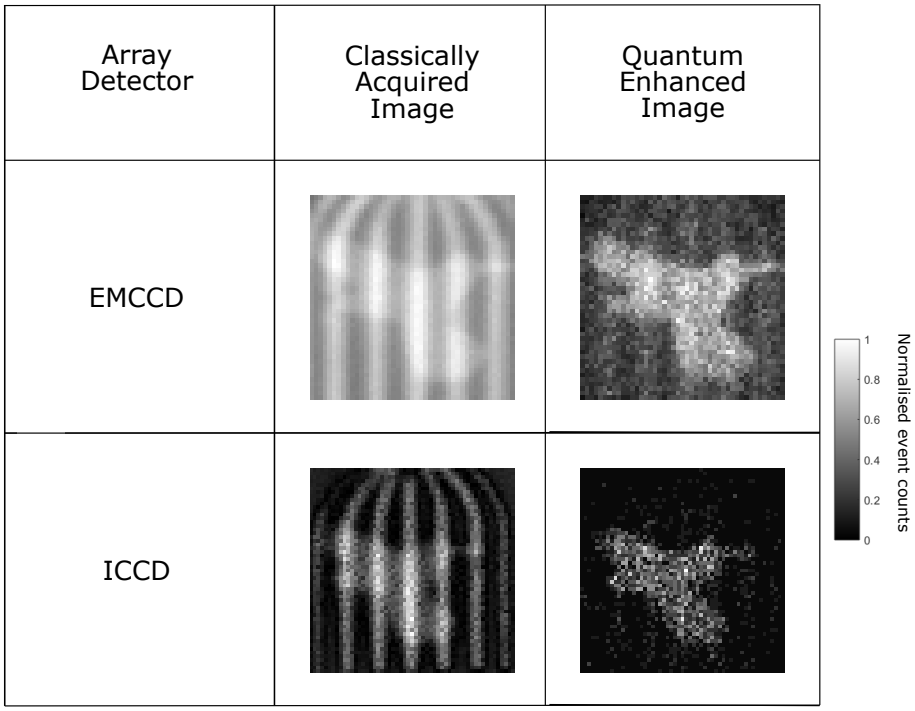

Figure 2.13: **Quantum enhanced images obtained using an EMCCD and an ICCD for the purposes of comparison.** For each of the array detectors the classically acquired image (left) is presented next to the quantum enhanced image (right) for comparison.

Chapter 3

Contrast Enhanced Imaging

3.1 Introduction

The work presented in this chapter utilises the spatial correlations between SPDC photon-pairs to improve image contrast. This is demonstrated through imaging a binary object under low-photon flux conditions. Under the conditions of low-photon flux the environmental noise and detector readout noise degrade the image contrast. However, by exploiting the spatial correlations between entangled photon-pairs generated by SPDC, uncorrelated detector noise events can be preferentially rejected and SPDC photon-pair events preferentially selected. By performing a bitwise AND-operation to select spatially correlated detector events, the SPDC photon-pair events are preferentially selected. The result of performing this AND-operation on a frame-by-frame basis is used to construct the correlated light AND-image, while the raw sum of the frames form the classically acquired image. This quantum imaging protocol was applied to perform imaging of a binary object using a commercially available EMCCD camera under a low-photon flux regime. The resulting image contrast and the improvement of the quantum imaging protocol over classical direct imaging under an identical illumination regime was assessed the contrast was enhanced by a factor of 4.56 ± 0.07 for the quantum enhanced AND-image relative to the classical average image. This imaging scheme was then used to image a series of binary objects for which the quantum enhanced AND-image is qualitatively superior. Previous work has been conducted on the subject of using the spatial correlations between SPDC photon-pairs to

perform contrast enhanced imaging. That work also used an EMCCD camera as the detector, however, the photon source was a downconversion crystal cut for type-I phase matching and the object was located in the image plane of the downconversion crystal and so a different pair detection algorithm was employed [390].

3.2 Experimental Methods

3.2.1 Experimental Setup

The experimental setup may be seen in figure 3.1 with the pump beam prepared prior to the downconversion crystal as described in section 2.2. In the far-field plane of a downconversion crystal cut for type-II phase matching, the SPDC beams are spatially separated thereby allowing an object to be placed in the path of only one of the beams (the probe beam) while the reference beam has a free optical path. Apart from the placement of the object in the path of the probe beam the two beams undergo transmission through an otherwise identical optical path. This far-field plane, in which the object is located, is demagnified by a factor of eight and then re-imaged onto an EMCCD camera such that the two beams are detected on different portions of the sensor. The far-field plane was demagnified so as to reduce the size of the correlation peak with respect to the size of the pixels on the detector. Demagnification of the far-field plane will serve to increase the number of SPDC photon-pairs arriving in anti-correlated pixel positions on the detector through demagnifying the width of the correlations. There is a limit to the level of demagnification that can be chosen while still maintaining the ability to build an image which is not radically under sampled. The optimal illumination regime to maximise resulting image contrast was found through simulation and verified by experiment. This was found to be a regime in which the detector noise event rate per pixel per frame after thresholding is equal to the SPDC photon event rate per pixel per frame after thresholding. The thresholded events per pixel per frame from the detection of SPDC photon events matches the event rate due to the noise of the camera. The analogue threshold applied to each frame was set to $T \approx \mu + 3.5\sigma$ where μ and σ are the mean and standard deviation of the detector readout signal for a set of dark frames. The approximation is due to digitised camera output. For the detector and acquisition settings

used here dark event rate at this threshold is ~ 0.0016 events per pixel per frame and so the SPDC illumination was set to achieve a total event rate of ~ 0.0032 events per pixel per frame. This level of SPDC illumination corresponds to $\sim 10^{-17}$ J/frame incident upon the sample after efficiency considerations are taken into account (see section 3.3.1).

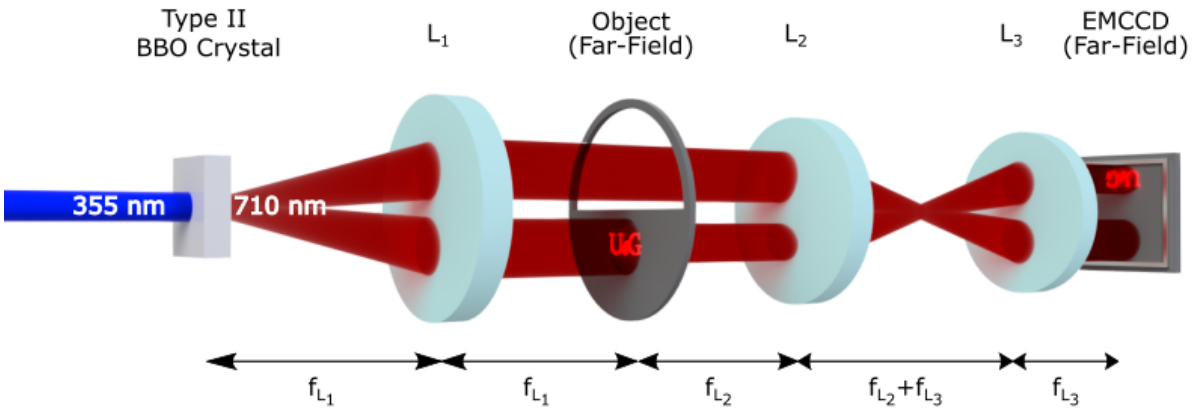

Figure 3.1: **Schematic of the contrast enhanced imaging experimental setup.** The target object is located in a far-field plane of the downconversion crystal in which the probe beam interacts with the target object while the reference beam has a free optical path. The lenses $L_1 = 75$ mm, $L_2 = 400$ mm, and $L_3 = 50$ mm comprise the optical system. used to demagnify the object plane by a factor of eight onto the EMCCD camera which is also located in a far-field plane of the downconversion crystal.

For the work presented in this chapter, great efforts were made to shield the experiment and the detector from background stray light because this uncorrelated source of light serves to effectively increase noise level through the addition of uncorrelated noise events. The aim of the work presented in this chapter was to maximise image contrast when performing imaging at a low-level of SPDC photon flux given a fixed background noise, and to apply this illumination regime to the imaging of binary test targets and realistic physical objects.

3.2.2 Data Analysis

The SPDC beams are detected in the far-field of the downconversion crystal in which the probe and reference beams are spatially separated. The acquired frames are binarised by means of

thresholding as described previously. Frames containing events of an extraordinary nature such as cosmic rays are identified by their containing pixels with large ADC output and then removed. To construct an AND-image, the two regions of the camera sensor on which the probe and reference beams are detected (ROI1 and ROI2) are extracted and ROI2 is rotated through an angle of π (equivalently the rows and columns of the region are reversed) to transform the detected anticorrelation into a position correlation. A bitwise AND-operation is performed on the two regions to select the detected momentum anticorrelated photon-pair events as shown in figure 3.2. The results of this AND-operation are summed over a number of frames to build the correlated light AND-image. In the case of the uncorrelated light AND-image, the above described operation is performed on ROIs from subsequent frames and therefore only random correlations are selected by performing the AND-operation. The spatial correlations, and also the advantages thereof, will only be evident in the case of the correlated light AND-image and not in the uncorrelated light AND-image. The classically acquired image is built by summing all events over all frames. By comparing the absolute contrasts of the correlated light AND-image and the classically acquired image the contrast improvement may be assessed.

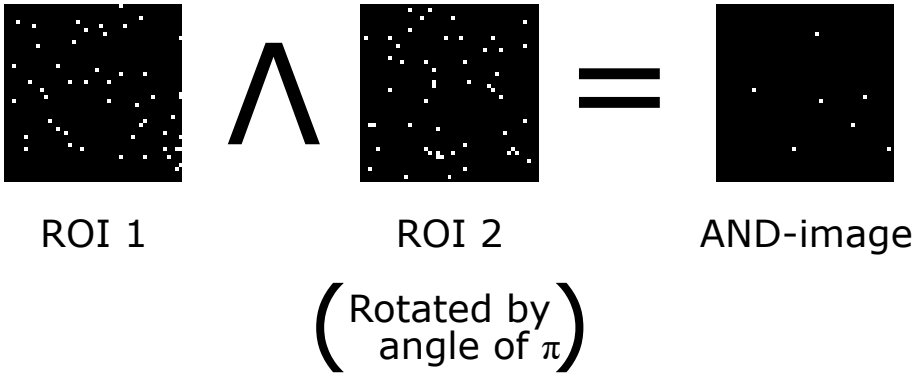

Figure 3.2: **Demonstration of the AND-operation.** Demonstration of the AND-operation in which ROI1 and ROI2, which comprise the probe and reference beams, are extracted from each camera frame. ROI2 is rotated through an angle of π and then the AND-operation is performed to preferentially select the spatially correlated photon-pair events.

3.3 Theory

In performing the AND-operation on the reference and the probe beam, the spatially-correlated photon-pairs will be preferentially selected and the uncorrelated environmental and camera noise

preferentially rejected. In the case of uncorrelated events the AND-event rate per pixel per frame is proportional to the number of events per pixel per frame in the two regions of interest that comprise the probe and reference beams, as defined by R_{Uncorr}, however, under quantum illumination there is an additional term due to the spatial correlations giving an increased AND-event rate, R_{corr}. The rate of AND events per pixel per frame are represented in equation 3.1. In this equation d represents the noise event rate per pixel per frame, p the photon event rate per pixel per frame, and η the efficiency with which the photon-pairs are detected by the camera in anticorrelated positions.

$$\begin{aligned} R_{Uncorr} &= (p+d)^2 \\ R_{Corr} &= p\eta + (p(1-\eta)+d)^2 \end{aligned} \tag{3.1}$$

The ratio, R, may be introduced as a measure of the proportion of AND-events that correspond to AND-events between entangled photon-pairs. This ratio may be used to determine the optimal SPDC illumination regime (SPDC event rate p) in which the maximum proportion of total AND-events correspond to AND-events resulting from spatial correlations between photon-pairs and not accidental AND-events which contribute noise to the final correlated light AND-image.

$$R = \frac{R_{Corr} - R_{Uncorr}}{R_{Corr}} \tag{3.2}$$

The optimum SPDC event rate was determined by measuring the ratio R across a range of light-levels. This was assessed by rotating a half-wave plate placed in the pump beam before the downconversion crystal through a range of angles corresponding to different light-levels and measuring the ratio R as given in equation 3.2. As may be seen in figure 3.3 the number of events per pixel per frame that offers the maximum advantage in the ratio R for the given camera noise background is found to be at a thresholded event rate of ~ 0.003 events per pixel per frame. This event rate corresponds to the regime in which the events per pixel per frame resulting from SPDC photon detection events equals that of noise events and which corresponds to the results of Tasca et al. (2013) [340]. The AND-efficiency of the system η is determined to be 0.005825

or 0.58% by calculating a line of best fit to the data points presented in the graph.

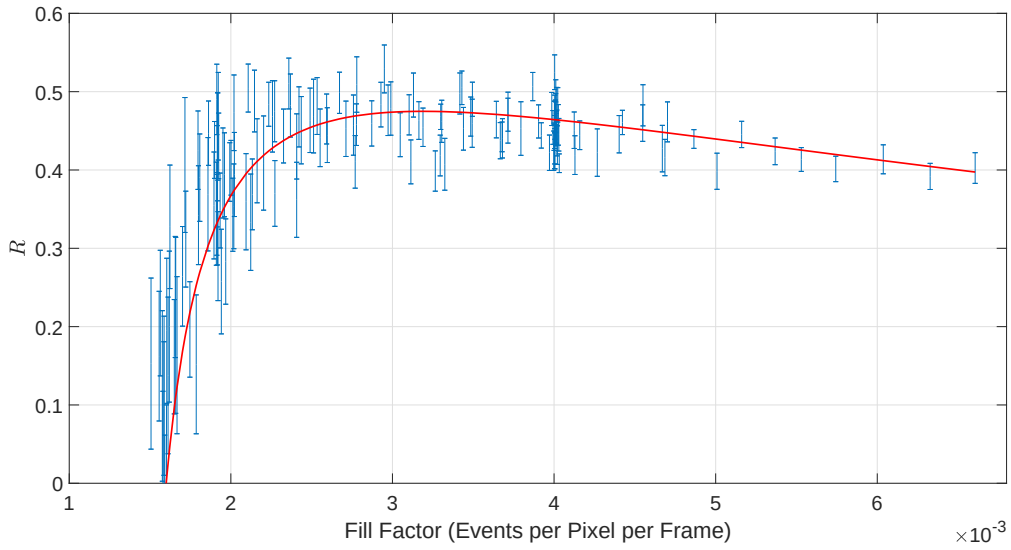

Figure 3.3: **Plot of the ratio of real correlated events vs fill-factor.** Ratio of the rate correlations between real events per pixel per frame kept from correlated light, R, vs the total rate of events per pixel per frame kept for a range of fill factors. Each point represents the mean value of 50,000 frames at a given light level with the error bars representing the standard error on the mean calculated from blocks of 5,000 frames.

This illumination level is then used to build the images by the aforementioned method. The contrast of these images may be quantitatively assessed using the Michelson contrast or visibility (V) as represented in equation (3.3) [391]. The visibility is defined as the difference between the average number of the events per pixel in the bright region of the image (I_{max}) and that in the dark regions of the image (I_{min}) divided by the sum of these two values.

$$V_{Q/C} = \frac{I_{max} - I_{min}}{I_{max} + I_{min}} \tag{3.3}$$

Furthermore, the visibilities $V_{Q/C}$ may be used to assess the contrast advantage ratio A at this light level, which is defined as the ratio between the image contrast of the contrast enhanced AND-image, V_Q, and the image contrast of the classical image obtained by summing all events over all frames, V_C.

$$A = \frac{V_Q}{V_C} \tag{3.4}$$

Using the above equations the contrast advantage ratio A across a range of light levels can

be simulated. As can be seen in figure 3.4 the lower the light level the greater the advantage (for a fixed AND-efficiency rate). The illumination level chosen was therefore the previously determined rate of 0.0016 detected photon events per pixel per frame so as to maximise the contrast advantage ratio A. Equivalently this maximises the proportion of event pairs selected by the bitwise AND-operation that correspond to real SPDC photon-pairs.

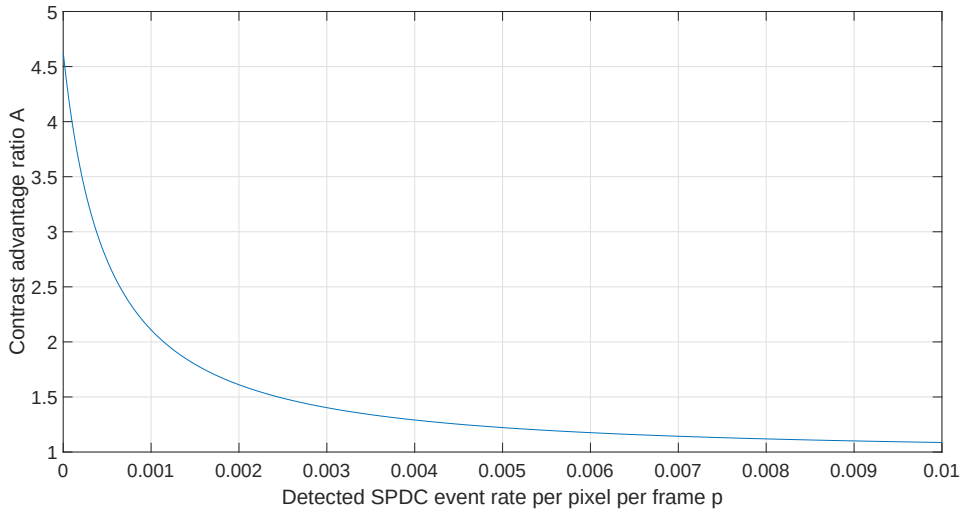

Figure 3.4: **Plot of the ratio of real correlated events vs AND-efficiency.** Ratio of the rate correlations between real events per pixel per frame kept from correlated light, R, vs the AND-efficiency.

For the above determined dark count rate and illumination level a plot of the calculated ratio of correlations that originate from real photon-pair events R vs AND-efficiency η is generated and shown in figure 3.5. In this figure, it is shown that as the AND-efficiency η increases from zero towards one, the ratio of correlations that originate from real photon-pair events increases rapidly. This is because as the AND-efficiency η increases $1-\eta$ decreases and therefore fewer random false correlations can occur.

Another plot of the contrast ratio A vs AND-efficiency η from equation 3.3 is shown in figure 3.6. In this figure it is shown that as the AND-efficiency η increases the ratio of the visibilities is expected to increase towards one due to the same reasons as detailed previously.

From figures 3.5 and 3.6 it is clear that the greater the quantum efficiency, the greater R and A will be.

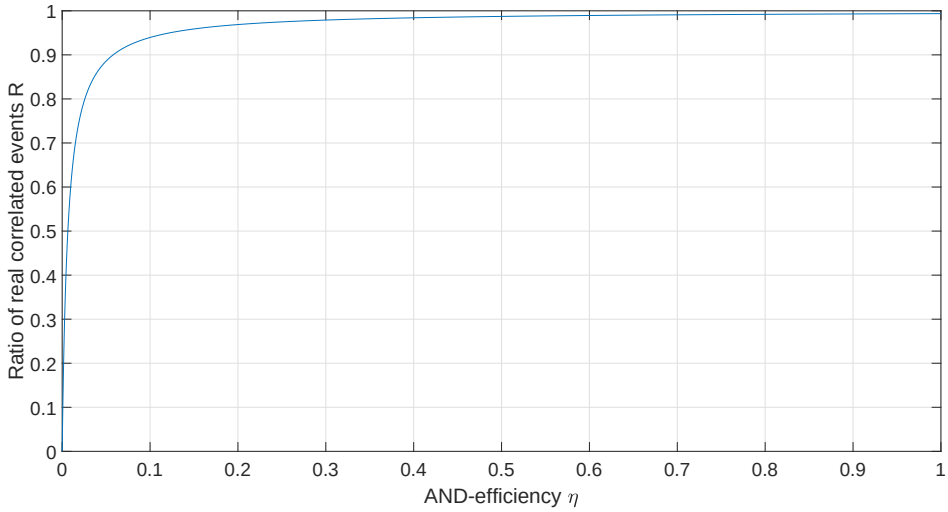

Figure 3.5: **Plot of the ratio of real correlated events vs AND-efficiency.** Ratio of the rate correlations between real events per pixel per frame kept from correlated light, R, vs the AND-efficiency.

3.3.1 Quantum Efficiency

For the experimental setup as described above the quantum efficiency of the system components is estimated below in Table 3.1. The thresholded QE is the estimated total efficiency of the detector efficiency combined with the result of performing the thresholding at $T = \mu + 3.5\sigma$ analogue counts. This was calculated using simulations of the avalanche multiplication effect in EMCCD cameras developed and presented by Lantz et al. (2008) [367]. The effective camera detection and thresholding efficiency is estimated to be $\sim 50\%$. The total efficiency of the detector registering the arrival of a single photon that comprises part of a photon-pair is estimated to be $\sim 41\%$. The estimated efficiency with which both photons that comprise a photon-pair are detected is estimated to be $\sim 17\%$. The correlation peak as measured for the data presented here in this chapter is calculated to be of dimensions $\sigma_x = 1.468$ pixels, $\sigma_y = 1.399$ pixels. Therefore $\sim 10.5\%$ of photon-pair events arrive in exactly anticorrelated positions and as a result are selected by performing the AND-operation. The heralding efficiency, that is the AND-operation efficiency for a real SPDC photon event ν in equation 3.1, is therefore estimated to be $\sim 1.8\%$.

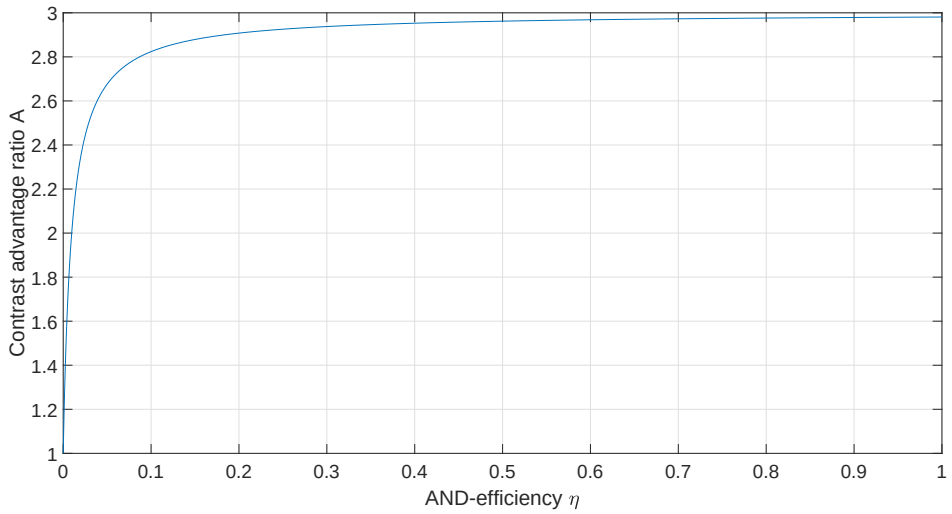

Figure 3.6: **Plot of the contrast advantage ratio vs AND-efficiency.**contrast advantage ratio, A, vs the AND-efficiency.

3.4 Results

The contrast enhancement advantage A at the optimally chosen level of illumination was assessed using a binary target object with regularly spaced bars, akin to a test target, with which the probe beam interacts, while the reference beam has a free optical path. The correlated light AND-image was constructed by performing an AND-operation on the probe and reference beam regions taken from the same frame and summing the result over all frames. The uncorrelated light AND-image was constructed by performing an AND-operation on the probe and reference beam regions taken from frames offset in time and summing the result over all frames. The classical image is the sum across all frames of all of the events detected in the probe beam region. The correlated light AND-image, uncorrelated light AND-image, and classical image are presented from top to bottom in the right of figure 3.7. Each image has been normalised so as to allow a fair qualitative assessment and comparison of the contrast by eye. In these images it may be seen that the contrast is improved for the AND-image constructed using correlated light over that constructed from uncorrelated light and the classical image. Further to the vast improvement when assessed qualitatively, the average value of the each row is plotted for the images constructed using correlated light, uncorrelated light, and the classical image in figure 3.7. From this graph it may be seen that the contrast is improved for the image constructed using

Component	QE
Lens Surface transmission	99.695% at 710 nm for B-Coated lenses (6 surfaces).
Lens Body Absorption	92.140% average over 705-715 nm for 10mm thick N-BK7 assume linear absorption for lens thickness of 3.6, 4.1, 5.3 mm giving 97.103%, 96.777% 95.834% transmission.
Camera Stated QE	Estimated at 77.75% for 710 nm at $-100^{\circ}C$
Thresholded QE (combined camera and threshold)	Estimated at $\sim 50\%$ for 710nm and threshold at $T = \mu + 3.5\sigma$ analogue counts.
Filter Transmission at 710 nm	Dichroic mirrors 98%, Interference filters 99%
Single Photon Detection Efficiency	41%
Photon-Pair Detection Efficiency	17%
Strength of Correlations	10.5%
Quantum Efficiency	1.8%

Table 3.1: **Table of the quantum efficiencies of system components used to calculate total QE of the experimental setup.**

correlated light as the bright and dark regions are separated to a greater degree than in the case of the image constructed by performing the AND-operation on uncorrelated light and the classical average. The images constructed by performing the AND-operation are less smooth than the classical average due to their containing fewer events.

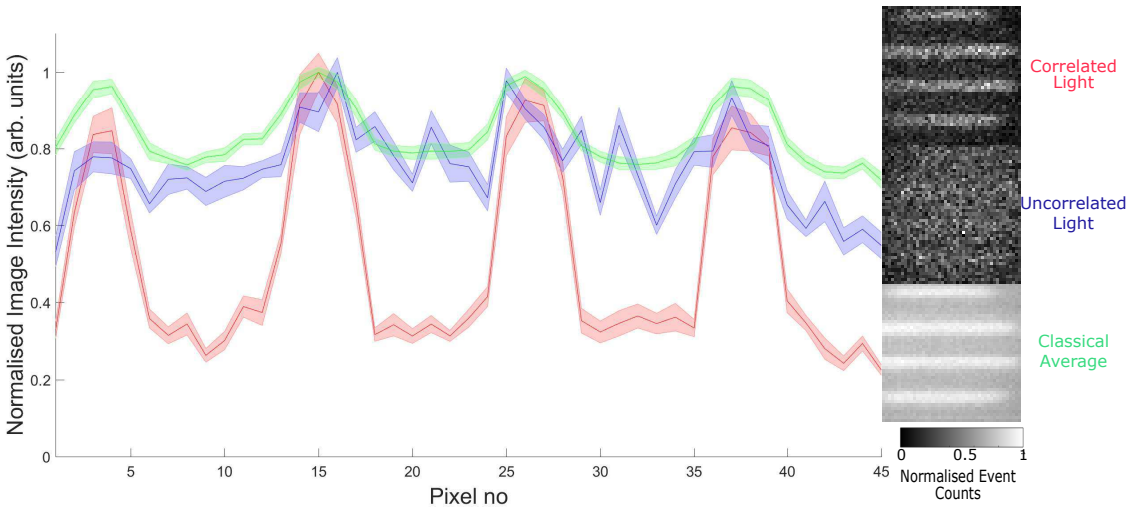

Figure 3.7: **Contrast enhancement demonstrated with a binary test target.** The graph shows the average value of each row for the images presented on the right hand side of the image. The correlated light image is presented in red, the uncorrelated light image in blue, and the classical average in green. The images and graph are calculated over 1,000,000 frames.

The contrast enhanced advantage A for the correlated light AND-image relative to the uncorrelated light AND-image is a factor of 4.84 ± 0.51, and for the correlated light AND-image relative to the classical image is a factor of 4.56 ± 0.07. This indicates a clear contrast enhancement for the correlated light AND-image over the classical image and also shows that the advantage is not an artefact resulting from performing the selection of kept events via the AND-operation as the contrast enhancement is similar in the case of the correlated light AND-image relative to the uncorrelated light AND-image. The contrast-enhanced advantage is greater here because there is some spillage of light from the bright regions into the dark regions by diffraction from the edges of the object. this increases the dark event rate in the dark regions from 0.0016 events per pixel per frame to 0.0022 events per pixel per frame which serves to reduce the contrast of the classical sum image and to a lesser degree also reduces the contrast of the contrast enhanced AND-image. Therefore the effective dark event rate in the dark portions of the image are elevated in both the classical image and the AND-images. For a heralding efficiency of 1.8% (as was previously calculated in section 3.3.1), the expected contrast enhanced advantage for the bars object is of order ~ 4.1 as demonstrated in the experimental result. To demonstrate the improvement in contrast in imaging real-world objects a number of images of binary objects constructed in the same manner for comparison are presented in figure 3.8 in which the contrast enhancement may be easily seen by eye.

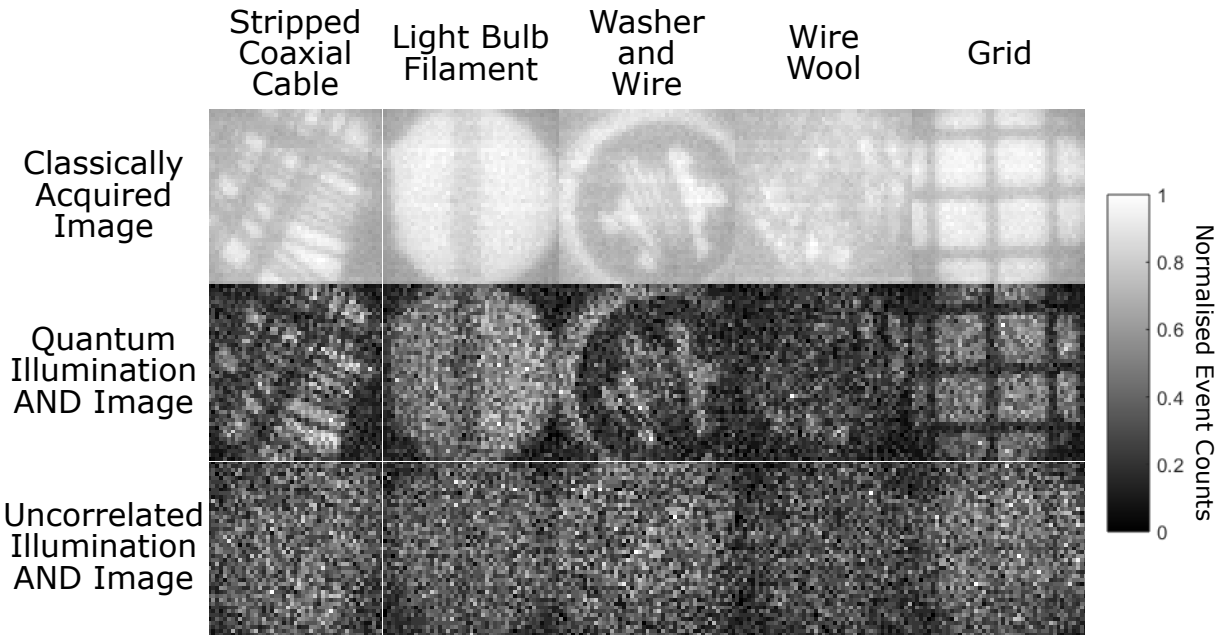

Figure 3.8: **Real-world binary objects imaged to demonstrate contrast enhancement.** For each of the objects three images are constructed using, from left to right, using correlated light, uncorrelated light, and the classical image. The images were constructed from one million frames.

3.5 Discussion

In conclusion the results of this experiment show that by utilising quantum correlations to construct an image using an AND-operation as the selection rule serves to select spatially correlated photon pair events and suppresses the selection of camera noise events in the resulting image. This results in an improvement in terms of image contrast for images constructed by performing the bitwise AND-operation on frames containing correlated photon-pairs when compared to images constructed using frames that do not contain spatially correlated photon-pairs. The improvement in contrast for the AND-image constructed using correlated light relative to that constructed using uncorrelated light was measured to be a factor of 4.84 ± 0.51. The improvement in contrast for the AND-image constructed using correlated light relative to the classical average was measured to be a factor of 4.56 ± 0.07. This result compares to the previous work performed by Izdebski [390] in which a contrast advantage of a factor of 1.44 was achieved operating under similar illumination conditions in which the thresholded number of photon events per pixel per frame was set to be comparable to the thresholded number of noise events for the

EMCCD detector at 0.02 events per pixel per frame. In the work of Izdebski [390] a downconversion crystal cut for type-I downconversion was used as a SPDC source and both the object and the detector were located in an image plane of the downconversion crystal which required a different pair detection algorithm to be utilised. As a result there are further differences with the work that is presented above with regards to selecting event pairs that correspond to spatially correlated photon-pairs but progress with regards to detector noise and the achievable contrast advantage is demonstrated.

An imaging scheme such as that presented here, in which the detection of the photon-pairs is highly parallelised, could conceivably be implemented into microscope configurations in which a low-photon flux is required for imaging purposes, e.g. in the imaging of photosensitive biological tissue samples for which a high-photon flux may cause irreversible damage. The optical damage threshold at visible red wavelengths (640 nm) is of the order $\sim 10^{-4}$ W μm^{-2} [310], while the detected illumination level in this experiment is of the order $\sim 10^{-22}$ W μm^{-2}. This experiment operates well below the optical damage limit for this wavelength, however, the principle presented here could be applied to imaging at different wavelengths for which optical damage thresholds are lower. Such imaging principles could also be applied to the observation of cell processes such as the transition into mitosis from stage G_2 which are light sensitive and halt the division process when under illumination [392]. However, in order to find application in imaging biological samples that are not binary in transmission and which are also liable exhibit movement will require improvements in both the single-frame efficiency with which AND-events are collected to populate the AND-image and also the frame rate of the detector.

Chapter 4

Quantum Illumination as Applied to Full-Field Imaging

4.1 Introduction

The work presented in this chapter utilises spatial correlations between downconverted photon-pairs to demonstrate the first implementation of a quantum illumination full-field imaging protocol [278, 279]. The application of the quantum illumination protocol presented in this chapter is demonstrated through imaging a binary object under low-photon flux conditions with additional background light added. Under the conditions of low-photon flux the environmental noise and detector readout noise degrade the ability to effectively distinguish the real object or scene from the background. However, the effects of these sources of noise on the final image can be mitigated by exploiting the spatial correlations between the entangled photon-pairs generated by SPDC. The twin beams produced via the SPDC process are directed to different regions of an EMCCD array detector and an AND-operation is performed on a frame-by-frame basis to construct the quantum illumination AND-image, while the raw sum of the frames form the classically acquired image. An additional thermal light source is used to introduce background noise onto the region of the camera upon which the probe beam is incident. By performing a simple AND-operation between two regions of an array detector that detect the SPDC beams, correlated photon-pair events are preferentially selected and uncorrelated background and de-

tector noise events preferentially rejected. A rejection of background and stray light of up to 5.8 and an image contrast improvement of up to a factor of 11 is demonstrated. The implementation of this protocol differs from usual quantum schemes in that the advantage is maintained even in the presence of noise and loss.

4.2 Experimental Methods

4.2.1 Experimental Setup

The experimental setup may be seen in figure 4.1 and is a modified version of the setup presented in the previous chapter in section 3.2.1. The optical system for the SPDC light, and the level of SPDC illumination is unchanged from that presented in the previous chapter. The pump beam is prepared prior to the downconversion crystal as described in section 2.2. In the work presented in this chapter the quantum arm of the system remains the same and a classical arm is built to deliberately introduce a background light field using a thermal light source to illuminate a mask which overlays the probe beam through a reflection from a microscope slide slip-cover (MS) placed in the image plane of the crystal. A thermal light source is used so as to simulate real-world conditions in which environmental noise will follow a similar distribution (i.e. noisier than a Poisson distribution) and be broad-band illumination. The probe beam illuminates the object and is subject to environmental losses and noise, while the reference beam neither interacts with the object nor is it subject to environmental losses and noise. The background thermal illumination was added to the region of the sensor on which the probe beam is detected thereby simulating environmental noise at the probe beam wavelength which the quantum illumination protocol is able to reject. Of the previous implementations of quantum illumination protocols in some works [274–276] a thermal light source to introduce background light into the system was used in implementations of a non-imaging schemes. A more recent implementation by England et al. (2019) [277] used a coherent light source to introduce background light into their implementation of a raster scanned imaging scheme. ND filters may be introduced after the target object to introduce optical losses as applied to the probe beam in order to demonstrate the resilience to losses of the quantum illumination protocol.

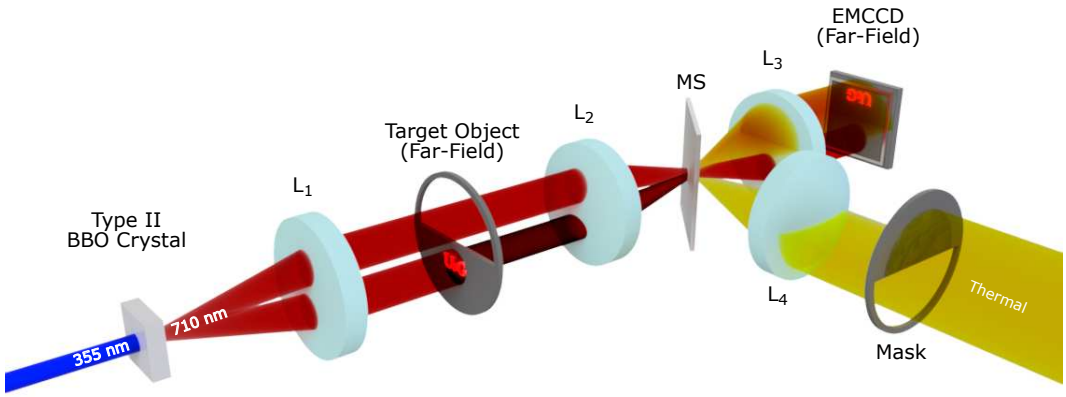

Figure 4.1: **Schematic of the quantum illumination experimental setup.** A BBO crystal cut for type-II downconversion is pumped by a UV laser to produce entangled photon-pairs via SPDC. The probe beam interacts with the Target Object placed in the far-field of the crystal while the reference beam has a free optical path. The lenses $L_1 = 75$ mm, $L_2 = 400$ mm, and $L_3 = 50$ mm comprise the quantum arm optics used to transform into the far-field, and then to demagnify by a factor of eight onto the EMCCD camera. A mask illuminated by thermal light is projected onto the camera using lenses $L_4 = 300$ mm and $L_3 = 50$ mm by reflection from the microscope slide (MS) placed in the image plane of the crystal.

4.2.2 Data Analysis

The data presented in this chapter is analysed in the same manner as described for the work presented in the previous chapter as per section 3.2.2. Performing the bitwise AND-operation on frames containing correlated event pairs, as opposed to recording the simple average image that includes both photon events and also noise events including background illumination, an advantage in image contrast is realised. This advantage is due to the fact that the AND-operation will preferentially select SPDC photon-pair events and will preferentially reject the uncorrelated events that arise from either detector or environmental noise introduced by the thermal source. The number of accidental coincidences between uncorrelated probe and reference events may be reduced by operating in a photon-sparse ($\ll 1$ events per pixel per frame) regime used here as described in section 3.3. In the results presented below the advantage of the quantum illumination protocol is shown to be resilient to thermal noise and to losses introduced into the probe arm.

4.3 Theory

In order to assess the robustness of this QI protocol under differing loss and thermal noise levels the ability of the quantum illumination scheme to reject the camera and thermal noise is measured. The contrast of the quantum illumination AND-image, the uncorrelated illumination AND-image and the classical sum images produced by the methods described in section 3.2.2 may be quantitatively assessed using the Michelson contrast or visibility (V) as represented in equation (4.1) [391]. The Michelson contrast and quantum illumination advantage were described in section 3.3 but are repeated here. The Michelson contrast assesses the difference between the intensities in a bright region (I_{max}) and a dark region (I_{min}) divided by the sum of the events in the bright and dark regions of the image. The quantum illumination advantage, A, is defined as the ratio between of the contrasts V_Q/V_C in which V_Q is the contrast of the quantum illumination AND-image and V_C is the contrast of the image acquired simply by summing all probe-beam events over all frames.

$$\begin{aligned} V_{Q/C} &= \frac{I_{max} - I_{min}}{I_{max} + I_{min}} \\ A &= \frac{V_Q}{V_C} \end{aligned} \tag{4.1}$$

As for the contrast advantage ratio presented in section 3.3, the quantum illumination, A, advantage may be expressed as a function of experimental parameters. The detected event rate of SPDC photons in the reference arm is p_r, the apparatus arm efficiency is η including losses in the quantum illumination arm but excluding losses due to the presence of the target object, the efficiency of the reference arm from the downconversion crystal to the camera is $\eta_r = \eta$ and for the probe arm from the crystal to the camera is $\eta_p = \eta\varepsilon$, where ε is the probe arm efficiency. This gives a detection rate of SPDC photons in the probe arm of $p_p = \varepsilon p_r$. We note d the dark count rates and T the thermal light rate. The AND-event rate for quantum correlated light may then be written as in equation 4.2 in which R^Q_{Bright} represents the rate in regions in which the object is transmissive and R^Q_{Dark} the regions in which the object is not transmissive. The thermal light is only incident on the regions of the detector on which the probe beam is detected and not

on the region of the detector on which the reference beam is detected.

$$\begin{aligned} R^{Q}_{Bright} &= \varepsilon\eta\, p_r + (p_r(1-\varepsilon\eta)+d)(\varepsilon p_r(1-\eta)+d+T) \\ R^{Q}_{Dark} &= (p_r+d)(d+T) \end{aligned} \tag{4.2}$$

The event rate for the classical average in which all events are kept may be written as in equation 4.3.

$$\begin{aligned} R^{C}_{Bright} &= \varepsilon p_r + d + T \\ R^{C}_{Dark} &= d + T \end{aligned} \tag{4.3}$$

The quantum illumination advantage, A, is derived from these equations and may be written as a function of the experimental parameters as in equation 4.4.

$$A = \frac{(R^{Q}_{Bright} - R^{Q}_{Dark})(R^{C}_{Bright} + R^{C}_{Dark})}{(R^{Q}_{Bright} + R^{Q}_{Dark})(R^{C}_{Bright} - R^{C}_{Dark})} \tag{4.4}$$

In this work the quantum advantage reported is relative to the optimum classical imaging case by performing photon-counting so as to allow identical experimental conditions to be used to obtain the quantum and the classical data. Lopaeva et al. (2013) [274] compared the twin PDC beams (quantum) to a single split PDC beam (classical). This experiment was performed in a high-gain regime and therefore it is possible to split a single beam for which there is a continuous stream of photons into two beams but for a low-gain regime this is not possible as you cannot split a single photon into the two arms and detect two photons at the detector. In the low-gain regime there will be very few double pairs to split at the beamsplitter and subsequently find any classical correlations between the beams. As a result the comparison image would require an obscene integration time or require further alterations to the optical setup which would render any comparison between the quantum illumination AND-image and the classically acquired AND-image invalid in our case. The uncorrelated AND-image which comprises random correlations could be used as a comparison but it is a subsample of the classical sum image and is suboptimal compared to the classical sum image due to its containing fewer events and therefore has an increased shot-noise.

4.4 Results

4.4.1 Quantum Illumination Contrast Enhancement

The robustness of the quantum illumination protocol under differing levels of thermal noise and losses is assessed here. In order to allow the contrast of the resulting images and by extension the quantum illumination advantage to be assessed a binary mask was used as the target object and the thermal background is unstructured. The target object is a binary mask of the University of Glasgow (UoG) initials laser cut from a piece of card. In figure 4.2 a comparison between the quantum illumination AND-image may be seen and the quantum illumination advantage A is assessed over a range of increasing thermal background illumination.

For the images presented in figure 4.2 the quantum illumination advantage, A, increases with the increasing level thermal illumination relative to SPDC. This trend is also shown in the graph presented in figure 4.3. The increase in the quantum illumination advantage, A, as the level thermal illumination relative to SPDC increases is due to the classical image contrast degrading at an increased rate when compared to the quantum illumination AND-image. This is the result of the classical image keeping all events, while in the case of the quantum illumination AND-image only correlated event pairs are kept due to the AND-operation being performed.

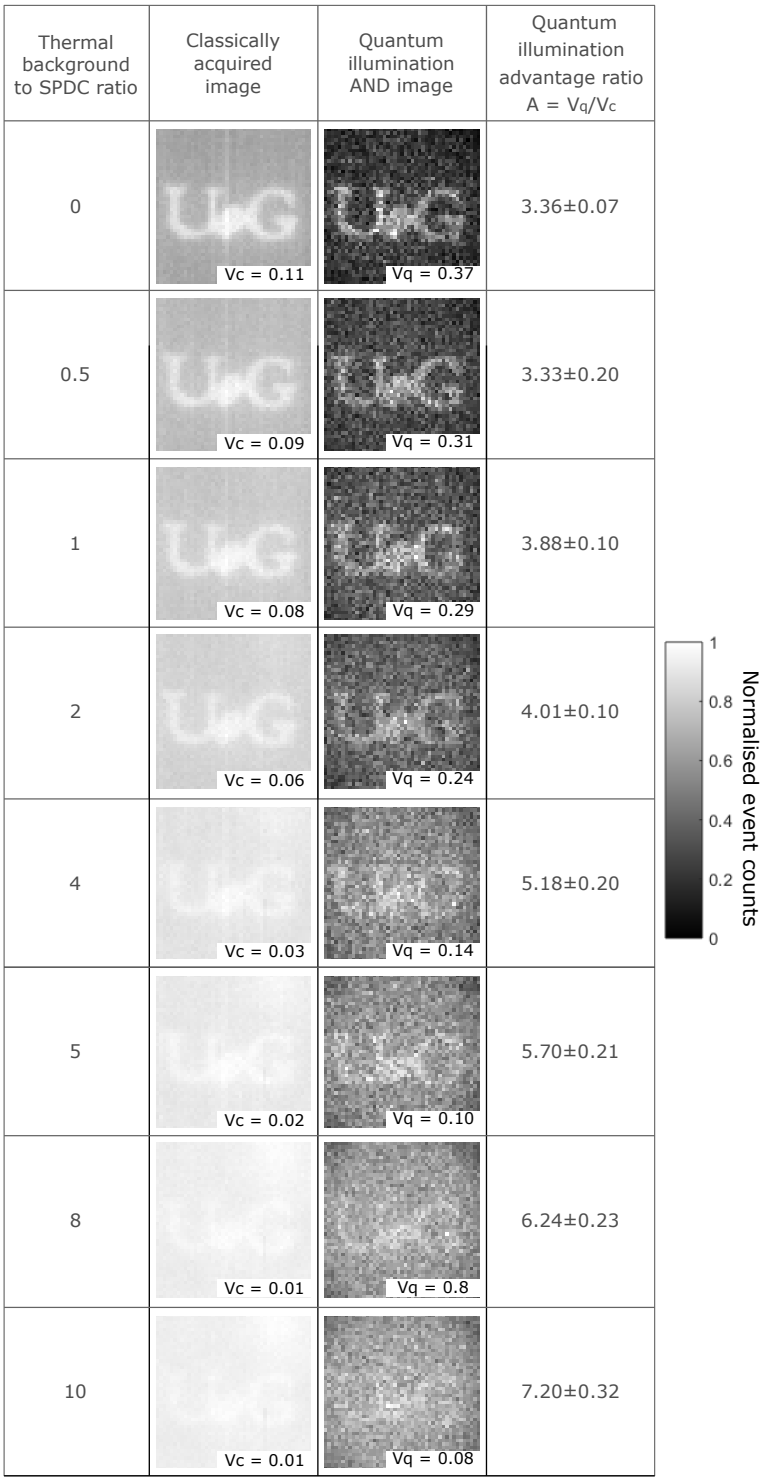

Figure 4.2: **Images of UoG using quantum illumination within a thermal background.** Classically acquired images of the UoG target object which are obtained by averaging all frames (left), and the quantum illumination AND-image which is obtained by summing the result of performing the AND-operation on a frame-by-frame basis in order to select correlated event-pairs in the reference and probe beams (right). The UoG target object is illuminated by the probe beam under a fixed illumination level for all acquisitions. Imaging is performed under an unstructured thermal background, the level of which increases (the ratio of thermal illumination to SPDC at 710 ± 5 nm is presented in column one). The quantum illumination advantage A is calculated for all pairs of images and presented. Images are constructed over 1.5 million frames. The given uncertainty is the standard error on the mean calculated using blocks of 100,000 frames. Images are 45×45 pixels.

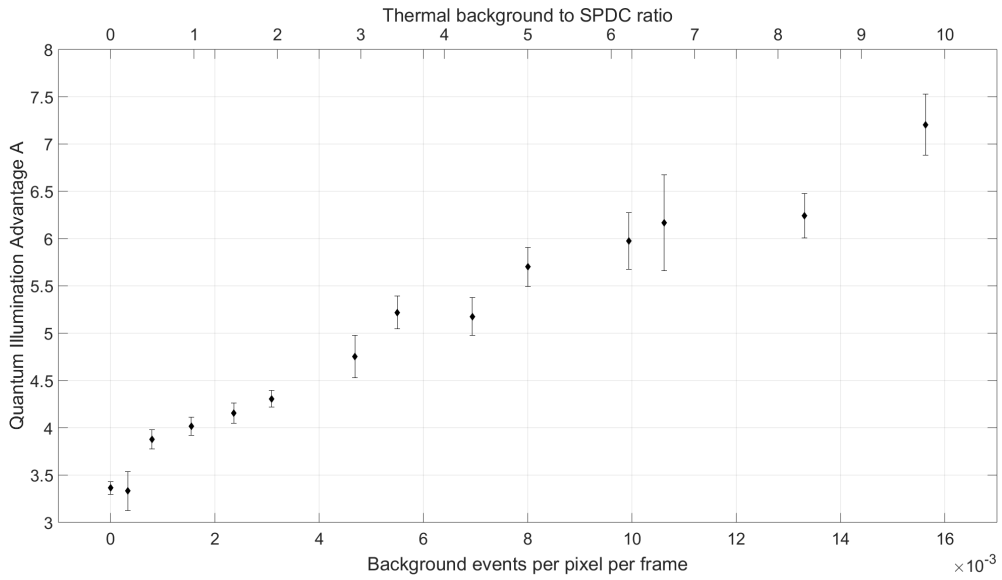

Figure 4.3: **Graph of the quantum illumination advantage under an increasing a thermal background.** Graph of the quantum illumination advantage, A, given for the range of levels of thermal illumination for images constructed over 1.5 million frames. The given uncertainty is the standard error on the mean calculated using blocks of 100,000 frames.

For the images presented in figure 4.4 quantum illumination advantage, A, may also be seen to increase as the level of optical losses introduced into the probe beam increases. The losses are introduced into the probe beam by means of placing an ND filter in the beam path. This trend is also is shown in the graph presented in figure 4.5.

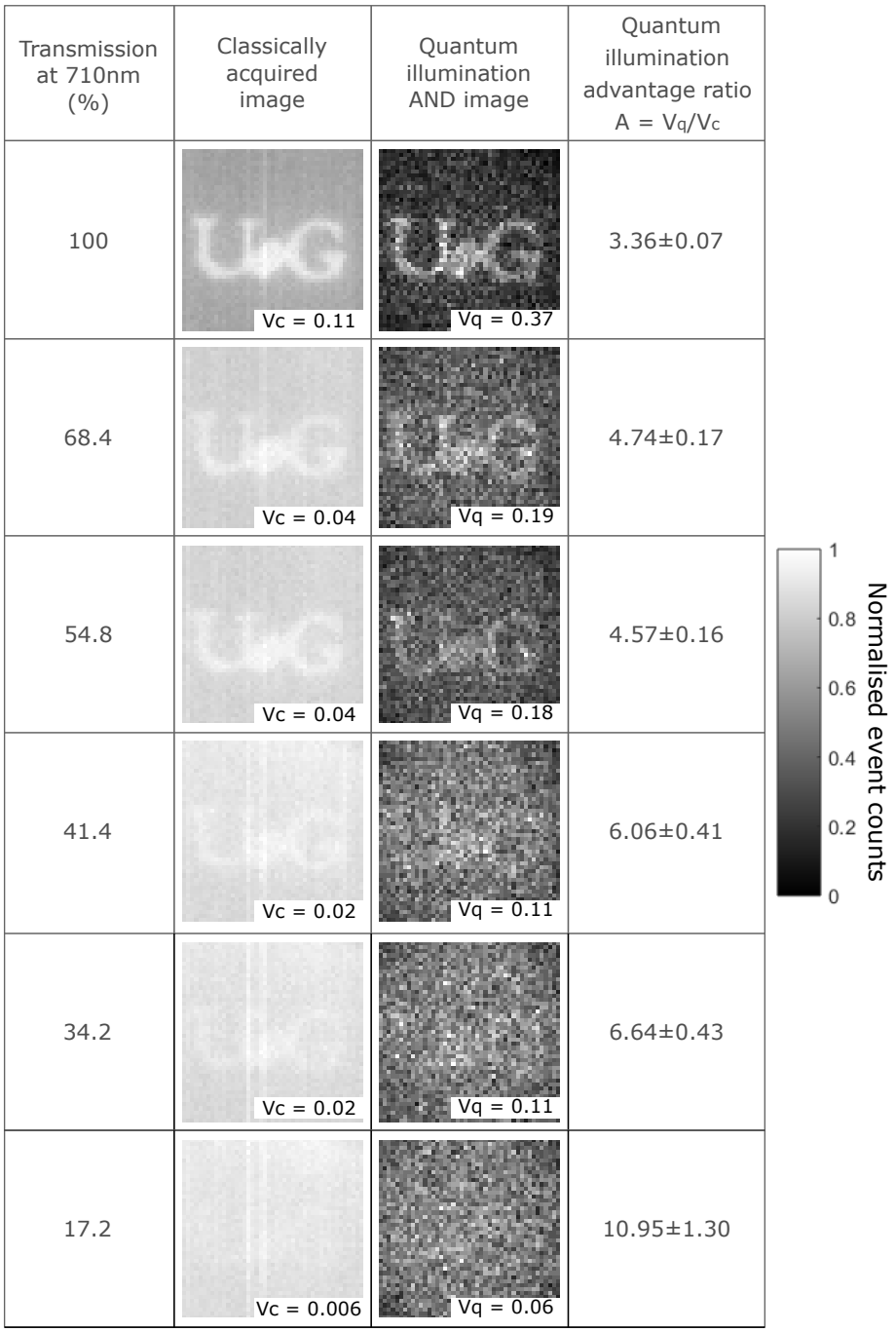

Figure 4.4: **Imaging using quantum illumination with losses introduced.** Classically acquired images of the UoG target object which are obtained by averaging all frames (left), and the quantum illumination AND-image which is obtained by summing the result of performing the AND-operation on a frame-by-frame basis in order to select correlated event-pairs in the reference and probe beams (right). The UoG target object is illuminated by the probe beam under a fixed illumination level for all acquisitions. Imaging is performed under an unstructured thermal background, the level of which remains constant (the ratio of thermal illumination to SPDC at 710 ± 5 nm is $\sim 1:1$). The quantum illumination advantage A is calculated for all pairs of images and presented. Images are constructed over 1.5 million frames. The given uncertainty is the standard error on the mean calculated using blocks of 100,000 frames. Images are 45×45 pixels.

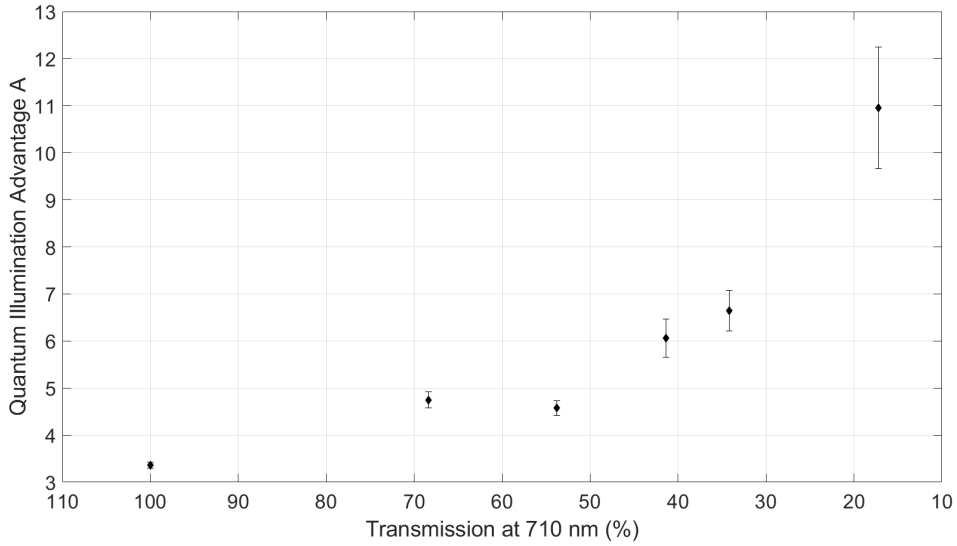

Figure 4.5: **Graph of the quantum illumination advantage under increasing losses.** Graph of the quantum illumination advantage A for the system under differing levels of optical loss. The quantum illumination advantage A is assessed under these levels of optical losses for images constructed over 1.5 million frames. The given uncertainty is the standard error on the mean calculated using blocks of 100,000 frames.

4.4.2 Bit Error Rate Enhancement

Further to the imaging results presented above for this quantum illumination protocol the ability of this protocol to discern the presence or absence of an object needs to be assessed as per the work of Lopaeva et al. (2013) [274]. This work is the context in which the quantum illumination protocol was originally propose by Lloyd [265] as it is in this context in which the protocol may be applied in realising quantum lidar and quantum radar. A strategy that combines the information from both the classical data and the quantum data can be shown to always lead to a bit-error-rate enhancement, so long as there exists a contrast advantage in the quantum data.

The theoretical works regarding quantum illumination [265, 266] assume that the experimental apparatus are lossless and therefore that the efficiency of both the signal and idler arms is unity. This assumption certainly does not hold for the setup described here and therefore the strategy to determine the presence or absence of a target on a pixel-by-pixel basis must be determined. The first strategy assumes that no information is known regarding the noise or the target object and for which the use of the AND-image will display a bit error rate enhancement. The second strategy assumes knowledge of the noise of the system and uses a combination of

the AND-image and the classical image to show an enhancement. Using both methods a bit error rate enhancement is displayed thereby indicating that a contrast advantage quantified as the quantum illumination advantage in 4.4.1 implies a bit error rate enhancement.

Blind Strategy

The blind method used to determine the bit error rate in estimating the presence or absence of a target, through both a quantum illumination and a classical illumination protocol. The bit error rate P_{err} is determined as the rate of erroneously predicting the presence of the target when it is absent $P_{Bright}(0)$ and rate of erroneously predicting the absence of the target when it is present $P_{Dark}(1)$.

The bit error rate may be written under the hypothesis of equal probability of the presence or absence of the target as in equation 4.5.

$$P_{err} = \frac{1}{2}P_{Dark}(1) + \frac{1}{2}P_{Bright}(0) \tag{4.5}$$

In order to determine the bit error rate from the image data acquired then the detection of zero events on a pixel of the image that comprises part of the target object as measuring the absence of the target object, and the detection of ≥ 1 as measuring the presence of the object. The optimum classical strategy is found which minimises the bit error rate, this is performed for the target object as the ground truth is already known for the data presented.

The optimum classical strategy is determined by taking the sum of N thresholded frames and determining the value of N for which the bit error rate P_{err}^{C} is minimised for the given set of experimental conditions and with no assumption regarding the object or the noises present being made. In the case of quantum illumination the image we operate on is the sum of the result of performing the AND-operation between the reference and probe beams on a frame-by-frame basis. An event is therefore only added to the AND-image if there exists an anticorrelated event-pair in the regions of the camera frame on which the reference and probe beams are detected. In order to compare the bit error rates in a fair manner the images on which the bit error rate is determined should contain a similar number of events. Therefore for a classical image composed

of N frames an AND-image composed of $N/(p+d)$ frames is required. N, the number of frames which optimises the classical scheme may be suboptimal for the quantum illumination scheme, however, a systematic advantage is shown.

The bit error rate is evaluated by applying a mask of the UoG object to the classical image (composed of the sum of N frames), and the AND-image (composed of the sum of $N/(p+d)$ frames) and determining the number of the number of background pixels the feature a detection event (false positive) and the number of pixels that comprise the UoG object but have no detected events (false negative). This is performed on data taken under a range of light levels and the bit error rate presented in figure 4.6.

The theoretical values of the bit error rate for the classical image case P^C_{err} and the quantum case P^Q_{err} may be predicted. For the classical case assuming equal probability of the target object being present or absent and determining the rate on an image composed by the sum of N frames P^C_{err} may be written as in equation 4.6 in which $P^C_{Dark}(0) = 1-(d+T)$ is the probability of detecting zero events for a pixel in which the object is not present for a single frame and $P^C_{Bright}(0) = 1-(\varepsilon p+d+T)$ is the probability of detecting zero events for a pixel in which the object is present for a single frame.

$$P^C_{err} = \frac{1}{2}(1-P^C_{Dark}(0)^N) + \frac{1}{2}P^C_{Bright}(0)^N \tag{4.6}$$

For the quantum illumination AND-image case assuming equal probability of the target object being present or absent and determining the rate on an image composed by the sum of N frames P^Q_{err} may be written as in equation 4.7 in which $P^Q_{Dark}(0) = 1-(d+T)$ is the probability of detecting no events within the region of the sensor in which the probe beam is detected that correspond to a detected event in the momentum anticorrelated position within the region of the sensor in which the reference beam is detected for a pixel in which the object is not present for a single frame and $P^Q_{Bright}(0) = \frac{p}{p+d}(1-(\varepsilon\eta+T+d)) + \frac{d}{p+d}(1-(\varepsilon p+T+d))$ is the probability of detecting no events within the region of the sensor in which the probe beam is detected that correspond to a detected event in the momentum anticorrelated position within the region of the sensor in which the reference beam is detected for a pixel in which the object is present for a

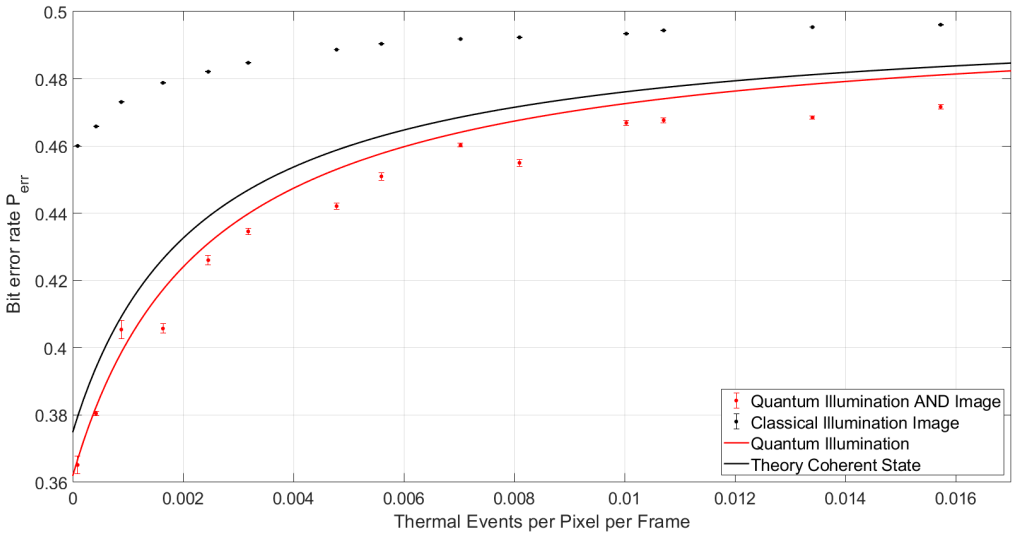

Figure 4.6: **The bit error rate P_{err} of detecting a target calculated over a range of thermal light levels using the blind strategy.** The classical data is represented by the black circles and the quantum illumination AND-image by the red circles. The black curve represents the theoretical optimum bit error rate for an image constructed from coherent state illumination. The red curve represents the curve for the theoretical optimum bit error rate for a quantum illumination AND-image calculated using the parameters of the experiment. The presented theoretical curves are valid for the blind strategy under the assumption of an unknown background illumination level and unknown target object and assuming Poissonian camera dark noise and thermal light. The error bars are the standard error on the mean for the calculated bit error rate.

single frame.

$$P^{Q}_{err} = \frac{1}{2}(1 - P^{Q}_{Dark}(0)^{N}) + \frac{1}{2}P^{Q}_{Bright}(0)^{N} \tag{4.7}$$

Equations 4.6 and 4.7 are used to plot theoretical curves alongside the experimental data presented in figure 4.6 in which the advantage in the probability of successfully determining the presence or absence of an object for quantum illumination may be seen over the range of thermal light levels.

The advantage in the bit error rate is based on the same mechanism as for the advantage obtained in contrast. For equal numbers of accumulated events for both the quantum illumination and the classical images possess the same background in the dark regions where the target object is not present and as a result the same error rate in predicting the absence of the target is calculated. The quantum illumination advantage in the bit error rate is due to an increased number of detected events in the bright parts of the images for the AND-images compared to

the classical images. The increased rate of detection results in a more accurate guess regarding the presence of the object. This increased intensity of the bright parts of the image alongside an identical background not only serves to increase the prediction accuracy but also means that the quantum illumination AND-image will exhibit a higher contrast than the classical image.

Non-Blind Strategy

The non-blind method entails knowing the target transmittance and noise as per Tan et al. (2008) [266]. The strategy here is to acquire frames to build an image and then find a threshold that minimises the bit error rate. This threshold may be calculated from the system parameters or through calibration of the system. Were the bit error rate of the AND-images to be compared with the classical images the bit error rate would be worse. This is because the AND-images are more noisy due to their containing fewer events than the classical image. With the complete data set acquired using the quantum illumination scheme the bit error rate of the classical case may be improved upon by using a combination of the classical images and the quantum illumination AND-images. This is similar to the optimal strategy for sub-shot noise measurements in which both correlated and uncorrelated data are used [262]. The strategy used to combine these images is to give more weight to the correlated events selected by the AND-operation than to the uncorrelated events contained within the classical sum. If the AND-image exhibits a contrast advantage compared to the classical image, then applying this strategy will lead to an improvement in the bit error rate when compared to that calculated for the classically acquired image. The optimal image upon which the bit error rate is assessed is then represented by a weighted sum of the classical image and the quantum illumination AND-image as represented in equation 4.8 in which the weight $(0 \leq s \leq 1)$ is dependent on the value of the reference arm efficiency η. The greater the AND-efficiency the more events I_{AND} that should be kept and the greater the value of s so if $\eta = 1$ then $s = 1$.

$$I_{Opt} = (1-s)I_{Average} + sI_{AND} \tag{4.8}$$

A quantum illumination advantage represented as a contrast advantage in I_{AND} means that a

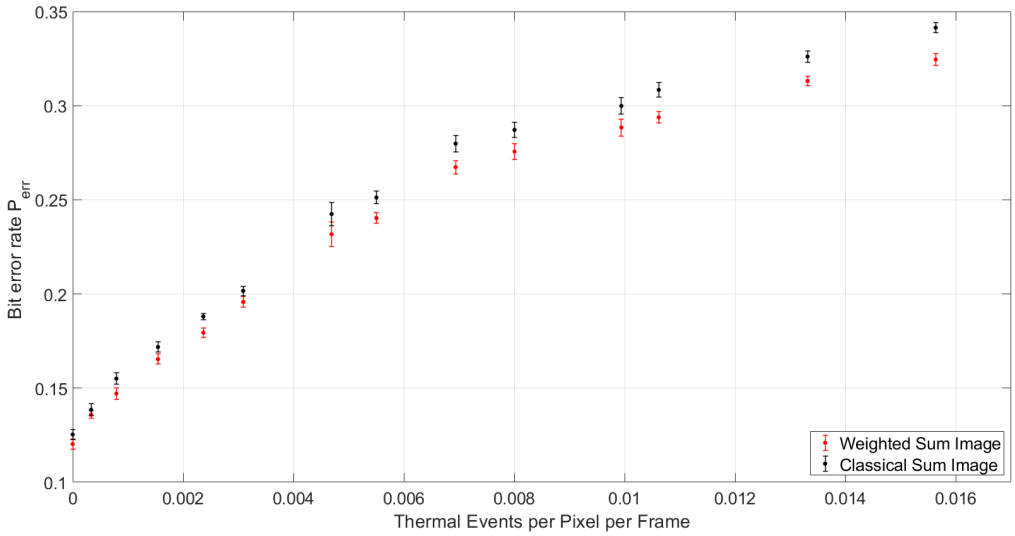

Figure 4.7: **The bit error rate P_{err} of detecting a target calculated over a range of thermal light levels using the non-blind strategy.** The purely classical data is represented by the black circles and the weighted sum of the classical image and the quantum illumination AND-image by the red circles. The error bars are the standard error on the mean for the calculated bit error rate.

strategy that is better than the classical strategy can be created and this means that an advantage in contrast through quantum illumination implies an advantage in the bit error rate.

For both images on which the bit error rate is assessed. The mean and standard deviations of the background pixels $(\mu_{bg} and \sigma_{bg})$ and the pixels that comprise the UoG object $(\mu UoG and \sigma_{UoG})$ are found and the threshold t is then set as per equation 4.9.

$$T = \mu UoG - n_{sd}\sigma_{UoG} = \mu_{bg} - n_{sd}\sigma_{bg}$$
$$\text{where} \tag{4.9}$$
$$n_{sd} = (\mu UoG - \mu_{bg})/(\sigma_{UoG} + \sigma_{bg})$$

The images are then thresholded accordingly and the bit error rate calculated. This is performed over a range of weights $s(0 \leq s \leq 1)$ and the minimum value for the bit error rate is determined for each light level. In figure 4.7 it may be seen that the advantage in the bit error rate is decreased compared to that calculated using the blind strategy detailed previously. The decreased advantage is due to a non-ideal reference arm efficiency, this results in a non-unity value for the weight value s.

4.4.3 Rejection of Structured Background

The quantum illumination protocol presented here may also be used to reject an arbitrarily structured and a-priori unknown background. Under such circumstances an ad-hoc background subtraction may not be performed due to uncertainties regarding which parts of the image correspond to the real object and which to the spoof object. In order to assess the distinguishability of the real target object from the spoof object both the contrast between the real and spoof objects and also the noise on the target object must be considered. The final image comprises the the quantum-illuminated target object, which has an average value of $\langle O \rangle$ above the background or dark portions of the image, and the spoof image which is the thermally illuminated structured background and has average value $\langle S \rangle$ above the background or dark portions of the image. The rejection of the spoof object in the form of structured illumination is characterised here as a ratio labelled as background rejection, $R_{Q/C} = \langle O \rangle / \langle S \rangle$. In order to assess the improvement that the quantum illumination AND-image possesses over the classically acquired image the ratio of the background rejection values $R_{Q/C}$ is assessed and named the rejection ratio RR as in equation 4.10.

$$RR = \frac{R_Q}{R_C} \tag{4.10}$$

The rejection ratio is able to assess the rejection of the thermal background illumination but it does not take into consideration the effect of shot-noise in the ability to distinguish the quantum-illuminated target object regions from the classically-illuminated spoof object regions. In order to better estimate the ability to distinguish the target object from the spoof object the shot-noise on the quantum-illuminated target object regions (σ_O) is taken into account as in equation 4.11.

$$D_{Q/C} = \frac{\langle O \rangle}{\langle S \rangle + \sigma_O} \tag{4.11}$$

In discussing the subject of noise a distinction here is made between noise that is internal to the image and the noise resulting from camera and environmental noise. The noise that originates from the detector or the environment may be preferentially rejected by performing the

AND-operation, while the image noise refers to image smoothness and therefore the number of events N registered in the image. A large number of frames are required to achieve image smoothness and reduce the value of $\sqrt{N}/N$ in the case of the quantum illumination AND-image. Therefore claims regarding the rejection of noise are made in reference to the rejection of detector and environmental noise as evidenced by the removal of the cage and net in figure 4.8, and do not refer to the noise within the image.

In figure 4.8 the bird and fish target objects are illuminated by the probe beam and the cage and net spoof objects are illuminated by thermal light. The spoof objects are present in the classically acquired image and the bird and fish are trapped but in the quantum illumination AND-image are released. This is because the cage and net are much reduced in intensity in the quantum illumination AND-image due to their being preferentially rejected as a result of the camera events from the thermal illumination of the cage and net events not possessing a pair-event in the reference beam that exhibits spatial correlations. For the bird in a cage image in figure 4.8 a rejection ratio RR of 4.2 is observed, and for the distinguishability D_Q/D_C a value of 1.3 is achieved.

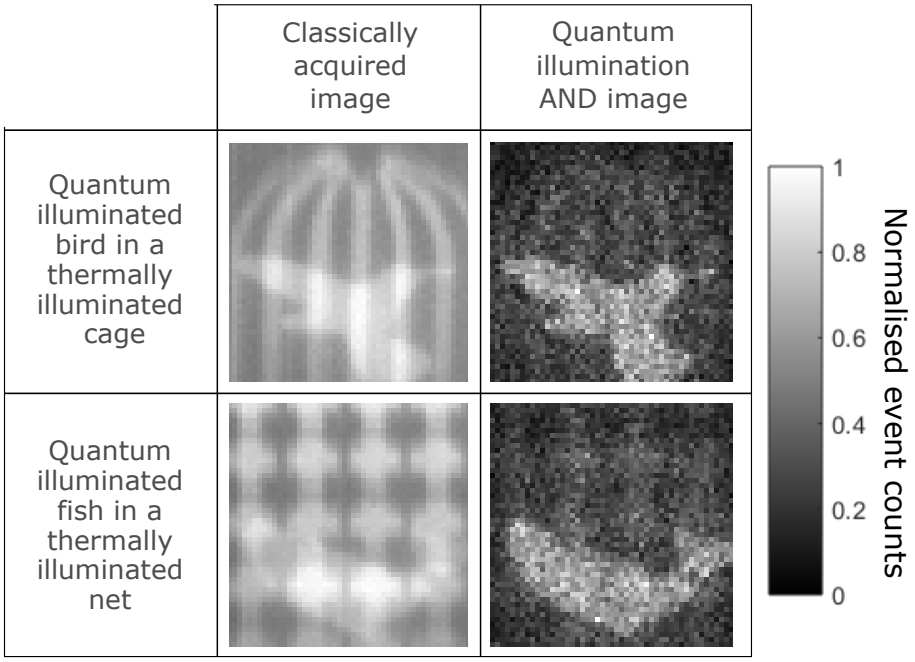

Figure 4.8: **Images of the rejection of structured thermal illumination.** Images of an object under quantum illumination overlaid with a thermally illuminated mask (left). By applying the AND-operation on the data, the quantum illuminated object may be separated from the thermally illuminated mask (right). In doing so the bird may be released from its cage (top), the fish released from its net (bottom). Images are 49×49 pixels.

Figure 4.9 displays the quantum illuminated bird trapped in a thermally illuminated cage under a range of increasing levels of thermal illumination. Under all levels of thermal illumination the prominence of the bars is much reduced in the quantum illumination AND-image when compared to the classically acquired image as can be seen in the cut through graphs alongside the figures. However, some of the bar structure remains visible in the quantum illumination AND-image as a result of random correlations being selected by the AND-operation. The rejection ratio, *RR*, for the images presented in this figure increase from 4.2 to 5.8 across as the level of thermal illumination increases from $\sim 0.5\times$ to $\sim 3.5\times$ the SPDC illumination level. The distinguishability ratio D_Q/D_C also increases from 1.35 to 3.87 with increasing thermal illumination of the cage. Therefore the quantum illumination AND-image presents an advantage over the classically acquired image in terms of distinguishability across the range of thermal illumination levels and also in the presence of losses as may be seen in the final row of figure 4.9. The distinguishability increases because the the quantum illumination AND-image does not contain all of the events that correspond to the thermally illuminated cage and as a result D_Q will decreases at a slower rate than does D_C.

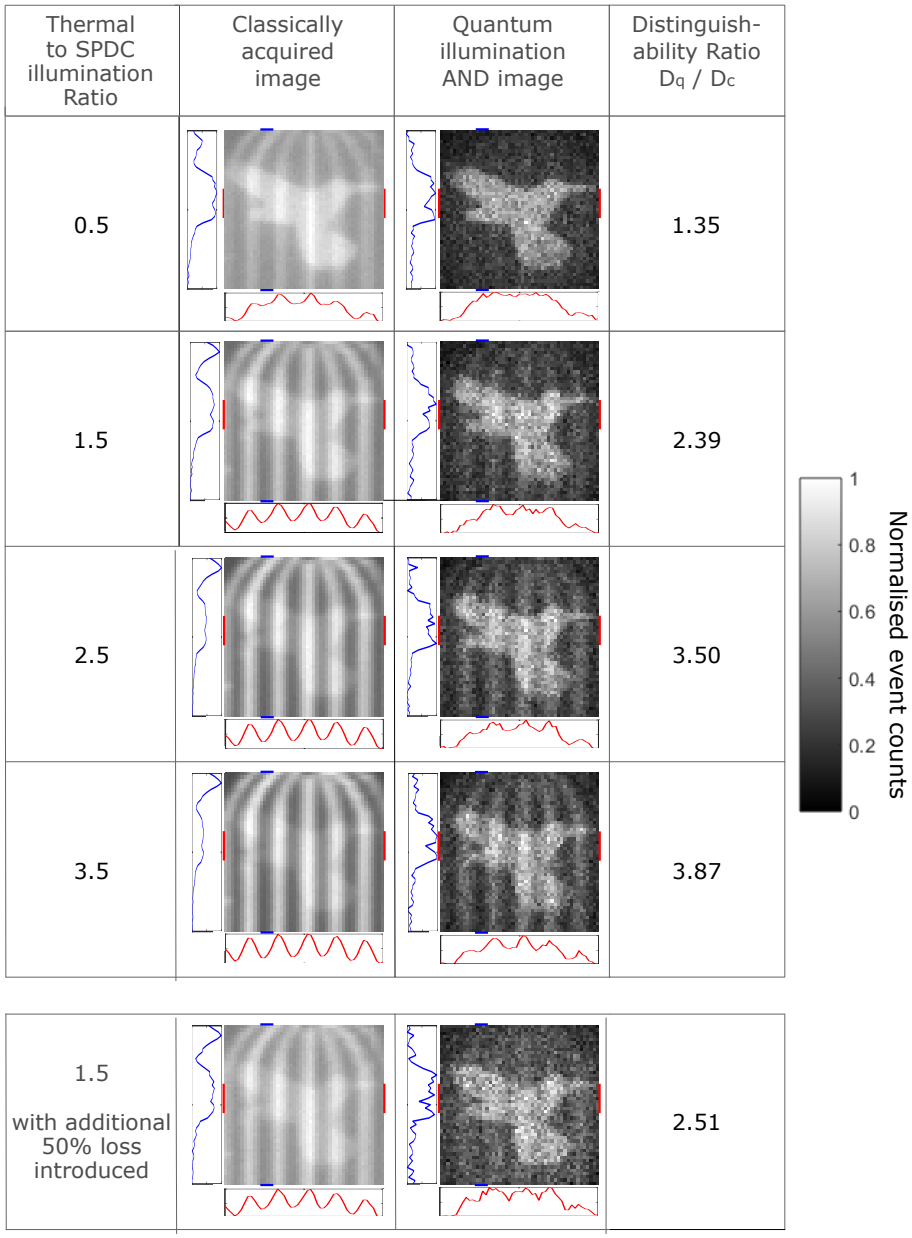

Figure 4.9: **Images of quantum illuminated object preferentially selected over thermally illuminated mask with increasing thermal illumination and the introduction of losses.** Images of the quantum illuminated bird overlaid with a thermally illuminated cage (left images). Quantum illumination AND-image obtained by applying the AND-operation on a frame-by-frame basis in which the quantum illuminated bird may be separated from the thermally illuminated cage (right images). By doing so the quantum bird is released from its classical cage across a range of increasing levels of thermal illumination. The relative level of thermal illumination to SPDC illumination is presented in the first column. In the bottommost row results for an acquisition in which optical losses of $\sim 50\%$ were introduced into the probe beam by means of an ND filter are presented. The distinguishability ratio D_Q/D_C calculated for each of these acquisitions is shown in the fourth column and may be seen to increase as the level of thermal illumination of the cage increases. The red lines on the images indicate the rows of the images that are used to generate the cut-through graphs as shown below the images. The blue lines on the images indicate the columns used to generate the cut-through graphs shown to the left of the images. Rows and columns used to generate the cut graphs are denoted by the red lines and blue lines on the images respectively are rows 19-27 and columns 12-15 for the images. Images are constructed over 2.5 million frames and are 49×49 pixels.

4.5 Discussion

In this chapter a quantum illumination protocol has been used to perform full-field imaging achieving a contrast enhancement through the suppression of both background-light and sensor noise. The results show that by utilising spatial correlations to construct an image using an AND-operation as a selection rule serves to preferentially select spatially correlated photon pair events and preferentially reject camera noise events. This protocol has also been shown here to reject a structured thermal background which is an a-priori unknown and therefore cannot be suppressed with a simple ad-hoc background subtraction. Through resilience to environmental noise and losses, such a quantum illumination protocol should find applications in real-world implementations which require a low-photon flux regime, situations in which environmental noise is high, or in covert imaging schemes. Therefore this demonstration of a quantum illumination full-field imaging protocol is an important development in the application of quantum technologies within a real-world setting in which background light and sensor noise requires suppression. Potential applications of a full-field quantum illumination protocol include quantum microscopy for low light-level imaging, quantum lidar imaging applications, and quantum radar.

The aforementioned applications of the quantum illumination protocol such as quantum lidar will become more viable as multi-pixel SPAD arrays that are capable of time-tagging single-photon events are further improved. The work presented in this chapter used an Andor iXon Ultra 888 with a single-frame acquisition time of ~ 0.015 s for our acquisition parameters and therefore is not applicable in the context of quantum lidar as such a system would have a depth resolution of 4.5×10^6 m. A SPAD array camera such as that developed by Gyongy et al. (2016) [363] will have an increased acquisition speed and time resolution with frame rates of 100 kfps and histogram bin sizes of down to 500 ps being achievable. Such specifications represent an increase at $10,000\times$ increase in the frame rate and an improvement of 3×10^7 in distance resolution. Such an improvement of around seven orders of magnitude in the temporal resolution of the detector would allow useful depth measurements of a scene to be made. An ability to time gate the detector using the specifications of the pump beam would also allow

further passive rejection of background illumination by virtue of not integrating the thermal illumination source over a time interval longer in duration than the pump pulse.

A classical analogue of the imaging protocol presented here would be to observe intensity correlations for an experiment in which a single beam is split into a reference and probe beam, or one in which a form of computational imaging is employed. The classical illumination can be modulated either temporally or spatially to enable intensity correlations to be used. Using the information regarding the known modulations of the probe beam the true signal could be distinguished from the spoof signal. These classical implementations would be subject to the limits observed in classical ghost imaging and computational ghost imaging including limitations in the shot-noise limited maximum achievable contrast and losses at digital light modulators [75, 194, 393].

Chapter 5

Noise Rejection Through An Improved Quantum Illumination Protocol

5.1 Introduction

The work presented in this chapter combines the classical image and the quantum illumination AND-image data to improve upon the results reported in the previous chapter. This is achieved through implementing an additional step into the analysis of the data and requires no additional acquisition to be performed beyond that which was required to produce the final quantum illumination AND-image as presented in the previous chapter. The application of the improved quantum illumination protocol presented in this chapter is again demonstrated through imaging a binary object under low-photon flux conditions. Under the conditions of low-photon flux the environmental noise and detector readout noise degrade the ability to distinguish the object from background light but through an improved imaging protocol $\gtrsim 99\%$ of the background illumination is rejected.

The improvement in the distinguishability ratio for the images obtained by implementing the improved imaging protocol is $\sim 27\times$ that of the corresponding classically acquired image and $\sim 11\times$ that of the corresponding quantum illumination AND-image. The improvement can be qualitatively seen in the resulting images by the near-complete rejection of the thermally illuminated spoof object present in the classically acquired images. All of the information necessary

to produce the images and achieve this improvement is acquired in a single acquisition and so no further data is required to calibrate the imaging system with regards to the background illumination level statistics or structure. This scheme is then demonstrated in the context of imaging a real-world biological object that is non-binary in transmission in the form of a wasp wing.

5.2 Methods

5.2.1 Imaging system

The experimental setup may be seen in figure 5.1 and is identical to the setup presented in the previous chapter in section 4.2.1. The optical system for the SPDC light, and the level of SPDC illumination is unchanged from that presented in the previous chapter. The pump beam is prepared prior to the downconversion crystal as described in section 2.2.

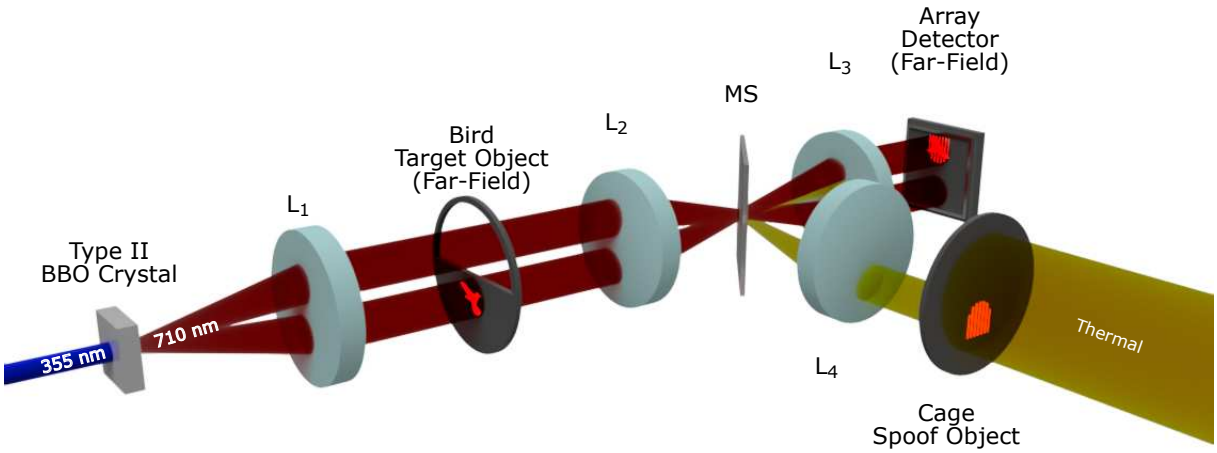

Figure 5.1: **The quantum illumination experimental setup.** A UV laser pumps a BBO crystal cut for type-II downconversion to generate entangled photon-pairs via SPDC. The probe beam interacts with the bird target object placed in the far-field of the crystal while the reference beam has a free optical path. The lens system $L_1 = 75$ mm, $L_2 = 400$ mm, and $L_3 = 50$ mm forms the arm in which the quantum light propagates and serves to demagnify the far-field plane in which the bird resides by a factor of eight onto the EMCCD camera array detector. A thermally illuminated cage spoof object is also projected onto the camera over the region on which the probe beam is detected using lenses $L_4 = 300$ mm and $L_3 = 50$ mm by reflection from the microscope slide slip cover (MS).

5.2.2 Image analysis

In order to preferentially select the camera events that correspond to spatially entangled photon-pair events and preferentially reject uncorrelated noise events, for each camera frame acquired a pixel-by-pixel AND-operation is performed between regions of interest that detect the reference beam and the probe beam. The photon-pair events are detected in the far-field and therefore of the regions of interest that correspond to the reference beam and the probe beam one must be rotated through an angle of π prior to performing the AND-operation being performed. As in Chapter 4 the result of performing the AND-operation on a frame-by-frame basis is summed to construct the quantum illumination AND-image I_{AND}. The classically acquired image of the probe beam I_C and the classically acquired image of the reference beam I_{ref} are constructed by summing all events that the detector registers above the analogue threshold. The measured correlation peak was found to extend beyond a single pixel as it is of FWHM of 3.51 ± 0.12 pixels. As a result a large proportion of the anti-correlated photon-pair events do not arrive in perfectly anticorrelated pixel positions on the detector. In order to collect the anticorrelated photon-pairs over the extent of the correlation peak, the AND-operation was performed on a 3×3 region about the central correlation position. For each position within the kernel the classical image of the probe beam I_C, the classical image of the reference beam I_{ref}, and the quantum illumination AND-image I_{AND} are obtained. Events that are found to have an anticorrelated partner are removed from the frames prior to performing the next step within the kernel in order to prevent double counting of the events in the AND-images. Section 6.2 provides further details regarding this integration of event-pairs over the extent of the peak and comparisons between different kernel sizes.

Performing the AND-operation not only serves to select event-pairs that correspond to entangled photon-pairs C_q but also selects event pairs that are the result of accidental correlations between uncorrelated events C_u and these two components comprise I_{AND} as in equation 5.1.

$$I_{AND} = C_q + C_u \tag{5.1}$$

The accidental correlations between events that do not correspond to entangled photon-pairs

are collected at a rate that is equal to the fill-factors of the corresponding pixels in the probe beam η_p and the reference beam η_{ref}. The contribution from accidental correlations C_u on a pixel-by-pixel basis in I_{AND} is as per equation 5.2.

$$\begin{aligned} C_u &= \eta_{ref}\eta_p\mathscr{N}_f \\ &= \eta_{ref}I_C \end{aligned} \tag{5.2}$$

In equation 5.2 $\mathscr{N}_f$ represents the number of acquired frames and $I_C = \eta_p\mathscr{N}_f$ equals the number of events registered in the corresponding pixel of the probe beam part of the sensor over the course of the acquisition which is equivalent to the classically acquired image. The fill-factor of the reference beam is derived from the classically acquired image of the reference beam and is data obtained within the same acquisition. No additional acquisitions or calibration steps are required to obtain this information.

Performing the subtraction operation to each of the AND-images as per equation 5.3 and combining them to form the final quantum illumination AND-image with accidentals subtracted a drastic improvement in the distinguishability was attained. This improvement is realised through the suppression of the accidental correlations that are associated with the classically spoof object regions.

$$I_{Sub} = I_{AND} - \eta_{ref}I_C \tag{5.3}$$

Removing the structured background is not something that can be achieved through an arbitrary background subtraction from the classically acquired image. This is because, without the additional information provided by the quantum illumination AND-image in conjunction with the reference beam image, it is not possible to ascertain which events correspond to the quantum illuminated target object and which events correspond to the classically illuminated spoof object.

5.3 Results

5.3.1 Rejection of structured thermal illumination

The advantage in noise rejection and distinguishability for the quantum illumination AND-image with accidentals subtracted relative to the classically acquired image for the bird in a cage images is assessed here. The noise rejection metric is defined as the ratio of the average value of the quantum-illuminated target object regions, $\langle O \rangle$, to the average value of the classically illuminated spoof object regions $\langle S \rangle$. The ability to distinguish the quantum-illuminated target object regions from the classically illuminated spoof object regions is also affected by the shot noise within the image and this is accounted for in the distinguishability metric by considering the shot noise on the quantum illuminated object regions, (σ_O). The distinguishability metric is defined in equation 5.4. Prior to assessing the noise rejection and distinguishability metrics for each of the images the average pixel value of the background regions of the images is subtracted from the image and the absolute values are used in calculating the noise rejection and distinguishability metrics.

$$D = \frac{\langle O \rangle}{\langle S \rangle + \sigma_O} \tag{5.4}$$

Figure 5.2 displays a series of images of the quantum illuminated bird target object within the classically illuminated cage spoof object. The ratios of thermal illumination of the classically illuminated cage to SPDC illumination of the quantum illuminated bird range from $\sim 0.5\times$ to $\sim 20\times$. It can be seen that the classical image (column 2) of the bird in the cage deteriorates as the ratio of thermal illumination to SPDC illumination is increased as the spoof image of the cage is visible across all illumination levels. The quantum illumination AND-image (column 3) is an improvement over the classically acquired image in that the relative intensity of the thermally illuminated cage object is reduced when compared to that of the quantum illuminated bird object. This improvement is a result of the AND-operation preferentially selecting spatially correlated photon-pairs and preferentially rejecting background light and sensor noise. However, the classically illuminated cage object remains visible to some extent due to accidental correla-

tions also being kept. In subtracting the accidental correlations the bird can be released from its prison across all illumination levels presented here as can be seen in the quantum illumination AND-image with accidentals subtracted (column 4).

Thermal vs SPDC Brightness	Classically acquired Image	Quantum Illumination AND-Image	Quantum Illumination AND-Image with Accidentals Subtracted	Distinguishability Ratio		
				$\frac{D_{AND}}{D_{Classical}}$	$\frac{D_{Sub}}{D_{Classical}}$	$\frac{D_{Sub}}{D_{AND}}$
0.5				1.50	1.47	0.98
0.7		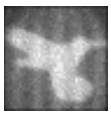		2.22	2.76	1.24
1.1		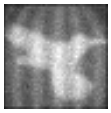		2.58	3.53	1.37
1.6		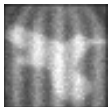		3.26	6.93	2.13
2.0		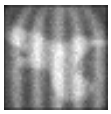		3.44	8.25	2.40
3.6	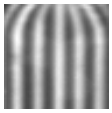	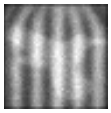		4.28	16.93	3.96
7.3	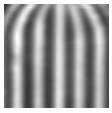	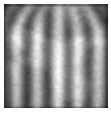		4.28	26.94	6.29
14.1	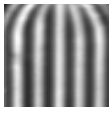	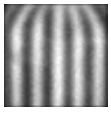		2.78	24.40	8.78
19.3	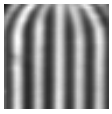	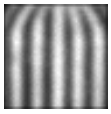		2.03	21.91	10.79

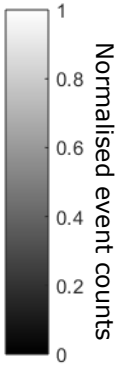

Figure 5.2: **Images of the classically acquired image, the quantum illumination AND-image, and the quantum illumination AND-image with accidentals subtracted for the bird in a cage** Images of the classically acquired image, the quantum illumination AND-image, and the quantum illumination AND-image with accidentals subtracted alongside their corresponding improvements in the distinguishability metric relative to that of the classically acquired image. Images constructed over 2.4 million frames.

For the range of thermal illumination to SPDC illumination ratios presented here the ratio of the distinguishability of the quantum illumination AND-image with accidentals subtracted compared to the classical image $D_{Sub}/D_{Classical}$ (column 6) is larger than that for the corresponding quantum illumination AND-image compared to the classical image $D_{AND}/D_{Classical}$ (column 5). The ratio D_{Sub}/D_{AND} is presented in column 7 and increases as the thermal illumination to SPDC illumination ratio increases and shows an improvement of up to a factor of ~ 11 when the thermal illumination to SPDC illumination ratio is $\sim 20\times$. The increased distinguishability ratio of the quantum illumination AND-image with accidentals subtracted relative to the quantum illumination AND-image demonstrates the advantage of combining the quantum information and the classical information as opposed to solely using either set of alone.

The distinguishability ratios decrease as the ratio of thermal illumination relative to SPDC illumination increases from $\sim 7\times$ to $\sim 20\times$. The decrease in the distinguishability ratio is due to spillage of background light from the thermally illuminated cage regions into the regions of the image that are designated as belonging the quantum illuminated bird and into the background regions of the image. In the case of a high ratio of thermal illumination relative to SPDC illumination pixels that are designated to comprise the bird object and which have n_{bird} real events incident upon the detector, this value is low enough such that it falls within the noise of the background regions $\sigma_{background}$ which affects the measured distinguishability of the classically acquired images. The ratio of distinguishabilities for the quantum illumination AND-image with accidentals subtracted compared to the quantum illumination AND-image D_{Sub}/D_{AND} continues to increase from 6 to 11 over this range of thermal illumination to SPDC illumination.

For the quantum illumination AND-image and the quantum illumination AND-image with accidentals subtracted images the cage rejection relative to the classically acquired image may be quantified and the values presented in Table 5.1. It can be seen that performing the AND-operation serves to reject $> 97\%$ of the background light across the range of thermal illumination to SPDC illumination ratios presented here, however the remaining events in the regions of the image that correspond to the cage are still present to a great enough extent such that the bird remains obscured for the higher ratios. For the quantum illumination AND-image with accidentals subtracted images the cage rejection is $\gtrsim 99.9\%$ across the range of thermal illumination to

Thermal background to SPDC ratio	Quantum illumination AND-image	Quantum illumination AND-image with accidentals subtracted
0.5	2.91e-02	1.04e-03
0.7	2.86e-02	9.21e-04
1.1	2.76e-02	8.36e-04
1.6	2.78e-02	7.27e-04
2.0	2.70e-02	7.09e-04
3.6	2.67e-02	4.88e-04
7.3	2.57e-02	3.46e-04
14.1	2.43e-02	3.06e-04
19.3	2.39e-02	1.92e-04

Table 5.1: **Table of the proportion of the thermally illuminated cage that remain in the quantum illumination AND-image and the quantum illumination AND-image with accidentals subtracted.** The ratio of average pixel value for the regions of the image that corresponds to the cage object for the quantum illumination AND-image (column 2) and the quantum illumination AND-image with accidentals subtracted (column 3) relative to the classically acquired image.

SPDC illumination ratios.

From 5.2 it can be seen that that the quantum illumination AND-image and the quantum illumination AND-image with accidentals subtracted both exhibit greater shot-noise than the classically acquired image. This increased noise internal to the image is due to the images containing far fewer events than the classically acquired image. For the quantum illumination AND-image with accidentals subtracted this noise within the image increases as the thermal illumination to SPDC illumination increases due to the number of events per pixel n, and the associated shot noise $\sqrt{n}$, increasing within the classically acquired image. The fluctuations within the classically acquired image are introduced into the quantum illumination AND-image with accidentals subtracted when the subtraction operation is performed to combine the classically acquired image and the quantum illumination AND-image and results in a final image with increased shot-noise. This increased noise within the final quantum illumination AND-image with accidentals subtracted is evident in the bottom two rows of figure 5.2. This also has the effect of reducing the average intensity of the quantum illuminated bird object regions as the thermal illumination to SPDC illumination increases due to the intensity of the bird increasingly residing within the noise of the thermally illuminated spoof object regions and the additional background light that spills into the quantum illuminated bird object regions and background

Thermal background to SPDC ratio	Classically acquired image	Quantum illumination AND-image	Quantum illumination AND-image with accidentals subtracted
0.5	6996.33	302.77	89.78
0.7	6944.55	302.03	89.92
1.1	7044.14	295.70	84.99
1.6	7752.13	330.67	90.53
2.0	7884.09	322.89	83.89
3.6	9577.95	383.19	84.01
7.3	12727.23	481.34	77.90
14.1	18184.50	650.08	74.58
19.3	23606.03	834.58	73.77

Table 5.2: **Table of the average number of events in the pixels that correspond to the regions of the final images that solely correspond to the quantum illuminated bird.** The average number of events in the pixels that correspond to the quantum illuminated bird regions for the classically acquired image (column 2), the quantum illumination AND-image (column 3), and the quantum illumination AND-image with accidentals subtracted (column 4).

regions of the image. This trend may be seen in Table 5.2 in which the average number of events per pixel in the regions of the image that correspond to the quantum illuminated bird decreases as the thermal illumination to SPDC illumination ratio increases for the quantum illumination AND-image with accidentals subtracted. For the quantum illumination AND-image the average number of events per pixel in the regions of the image that correspond to the quantum illuminated bird increase as the thermal illumination to SPDC illumination ratio increases due to an increased rate of accidental correlations due to the increased thermal background light.

5.3.2 Noise Rejection in Imaging a Complex Object

The improved quantum illumination protocol is demonstrated in the context of imaging a complex biological object. The object in question is a wasp wing which is a non-binary object with regards to its transmission profile. Furthermore, in order to demonstrate the ability to reject noise, thermal illumination at a thermal to SPDC illumination ratio of ~ 1.5 that has passed through a dirty and scratched microscope slide is overlaid onto the region of the camera that detects the probe beam. The resulting images are presented in fig. 5.3 in which it may be seen that the wing and its structure are hardly visible. In the quantum illumination AND-image which

represents the correlated event pairs in the reference beam and the probe beam some structure becomes visible but with a low contrast due to the incomplete rejection of the background light. In the case of the quantum illumination AND-image with accidentals subtracted the internal structure of the wing becomes clear and is visible with a high contrast as the thermal light and the features of the scratched microscope slide are largely removed.

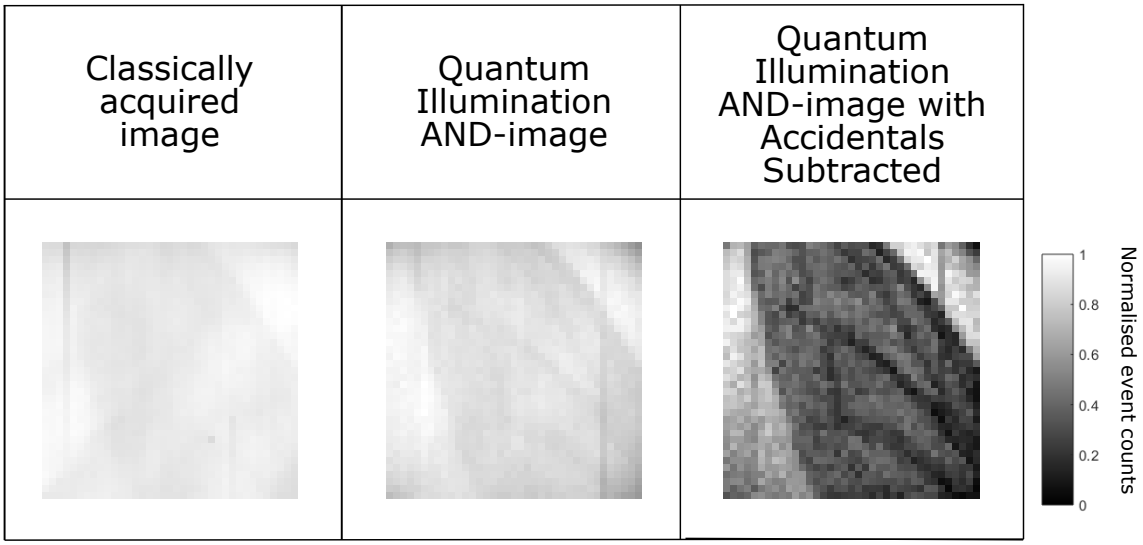

Figure 5.3: **Images of a wasp wing.** The classically acquired image (left), quantum illumination AND-image (centre), the quantum illumination AND-image with accidentals subtracted by combining the quantum and classical data (right). The images were constructed over 87.7 million frames.)

5.4 Discussion

Here we demonstrated a significant improvement with regards to achievable background light and sensor noise rejection for a full-field quantum illumination protocol in a single photon regime. This was achieved using information that was already acquired within the acquisition. The method of combining the quantum and classical information presented here may be limited in environments in which the background light signal is low or the heralding efficiency is high because then the shot-noise on the classical image will be close to that on the quantum illumination AND-image. This limitation is because in such cases performing a subtraction will lead to reduced image quality in the form of image noise and thereby hinder the ability to distinguish the object in the quantum illumination AND-image with accidentals subtracted relative

to the quantum illumination AND-image. As a result the quantum illumination imaging scheme that we present here is adapted well for adverse imaging conditions of a strong background and high losses, however, as the level of adversity increases so does the number of frames required. These results strengthen the case for quantum illumination protocol implementation in a variety of fields in which the effects of noise and spoofing of an image or scene may prove troublesome. This result allows the quantum signal to be extracted from the detected signal over a large range of and therefore offers routes for the implementation of the quantum illumination protocol in real-world environments for the purposes of realising covert imaging schemes, quantum lidar, and quantum radar. Such applications will become more viable as spatially resolved SPAD arrays [363] continue to improve with regards to speed and time resolution which will allow accurate time-of-flight measurements to be performed in a spatially resolved manner. The drastic improvements shown here can allow one to more easily imagine quantum imaging technologies based on the quantum imaging protocol to find real-world applications in which sensor noise, background illumination, and active spoofing or jamming signals need to be suppressed.

Chapter 6

Improved Data Extraction Techniques

6.1 Introduction

Due to the extent of the correlations in the plane of the camera not all entangled photon-pair events are selected by performing the bitwise AND-operation. As a result, the maximum achievable AND-efficiency of the system is reduced from a theoretical maximum of $\sim 17\%$ (in the case of the uncertainty in the position of the photons being less than the size of a pixel on our detector) to $\sim 1.8\%$ for the experimental setup presented in this thesis. Due to the reduced efficiency a number of ways in which the efficiency of the system could be increased and the final images improved have been considered and are presented in this chapter.

6.2 Integrating Correlations Over Extent of Peak

The correlation peak as shown in figure 2.5 has a FWHM of 3.51 pixels and therefore the correlated photon-pair events are not all represented in the AND-image. For a Gaussian distribution of $\sigma_x = 1.29$, $\sigma_y = 1.70$, average $\sigma = 1.49$ pixels the proportion of the Gaussian that falls within the 1, 3, and 5 pixel kernels are presented in table 6.1. The proportion of photons-pairs that are expected to be collected by integrating over kernels of size 1, 3, and 5 pixels are presented in table 6.1.

This integration may be performed by shifting one of the ROIs and performing additional

Kernel Size	Proportion of Gaussian within Kernel
1×1	10.19%
3×3	61.17%
5×5	91.90%

Table 6.1: **Table of the proportion of a Gaussian with widths of $\sigma_x = 1.29$ and $\sigma_y = 1.70$ contained within a kernel of 1, 3, and 5 pixels.**

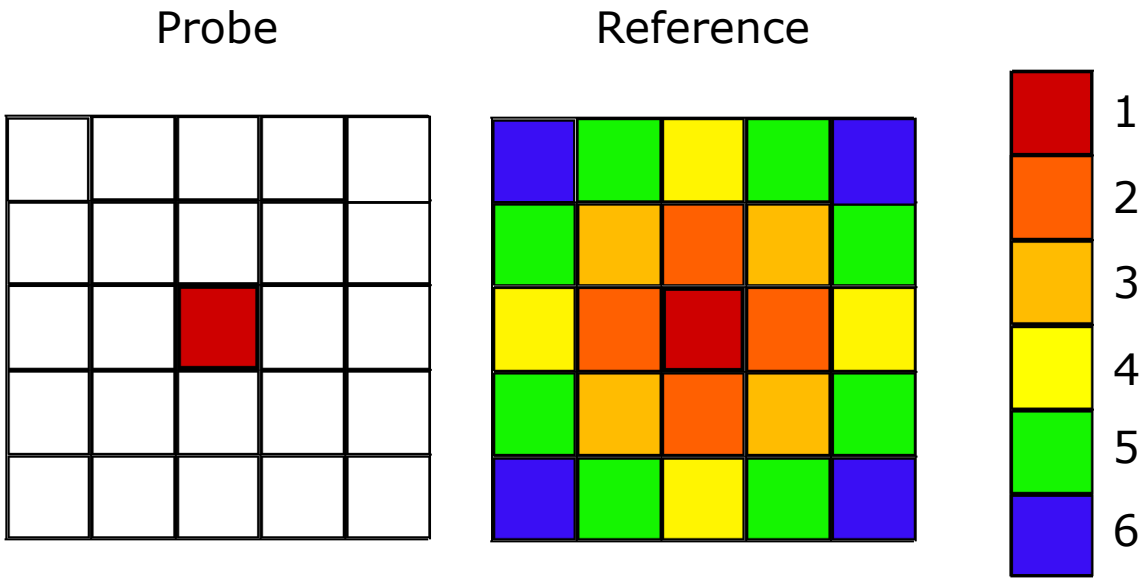

Figure 6.1: **Figure displaying the order of the offsets for integrating the correlations over the extent of the correlation peak.** The AND-operation is performed for offsets in the labelled numerical order and once an event-pair is found the events are removed prior to performing subsequent steps.

AND-operations allows the collection of the pair-events that are not exactly anticorrelated in position. Once a correlation is found the events are masked out prior to the next step of the ROIs and therefore no double counting of events is performed. The AND-image resulting from this integration of the correlations will therefore be the sum of multiple images with the offsets as defined by the steps required to perform the integration as shown in figure 6.1. The increase in the proportion of events that are collected for a 3×3 kernel will be $6\times$ and for a 5×5 kernel up to $9\times$. The AND-image resulting from this integration of the correlations will therefore be the sum of multiple images with the offsets as defined by the steps required to perform the integration as shown in figure 6.1.

6.2.1 Contrast Enhancement

For the UoG object this analysis method was applied and the contrast of the resulting images assessed for the data obtained under differing levels of thermal illumination and losses. In this case the peak integration was performed in order to ascertain whether this method of analysis would result in an improvement in the quantum illumination advantage due to an increased number of AND-events that correspond to real SPDC photon-pair events. The images on which the contrast is assessed are 37×37 pixels in size. The smaller image size is used in order to crop out the border regions that are introduced in combining the multiple images constructed at each step of the peak integration. As a result the contrasts of the individual images presented may differ slightly from those presented in chapter 4.

Using both the 3×3 and the 5×5 kernel results in a reduced contrast relative to the the simple AND-analysis method as described and utilised in chapter 3 and 4. The array of images of the UoG object under differing levels of thermal illumination demonstrating this are presented in figure 6.2 and under differing levels of loss in figure 6.3. The reduction in the contrast is due to the fact that of the 9 in the case of a 3×3 kernel, or 25 in the case of a 5×5 kernel, images that are summed to construct the final AND-image each of the offset AND-images that do not correspond to the central correlation have a reduced contrast and therefore the raw sum of these images can only result in a final AND-image of reduced contrast.

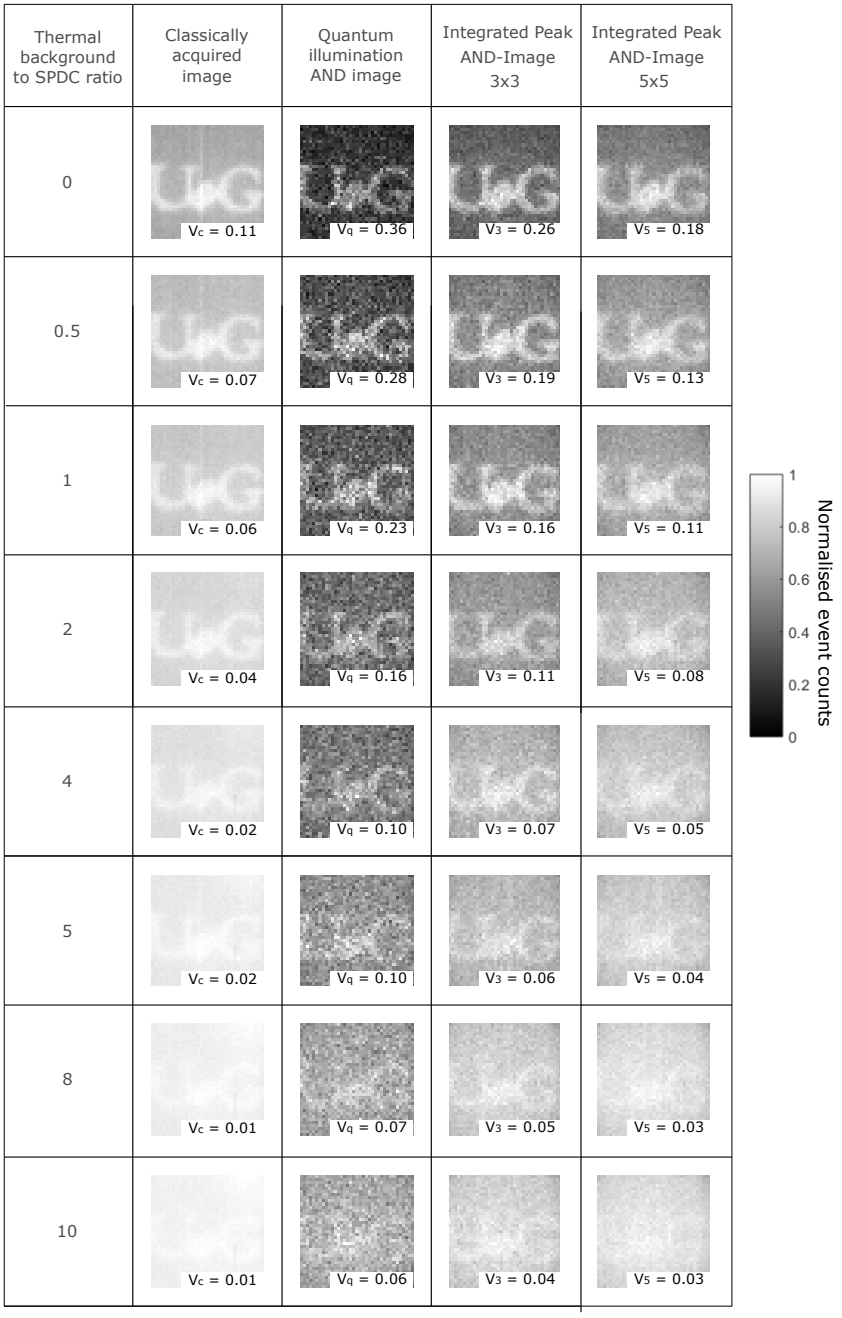

Figure 6.2: **Comparison of images resulting from performing the original AND-operation and the peak integration method for the UoG object under differing levels of thermal illumination.** The images obtained by the original AND-analysis method (2nd column) compared to the new peak integration AND-analysis method for a 3×3 kernel (3rd column) and a 5×5 kernel (4th column). Image contrast inset in bottom right of respective image. Images constructed over 1.4 million frames.

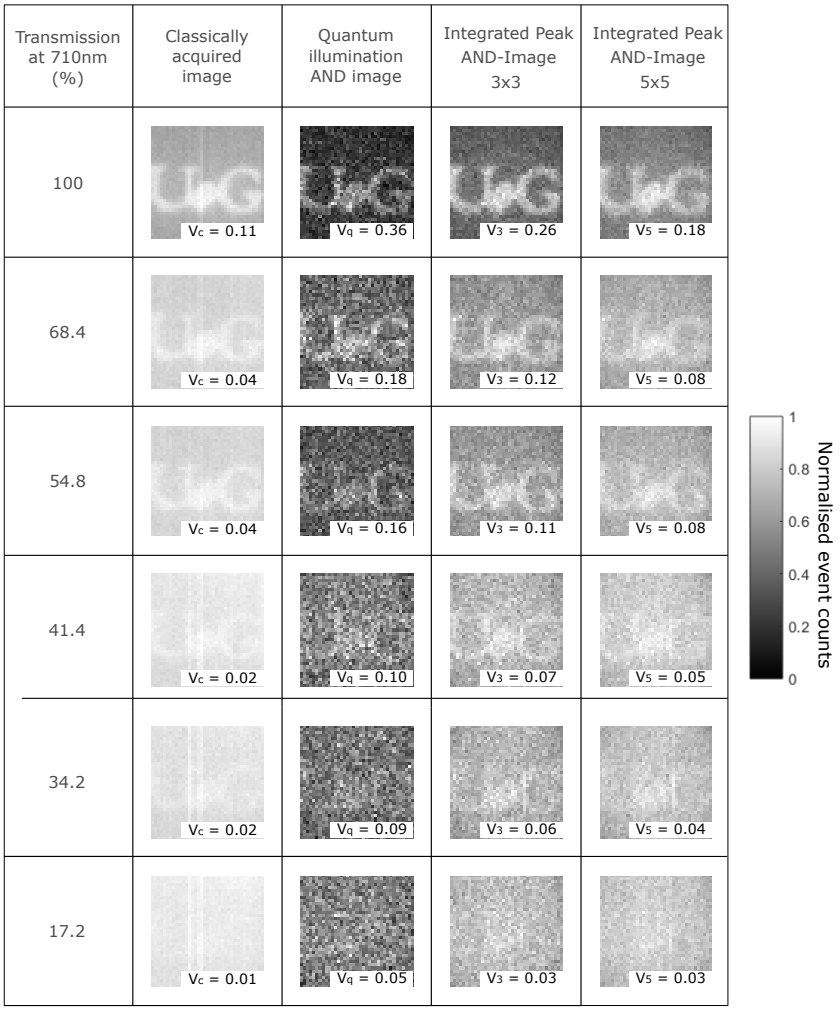

Figure 6.3: **Comparison of images resulting from performing the original AND-operation and the peak integration method for the UoG object under differing levels of loss in the probe beam.** The images obtained by the original AND-analysis method (2nd column) compared to the new peak integration AND-analysis method for a 3×3 kernel (3rd column) and a 5×5 kernel (4th column). Image contrast inset in bottom right of respective image. Images constructed over 1.4 million frames.

After performing the subtraction, however, there exists an advantage in performing the peak integration method as the additional noise that degrades the contrast in the additional offset images can be removed. However, there is a degradation in the contrast of the final image contrast in the case of the 5×5 kernel subtraction image relative to the 3×3 kernel subtraction image. This is because the ratio of the SPDC signal to the noise on the thermal background light is reduced as the level of thermal illumination or losses is increased and the signal then eventually begins to lie within the noise of the background light. The addition of the extra images then serves only to add noise to the final resulting image. The array of images of the UoG object under differing levels of thermal illumination demonstrating this are presented in figure 6.4 and under differing levels of loss in figure 6.5.

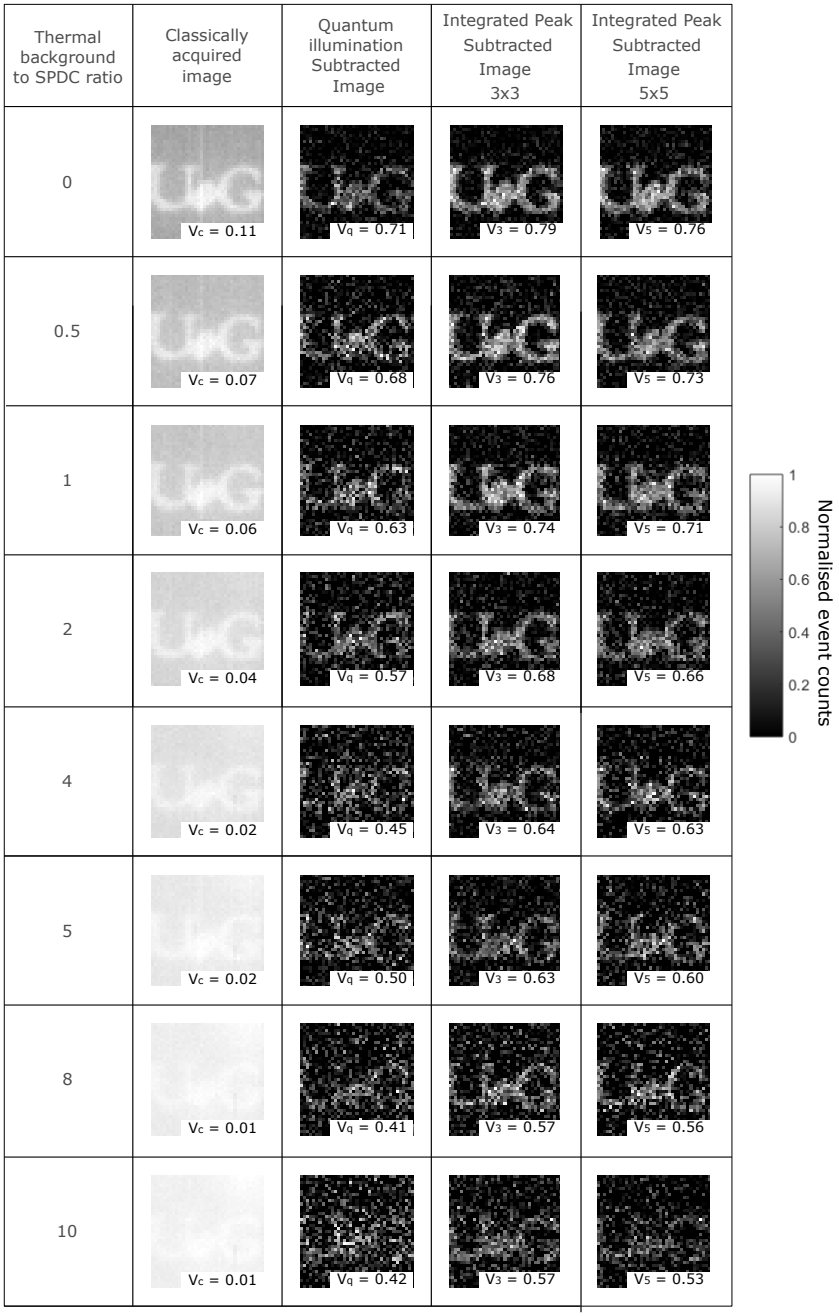

Figure 6.4: **Comparison of images resulting from performing the subtraction operation after applying the peak integration method for the UoG object under differing levels of thermal illumination.** The images obtained by the original AND-analysis method (2nd column) compared to the new peak integration AND-analysis method for a 3×3 kernel (3rd column) and a 5×5 kernel (4th column). Image contrast inset in bottom right of respective image. Images constructed over 1.4 million frames.

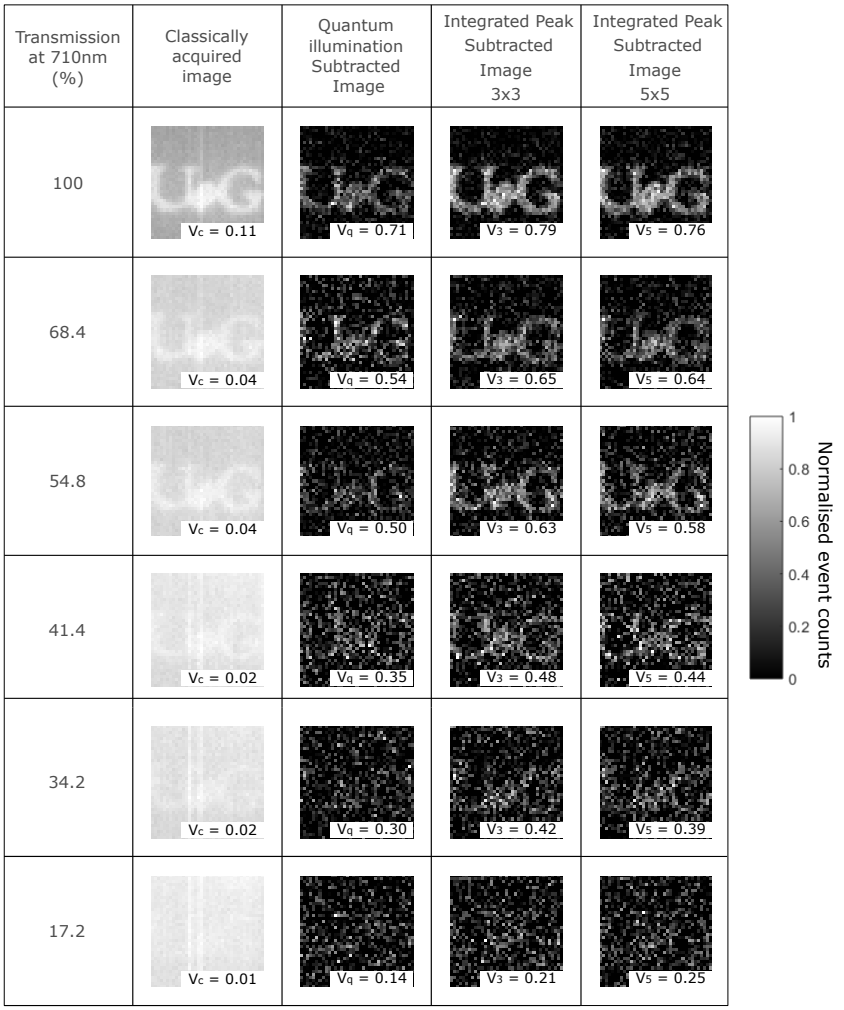

Figure 6.5: **Comparison of images resulting from performing the subtraction operation after applying the peak integration method for the UoG object under differing levels of loss in the probe beam.** The images obtained by the original AND-analysis method (2nd column) compared to the new peak integration AND-analysis method for a 3×3 kernel (3rd column) and a 5×5 kernel (4th column). Image contrast inset in bottom right of respective image. Images constructed over 1.4 million frames.

6.2.2 Noise Rejection

For the bird in a cage object this analysis method was applied and the distinguishability of the resulting images assessed for the data obtained under differing ratios of thermal illumination to SPDC illumination. The peak integration was performed in order to ascertain whether this method of analysis would result in an improvement in the quantum illumination advantage due to an increased number of AND-events that correspond to real SPDC photon-pair events. The images presented and on which the contrast is assessed are 45×45 pixels in size. The smaller image size is used in order to crop out the border regions that are introduced in combining the multiple images constructed at each step of the peak integration. As a result the distinguishabilities of the individual images presented differ from those presented in chapter 4 and 5.

In the case of the AND-image, the peak integration method results in a reduced distinguishability relative to the simple AND-analysis method as described and utilised in chapter 3 and 4. The array of images of the bird in a cage at differing ratios of thermal illumination to SPDC illumination demonstrating this are presented in figure 6.6. The corresponding distinguishabilities are presented in table 6.2 and show a reduction as the size of the kernel for the peak integration increases. This is due to the fact that of the 9 in the case of a 3×3 kernel, or 25 in the case of a 5×5 kernel, images that are summed to construct the final AND-image, each of the offset AND-images that do not correspond to the central correlation have a reduced ratio of pair events that correspond to the bird to those that correspond to the cage and therefore the sum of these images can only result in a final peak integration AND-image of reduced distinguishability relative to the image that contains pair events corresponding to the central correlation as in case of the 1×1 kernel.

	Distinguishabilities		
Thermal background to SPDC ratio	1×1	3×3	5×5
0.5	2.08	2.81	2.59
0.7	1.99	2.27	2.24
1.1	1.52	1.75	1.77
1.6	1.30	1.22	1.23
2.0	1.10	0.97	0.97
3.6	0.67	0.53	0.13
7.3	0.35	0.25	0.25
14.1	0.19	0.13	0.15
19.3	0.13	0.10	0.13

Table 6.2: **Table of distinguishabilities for the bird in a cage images created by performing the original AND-operation and the peak integration method for the bird in a cage object under differing levels of thermal illumination.** Distinguishabilities are presented for peak integration AND-images for the range of ratios of the thermal illumination to SPDC illumination for kernel sizes of 1×1, 3×3, and 5×5.

As with the UoG object data presented above, implementing the peak integration method in conjunction with the subtraction algorithm allows the increased number of accidental correlations that cause the reduction in distinguishability in the peak integration AND-image to be removed. The distinguishabilities for the peak integration subtracted image are presented in table 6.3 in which the maximum achievable distinguishability for each data set is found to be using the 3×3 kernel for the same reasons as stated above for the peak integration subtraction images of the UoG object. This is the kernel size used in chapter 5.

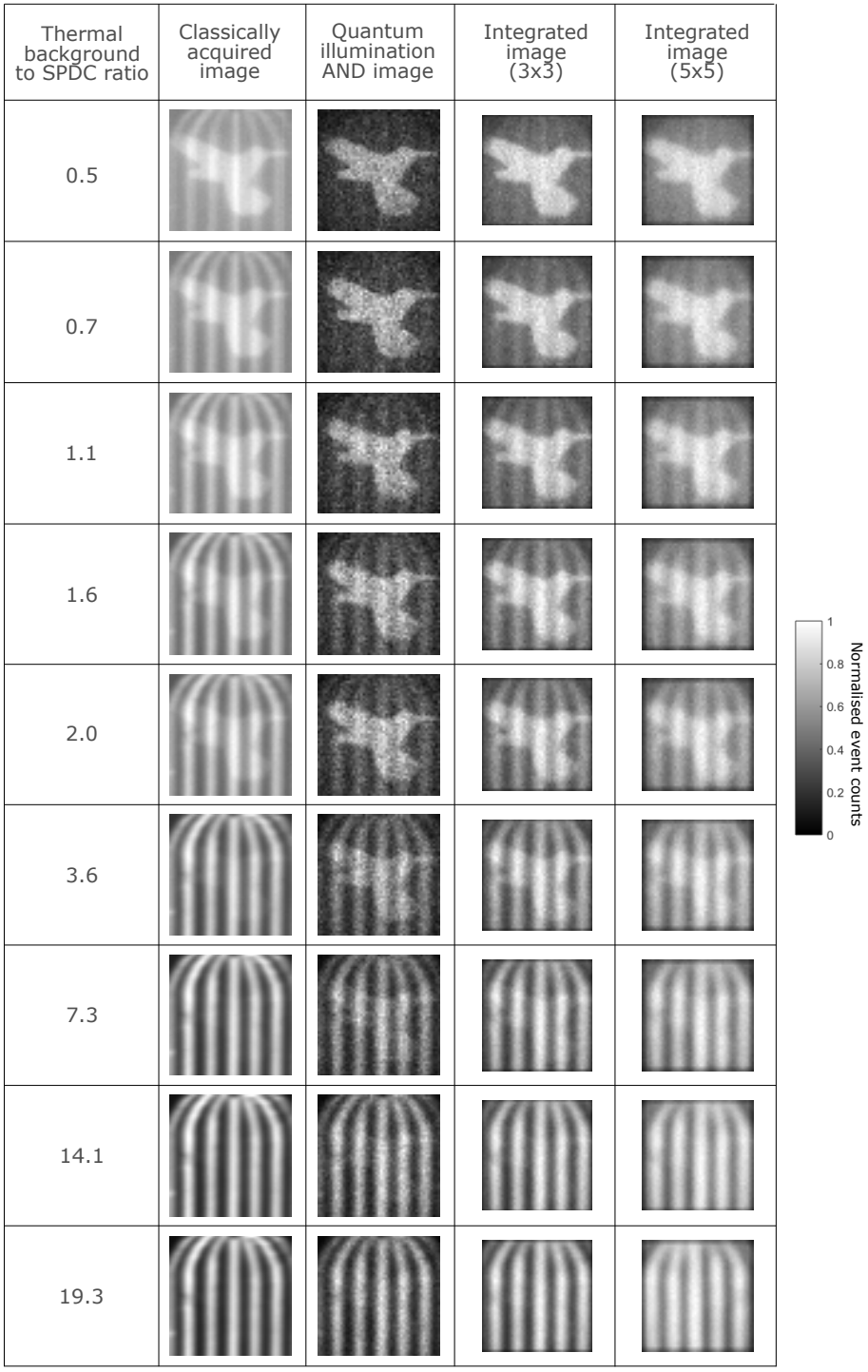

Figure 6.6: **Comparison of images created by performing the original AND-operation and the peak integration method for the bird in a cage object under differing levels of thermal illumination.** Images constructed by performing the original AND-analysis method (2nd column) and the new peak integration AND-analysis method using a 3×3 kernel (3rd column) and a 5×5 kernel (4th column). Images constructed over 2.4 million frames.

	Distinguishabilities		
Thermal background to SPDC ratio	1×1	3×3	5×5
0.5	1.85	2.62	2.46
0.7	1.85	2.64	2.47
1.1	1.57	2.28	2.13
1.6	1.77	2.57	2.47
2.0	1.67	2.34	2.10
3.6	1.51	2.26	2.06
7.3	1.29	1.79	1.56
14.1	1.02	1.37	1.23
19.3	1.00	1.29	1.22

Table 6.3: **Table of distinguishabilities for the bird in a cage images constructed by implementing the peak integration method and the subtraction operation.** Distinguishabilities are presented for peak integration subtracted images for the range of ratios of the thermal illumination to SPDC illumination for kernel sizes of 1×1, 3×3, and 5×5.

For peak integration subtraction image, the mean and standard deviation of the bird regions of the image are presented in table 6.4. The average improvement in the distinguishabilities in the subtracted images constructed by performing the AND-operation over a 1×1 kernel to a 3×3 kernel is ~ 1.4. This corresponds to the ratio $\langle O/rangle/\sigma_O$ which is effectively the distinguishability ratio for images where the cage is removed as is the case in figure 6.7. These values of $\langle O/rangle$ and σ_O for the three kernel sizes are present in table 6.4. The mean values for each kernel are consistent up to a thermal background to SPDC illumination ratio of 14.1 for the 1×1 kernel, and 7.3 for the 3×3 and 5×5 kernel. The subtraction method can therefore be seen to effectively remove the accidental correlations and keep the true correlations but as the level of thermal illumination increases the SPDC signal lies within the noise that has spilled into the background regions and a greater proportion is lost in performing the background subtraction prior to calculating these values.

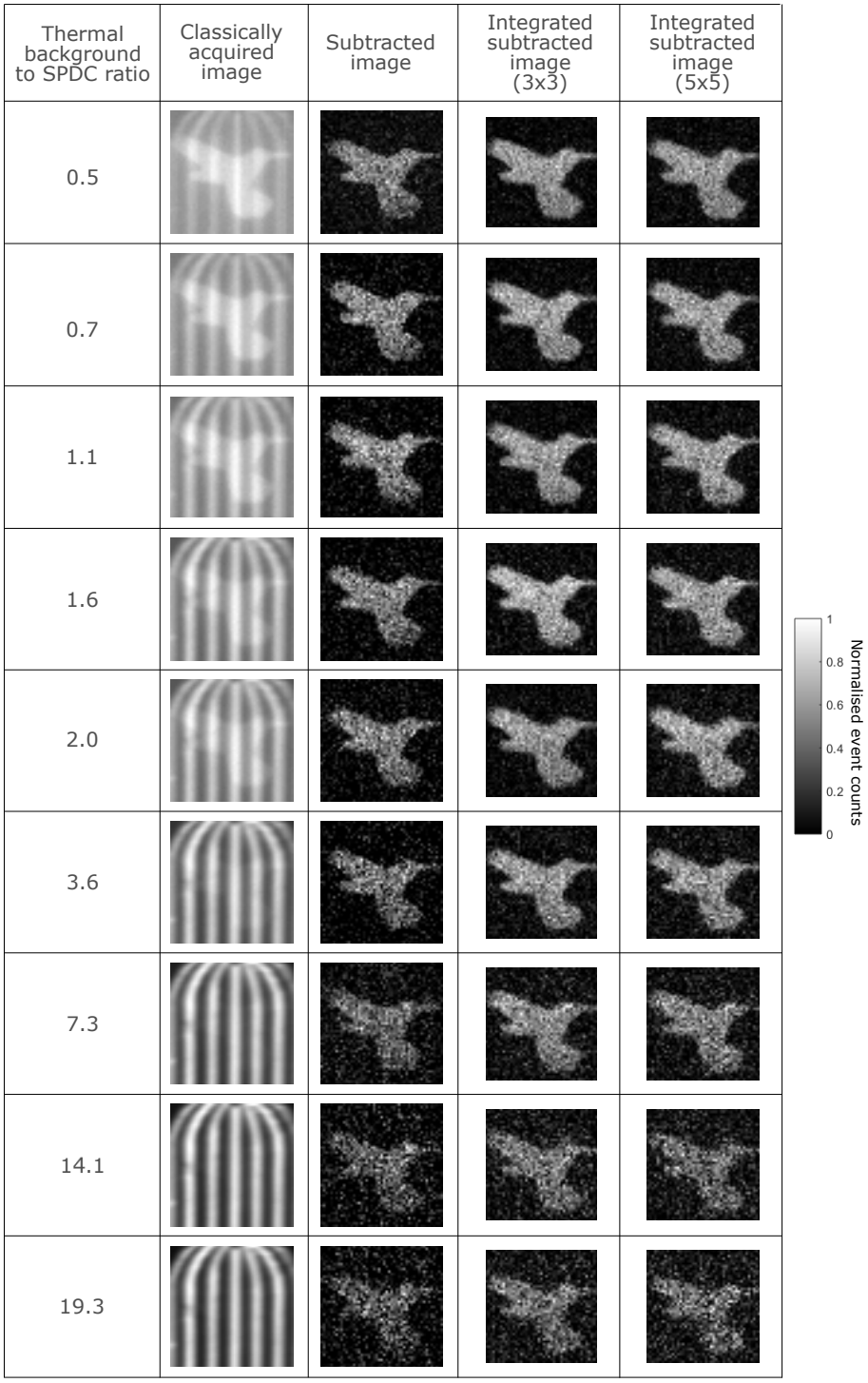

Figure 6.7: **Comparison of images resulting from performing the subtraction operation in combination with the peak integration method for the bird in a cage object under differing levels of thermal illumination.** Images constructed by performing the subtraction method on the original AND-image (2nd column) and the new peak integration AND-analysis method using a 3×3 kernel (3rd column) and a 5×5 kernel (4th column). Images constructed over 2.4 million frames.

	1×1		3×3		5×5	
Thermal background to SPDC ratio	μ_1	σ_1	μ_3	σ_3	μ_3	σ_5
0.5	20.91	7.74	90.99	23.96	127.87	34.91
0.7	20.69	7.77	89.08	24.11	124.62	34.49
1.1	19.69	8.20	86.97	24.10	120.25	34.45
1.6	20.22	8.23	89.86	24.17	125.58	35.37
2.0	19.21	8.31	85.59	24.49	118.10	35.15
3.6	19.30	8.93	85.31	26.52	116.85	39.77
7.3	19.35	9.88	80.07	28.81	105.37	44.03
14.1	18.39	11.48	72.45	34.32	93.71	52.05
19.3	19.37	12.96	74.11	37.75	86.01	54.51

Table 6.4: **Table of mean and standard deviation of the entire quantum illuminated bird object regions for the bird in a cage images constructed by implementing the peak integration method and the subtraction operation.** The mean and standard deviation are presented for peak integration subtracted images for the range of ratios of the thermal illumination to SPDC illumination for kernel sizes of 1×1, 3×3, and 5×5 pixels.

6.3 Optimisation of the Distinguishability

6.3.1 AND-images optimisation

For the Bird in a Cage as presented in chapter 5 a computational optimisation method was implemented to maximise the distinguishability ratio of the output image to the classically acquired image. The optimisation was run for a set of images constructed by thresholding the analogue data at values of $\mu + n\sigma$ for sigma in range 2 to 10 in steps of 0.5, in addition to the global threshold of 510 analogue counts used to generate the results presented in all preceding sections of this work.

For each of the sets of AND-images constructed using a 1×1 kernel, AND-images constructed using a 3×3 kernel, AND-images with accidentals removed constructed using a 1×1 kernel, and AND-images with accidentals removed constructed using a 3×3 kernel an optimised solution for the distinguishability ratio relative to the classically acquired image obtained by thresholding at 510 analogue counts for each level of thermal to SPDC illumination ratio is found. Analysing these resulting optimised solutions an attempt to find a generalised optimised solution is then presented. An optimisation solution that could be generalised across the range

of thermal illumination to SPDC illumination ratios for which a system operates would allow said solution to be applied to hitherto unseen datasets. This could lead to the implementation of the quantum illumination imaging protocol into real-world systems for which the background light illumination level and losses in the system may not be known or only estimated to an order of magnitude. Optimisation parameters are presented in Appendix A

For reference the distinguishability metric is repeated again below in equation 6.1 in which $\langle O \rangle$ is the average value of the regions of the image that comprise only the bird, $\langle S \rangle$ is the average value of the regions of the image that comprise only the cage, and σ_O the noise on the bird regions.

$$D = \frac{\langle O \rangle}{\langle S \rangle + \sigma_O} \tag{6.1}$$

For the following description the different threshold values are split into three categories: low 0.5σ to 2.5σ, high: 4.5σ to 10σ, and mid 3σ to 4σ and the 510 ADC count threshold that was used in the original work presented in chapters 4 and 5. This organisation is in order to allow easier analysis of the results here. the tables of optimisation values are located in Appendix A.

Figure 6.8 displays the original AND-image constructed using the 1×1 kernel alongside the combination of AND-images that has been optimised for the distinguishability for each level of cage illumination. It can be seen by comparing the distinguishability ratios that there is an advantage in the resulting distinguishability ratio for the optimised combination of the AND-images constructed using frames thresholded at a different number of σ across the range of thermal to SPDC illumination ratios presented here. The largest improvements are achieved in the case of a thermal illumination to SPDC illumination ratio of $\lesssim 1\times$ for which there is a $\sim 12\%$ advantage and for the ratios $14.1\times$ and $19.3\times$ for which the respective advantages are $\geq 68.24\%$ and 88.64%. From table 6.5 it can be seen that for a thermal illumination to SPDC illumination ratio of $\lesssim 1$ a greater proportion the AND-images constructed by performing thresholding at a low number of σ are present to the order of 1%, whereas for a thermal illumination to SPDC illumination ratio of > 1 this proportion is of the order 0.001% or less. This indicates that in the case of thermal illumination to SPDC illumination ratio of $\lesssim 1$ the smoothness of the

Thermal background to SPDC ratio	Low	High	Mid
0.5	4.802880%	60.392912%	34.804209%
0.7	1.388266%	54.574414%	44.037320%
1.1	0.003520%	58.364799%	41.631680%
1.6	0.000031%	58.522291%	41.477678%
2.0	0.002951%	47.842375%	52.154675%
3.6	0.003480%	46.000994%	53.995526%
7.3	0.000438%	57.265195%	42.734367%
14.1	0.000328%	99.995960%	0.003711%
19.3	0.000015%	99.999801%	0.000184%

Table 6.5: **Table of the proportions of different ranges of AND-images used to construct the optimised AND-image of the bird in a cage object for a 1×1 kernel.** The proportion AND-images defined as having been constructed from low, high, and mid-ranges of thresholding that comprise the final optimised AND-images.

bird region, which is represented by σ_O in the distinguishability metric, is the component of the distinguishability that is increased in the optimised combination of AND-images. In the case of the thermal illumination to SPDC illumination ratios $14.1\times$ and $19.3\times$ the AND-images constructed by performing thresholding at a high number of σ are present to the order of $\sim 100\%$ which indicates that the ratio of quantum illuminated bird regions to thermally illuminated cage regions is the component of the distinguishability that is being increased in the combination of AND-images. For thermal illumination to SPDC illumination ratios between $1.1\times$ and $7.3\times$ the improvements in the distinguishability are $< 10\%$ and comprise the AND-images constructed by performing thresholding at a high number of σ and the mid-range values in proportions of $\sim 60\%$ high and $\sim 40\%$ mid to $\sim 40\%$ high and $\sim 60\%$ mid.

Thermal vs SPDC Brightness	Classically acquired Image	Quantum Illumination AND-Image 1x1 Kernel	Optimised Quantum Illumination AND-Image 1x1 Kernel	Distinguishability Ratio		
				$\frac{D_{AND}}{D_{Classical}}$	$\frac{D_{Opt}}{D_{Classical}}$	Percentage Increase
0.5				1.17	1.31	11.64%
0.7				2.06	2.30	11.62%
1.1			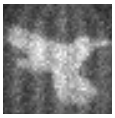	2.35	2.49	6.23%
1.6	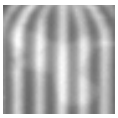	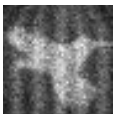	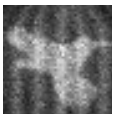	3.44	3.57	3.74%
2.0	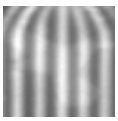	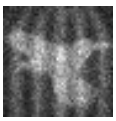	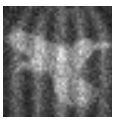	3.82	3.86	0.76%
3.6		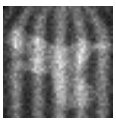	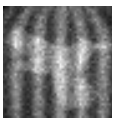	5.02	5.10	1.41%
7.3		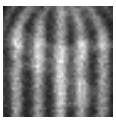	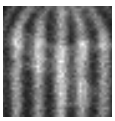	5.28	5.32	0.76%
14.1	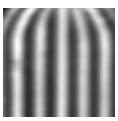	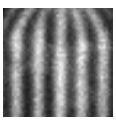		3.39	5.70	68.24%
19.3	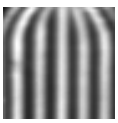	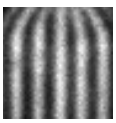	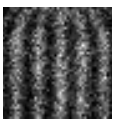	2.31	4.37	88.64%

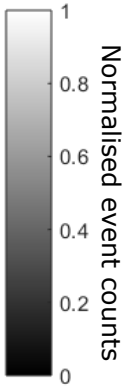

Figure 6.8: **Optimised combination of AND-images of the bird in a cage object constructed using a 1×1 kernel combined to maximise the distinguishability metric.** The classically acquired image (column 1), the quantum illumination AND-image (2nd column) ,and the optimised combination of quantum illumination AND-images (3rd column) alongside the distinguishability ratios. Images constructed over 2.4 million frames.

From the above it can be seen that the solution to the optimisation varies across the range ratios of thermal illumination to SPDC illumination that are presented here ($0.5\times$ to $20\times$). This indicates that for each light level there are different trade-offs between the intensities of the ratio of quantum illuminated bird $\langle O \rangle$ to thermally illuminated cage $\langle S \rangle$, and the smoothness of quantum illuminated target object regions σ_O. The optimisation solution that is to be tested here is for the reduced range of thermal illumination to SPDC illumination ratios from $1.1\times$ to $7.3\times$. An optimisation solution is then sought to maximise the sum of the distinguishabilities of the datasets within this range. This generalised solution is then applied to all datasets as presented in figure 6.9. It can be seen that applying this generalised optimised solution does not result in a significant advantage in the distinguishability across the range of thermal illumination to SPDC illumination ratios presented here and degrades the final image in some cases.

Thermal vs SPDC Brightness	Classically acquired Image	Quantum Illumination AND-Image 1x1 Kernel	Optimised Solution Quantum Illumination AND-Image 1x1 Kernel	Distinguishability Ratio		
				$\frac{D_{AND}}{D_{Classical}}$	$\frac{D_{GenOpt}}{D_{Classical}}$	Percentage Increase
0.5				1.17	1.22	3.55%
0.7				2.06	2.16	4.83%
1.1			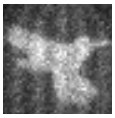	2.35	2.44	3.79%
1.6	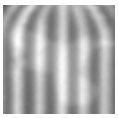	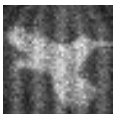	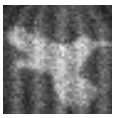	3.44	3.54	2.87%
2.0		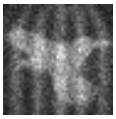	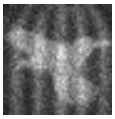	3.82	3.84	0.33%
3.6		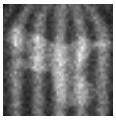	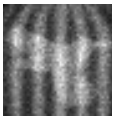	5.02	5.07	0.88%
7.3		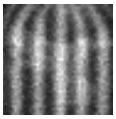	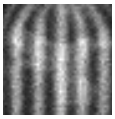	5.28	5.27	-0.21%
14.1		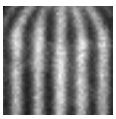	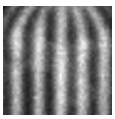	3.39	3.32	-1.80%
19.3		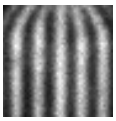	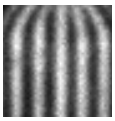	2.31	2.32	0.40%

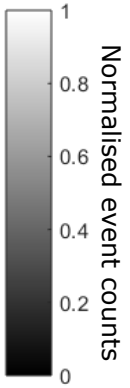

Figure 6.9: **Combination of AND-images of the the bird in a cage object constructed using a 1×1 kernel using optimised solution for Thermal illumination to SPDC illumination ratios of $1.1\times$ to $7.3\times$.** The classically acquired image (column 1), the quantum illumination AND-image (2nd column), and the optimised combination of quantum illumination AND-images (3rd column) alongside the distinguishability ratios. Images constructed over 2.4 million frames.

Figure 6.10 displays the AND-image constructed using the 3×3 kernel alongside the combination of AND-images that has been optimised for the distinguishability for each level of cage illumination. It can be seen by comparing the distinguishability ratios that there is an advantage in the resulting distinguishability ratio for the optimised combination of the AND-images constructed at different levels of thresholding across the range of thermal to SPDC illumination ratios presented here. The largest improvements are achieved in the case of a thermal illumination to SPDC illumination ratio of $> 7\times$ for which there is a 30% to 60% advantage. From table 6.6 it can be seen that for a thermal illumination to SPDC illumination ratio of $< 7\times$ the proportion of AND-images constructed using the 3×3 kernel on frames thresholded at a low number of σ is of the order 0.001% or less. There is no consistency in the proportion of AND-images constructed using the 3×3 kernel on frames thresholded at a high or mid-range number of σ and therefore this range does not appear to present any potential for a generalised optimisation solution. In the case of a thermal illumination to SPDC illumination ratio of $> 7\times$ the proportion of AND-images constructed using the 3×3 kernel on frames thresholded at a low number of σ is of the order 95% or greater. While this initially seems promising, the quality of the images is clearly reduced and this is an artefact of the optimisation process in which the smoothness of the bird region, which is represented by σ_O in the distinguishability metric, is the component of the distinguishability that is increased in the optimised combination of AND-images to the detriment of the relative intensity of the quantum illuminated bird $\langle O \rangle$ to thermally illuminated cage $\langle S \rangle$ regions of the image.

From the above it can be seen that the solution to the optimisation varies across the range ratios of thermal illumination to SPDC illumination that are presented here ($0.5\times$ to $20\times$) which indicates that for each light level there are different trade-offs between the intensities of the ratio of quantum illuminated target object regions $\langle O \rangle$ to thermally illuminated spoof object regions $\langle S \rangle$, and the smoothness of quantum illuminated target object regions σ_O. There are is no clear range that can be used to derive a generalised optimisation solution for this data once the range of thermal illumination to SPDC illumination ratios of $> 7\times$ is discounted.

Thermal vs SPDC Brightness	Classically acquired Image	Quantum Illumination AND-Image 3x3 Kernel	Optimised Quantum Illumination AND-Image 3x3 Kernel	Distinguishability Ratio		
				$\frac{D_{AND}}{D_{Classical}}$	$\frac{D_{Opt}}{D_{Classical}}$	Percentage Increase
0.5				1.50	1.56	4.11%
0.7		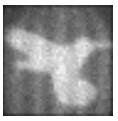		2.22	2.27	2.19%
1.1			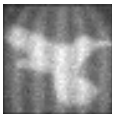	2.58	2.61	1.18%
1.6	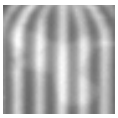	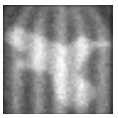	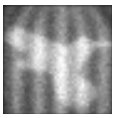	3.26	3.26	0.02%
2.0		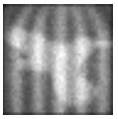	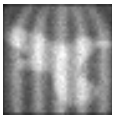	3.44	3.45	0.16%
3.6		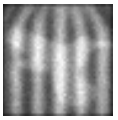		4.28	4.37	2.25%
7.3		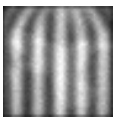		4.28	5.60	30.89%
14.1		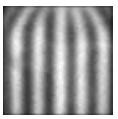		2.78	4.34	56.10%
19.3		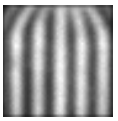		2.03	3.20	57.69%

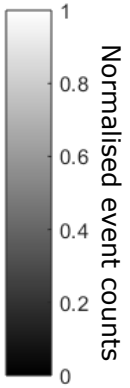

Figure 6.10: **Optimised combination of AND-images of the bird in a cage object constructed using a 3×3 kernel combined to maximise the distinguishability metric.** The classically acquired image (column 1), the quantum illumination AND-image (2nd column), and the optimised combination of quantum illumination AND-images (3rd column) alongside the distinguishability ratios. Images constructed over 2.4 million frames.

Thermal background to SPDC ratio	Low	High	Mid
0.5	0.001414%	55.265521%	44.733065%
0.7	0.000325%	50.298341%	49.701333%
1.1	0.000452%	33.238761%	66.760787%
1.6	0.000132%	8.174498%	91.825370%
2.0	0.000184%	34.239710%	65.760105%
3.6	0.342506%	88.300563%	11.356931%
7.3	95.065821%	4.788887%	0.145292%
14.1	97.940756%	2.020327%	0.038917%
19.3	98.830594%	1.147721%	0.021685%

Table 6.6: **Table of the proportions of different ranges of AND-images used to construct the optimised AND-image of the bird in a cage object for a 3×3 kernel.** The proportion AND-images defined as having been constructed from low, high, and mid-ranges of thresholding that comprise the final optimised AND-images.

6.3.2 AND-images with accidentals subtracted optimisation

Figure 6.11 displays the AND-images with accidentals subtracted constructed using a 1×1 kernel alongside the combination of AND-images with accidentals subtracted that has been optimised for the distinguishability for each level of cage illumination. It can be seen by comparing the distinguishability ratios that there is an advantage in the resulting distinguishability ratio for the optimised combination of the AND-images with accidentals subtracted constructed using a 1×1 kernel constructed using frames thresholded at a different number of σ across the range of thermal to SPDC illumination ratios presented here. There is an advantage of $8\% - 23\%$ across the range of a thermal illumination to SPDC illumination ratios with no noticeable artefacts of the optimisation process as were evident in the case of some of the optimised combinations of AND-images displayed previously. From table 6.7 it can be seen that for the range of thermal illumination to SPDC illumination ratios presented here the optimised AND-images with accidentals subtracted largely comprise the AND-images with accidentals subtracted constructed by performing thresholding at a high number of σ and the mid-range values in proportions of $\sim 60\%$ high and $\sim 35\%$ mid to $\sim 20\%$ high and $\sim 70\%$ mid.

From the above it can be seen that the solution to the optimisation varies across the range ratios of thermal illumination to SPDC illumination that are presented here ($0.5\times$ to $20\times$) which

Thermal vs SPDC Brightness	Classically acquired Image	Quantum Illumination AND-Image with Accidentals Subtracted 1x1 Kernel	Optimised Quantum Illumination AND-Image with Accidentals Subtracted 1x1 Kernel	Distinguishability Ratio		
				$\frac{D_{SUB}}{D_{Classical}}$	$\frac{D_{Opt}}{D_{Classical}}$	Percentage Increase
0.5				1.04	1.13	8.68%
0.7				1.95	2.29	17.49%
1.1				2.45	3.01	23.02%
1.6				4.71	5.49	16.38%
2.0				5.83	6.48	11.30%
3.6				11.28	13.58	20.31%
7.3	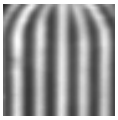			19.43	22.05	13.45%
14.1	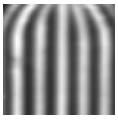			17.96	20.79	15.73%
19.3				16.75	19.57	16.82%

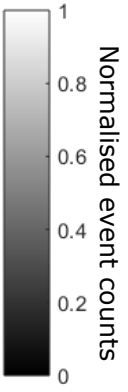

Figure 6.11: **Optimised combination of AND-images with accidentals subtracted the bird in a cage object constructed using a 1×1 kernel combined to maximise the distinguishability metric.** The classically acquired image (column 1), the quantum illumination AND-image with accidentals subtracted (2nd column), and the optimised combination of quantum illumination AND-images with accidentals subtracted (3rd column) alongside the distinguishability ratios. Images constructed over 2.4 million frames.

Thermal background to SPDC ratio	Low	High	Mid
0.5	4.663135%	43.299928%	52.036937%
0.7	5.453934%	48.732097%	45.813969%
1.1	7.690660%	57.18605%	35.123284%
1.6	5.607476%	28.997470%	65.395053%
2.0	2.975999%	41.324580%	55.699422%
3.6	5.383320%	34.940379%	59.676301%
7.3	12.92914%	6.082060%	80.988799%
14.1	6.177962%	43.323070%	50.498968%
19.3	11.341730%	19.938298%	68.719971%

Table 6.7: **Table of the proportions of different ranges of AND-images used to construct the optimised AND-image of the bird in a cage object for a 1×1 kernel.** The proportion AND-images defined as having been constructed from low, high, and mid-ranges of thresholding that comprise the final optimised AND-images.

indicates that for each light level there are different trade-offs between the intensities of the ratio of quantum illuminated bird $\langle O \rangle$ to thermally illuminated cage $\langle S \rangle$, and the smoothness of quantum illuminated target object regions σ_O. However, the final optimised solution and the AND-images with accidentals subtracted largely appear to follow a similar trend and so an optimisation solution is then sought to maximise the sum of the distinguishabilities of the datasets across the range of thermal illumination to SPDC illumination ratios. This generalised solution is then applied to all datasets as presented in figure 6.12. It can be seen that applying this generalised optimised solution results in an advantage in the distinguishability from $\gtrsim 90\%$ of the distinguishability enhancement that can be achieved by optimising for a single set of images for a given thermal illumination level as displayed in table 6.8. Therefore, the optimisation solution appears to be generalisable across the range of thermal illumination to SPDC illumination ratios presented here.

Thermal vs SPDC Brightness	Classically acquired Image	Quantum Illumination AND-Image with Accidentals Subtracted 1x1 Kernel	Optimised Quantum Illumination AND-Image with Accidentals Subtracted 1x1 Kernel	Distinguishability Ratio		
				$\frac{D_{SUB}}{D_{Classical}}$	$\frac{D_{Opt}}{D_{Classical}}$	Percentage Increase
0.5				1.04	1.12	7.73%
0.7				1.95	2.29	17.60%
1.1				2.45	2.96	21.14%
1.6				4.71	5.45	15.65%
2.0				5.83	6.42	10.19%
3.6				11.28	13.48	19.46%
7.3	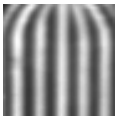		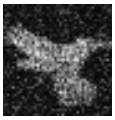	19.43	21.92	12.79%
14.1	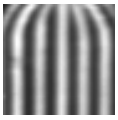			17.96	20.98	16.78%
19.3				16.75	19.42	15.92%

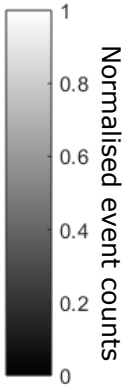

Figure 6.12: **Combination of AND-images with accidentals subtracted for the bird in a cage object constructed using a 1×1 kernel using the optimised solution for the set of AND-images with accidentals subtracted obtained across the entire range of thermal illumination to SPDC illumination ratios of $0.5\times$ to $19.3\times$.** The classically acquired image (column 1), the quantum illumination AND-image with accidentals subtracted (2nd column) and the optimised quantum illumination AND-image with accidentals subtracted (3rd column) alongside the distinguishability ratios. Images constructed over 2.4 million frames.

Thermal background to SPDC ratio	$D_{Opt}/D_{Classical}$	$D_{GenOpt}/D_{Classical}$	$D_{GenOpt}/D_{Opt}(\%)$
0.5	1.13	1.12	92.56%
0.7	2.29	2.29	100.16%
1.1	3.01	2.96	97.72%
1.6	5.49	5.45	99.24%
2.0	6.48	6.42	98.82%
3.6	13.58	13.48	99.24%
7.3	22.05	21.92	99.39%
14.1	20.79	20.98	100.96%
19.3	19.57	19.42	99.19%

Table 6.8: **Table of the distinguishability ratios for the optimised combinations of each set of AND-images with accidentals subtracted of the bird in a cage object constructed using a 1×1 kernel.** The distinguishability ratios for the case in which each AND-image with accidentals subtracted is optimised for distinguishability is presented as $D_{Opt}/D_{Classical}$ in column 2. The distinguishability ratios for the case in which the entire range of AND-images with accidentals subtracted are optimised for the sum of the distinguishabilities is presented as $D_{GenOpt}/D_{Classical}$ in column 3. For comparison the ratio of these two values is presented in column 4.

Figure 6.13 displays the AND-images with accidentals subtracted constructed using a 3×3 kernel alongside the combination of AND-images with accidentals subtracted that has been optimised for the distinguishability for each level of cage illumination. It can be seen by comparing the distinguishability ratios that there is an advantage in the resulting distinguishability ratio for the optimised combination of the AND-images with accidentals subtracted constructed using a 3×3 kernel constructed using frames thresholded at a different number of σ across the range of thermal to SPDC illumination ratios presented here. There is an advantage of $10\% - 27\%$ across the range of a thermal illumination to SPDC illumination ratios with no noticeable artefacts of the optimisation process as were evident in the case of some of the optimised combinations of AND-images displayed previously. From table 6.9 it can be seen that for the range of thermal illumination to SPDC illumination ratios presented here the optimised AND-images with accidentals subtracted largely comprise the AND-images with accidentals subtracted constructed by performing thresholding at a high number of σ and the mid-range values in proportions of $\sim 70\%$ high and $\sim 25\%$ mid to $\sim 45\%$ high and $\sim 50\%$ mid.

From the above it can be seen that the solution to the optimisation varies across the range

Thermal vs SPDC Brightness	Classically acquired Image	Quantum Illumination AND-Image with Accidentals Subtracted 3x3 Kernel	Optimised Quantum Illumination AND-Image with Accidentals Subtracted 3x3 Kernel	Distinguishability Ratio		
				$\frac{D_{SUB}}{D_{Classical}}$	$\frac{D_{Opt}}{D_{Classical}}$	Percentage Increase
0.5				1.47	1.69	14.89%
0.7				2.76	3.18	15.17%
1.1				3.53	4.03	14.43%
1.6				6.93	7.63	10.09%
2.0				8.25	9.24	12.05%
3.6				16.93	19.10	12.84%
7.3				26.94	30.50	13.20%
14.1				24.40	30.43	24.70%
19.3				21.91	27.85	27.07%

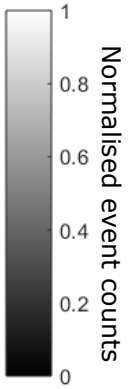

Figure 6.13: **Optimised combination of AND-images with accidentals subtracted constructed using a 3×3 kernel combined to maximise the distinguishability metric.** The classically acquired image (column 1), the quantum illumination AND-image with accidentals subtracted (2nd column), and the optimised combination of quantum illumination AND-images with accidentals subtracted (3rd column) alongside the distinguishability ratios. Images constructed over 2.4 million frames.

Thermal background to SPDC ratio	Low	High	Mid
0.5	0.882592%	37.885111%	61.232298%
0.7	1.417213%	25.991101%	72.591686%
1.1	4.343852%	30.290006%	65.366142%
1.6	4.908081%	51.112776%	43.979143%
2.0	3.656434%	47.799112%	48.544454%
3.6	4.297537%	52.366806%	43.335657%
7.3	8.374916%	32.985247%	58.639837%
14.1	9.120116%	41.068764%	49.811120%
19.3	7.637581%	46.728707%	45.633712%

Table 6.9: **Table of the proportions of different ranges of AND-images used to construct the optimised AND-image for a 3×3 kernel.** The proportion AND-images defined as having been constructed from low, high, and mid-ranges of thresholding that comprise the final optimised AND-images.

of ratios of thermal illumination to SPDC illumination that are presented here ($0.5\times$ to $20\times$) which indicates that for each light level there are different trade-offs between the intensities of the ratio of quantum illuminated bird $\langle O \rangle$ to thermally illuminated cage $\langle S \rangle$, and the smoothness of quantum illuminated target object regions σ_O. However, the final optimised solution and the AND-images with accidentals subtracted largely appear to follow a similar trend and so an optimisation solution is then sought to maximise the sum of the distinguishabilities of the datasets across the range of thermal illumination to SPDC illumination ratios. This generalised solution is then applied to all datasets as presented in figure 6.14. It can be seen that applying this generalised optimised solution results in an advantage in the distinguishability from $\gtrsim 95\%$ of the distinguishability enhancement that can be achieved by optimising for a single thermal illumination level as shown in table 6.10. Therefore the optimisation solution appears to be generalisable across the range of thermal illumination to SPDC illumination ratios presented here.

In table 6.11 the total improvement in the distinguishability that can be achieved by implementing the techniques presented in this chapter is presented for each of the illumination levels used. The average improvement for the range of ratios of thermal illumination to SPDC illumination that are presented here ($0.5\times$ to $20\times$) is 61.54%.

Thermal vs SPDC Brightness	Classically acquired Image	Quantum Illumination AND-Image with Accidentals Subtracted 3x3 Kernel	Optimised Quantum Illumination AND-Image with Accidentals Subtracted 3x3 Kernel	Distinguishability Ratio		
				$\frac{D_{SUB}}{D_{Classical}}$	$\frac{D_{Opt}}{D_{Classical}}$	Percentage Increase
0.5				1.47	1.65	12.08%
0.7				2.76	3.12	12.73%
1.1				3.53	3.98	12.86%
1.6				6.93	7.70	11.11%
2.0				8.25	9.14	10.82%
3.6				16.93	19.11	12.892%
7.3				26.94	30.11	11.75%
14.1				24.40	30.16	23.58%
19.3	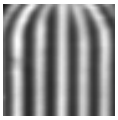			21.91	26.83	22.42%

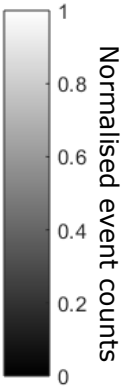

Figure 6.14: **Combination of AND-images with accidentals subtracted constructed using a 3×3 kernel using the optimised solution for the set of AND-images with accidentals subtracted obtained across the entire range of thermal illumination to SPDC illumination ratios of $0.5\times$ to $19.3\times$.** The classically acquired image (column 1), the quantum illumination AND-image with accidentals subtracted (2nd column) and the optimised quantum illumination AND-image with accidentals subtracted (3rd column) alongside the distinguishability ratios. Images constructed over 2.4 million frames.

Thermal background to SPDC ratio	$D_{Opt}/D_{Classical}$	$D_{GenOpt}/D_{Classical}$	$D_{GenOpt}/D_{Opt}(\%)$
0.5	1.69	1.65	94.04%
0.7	3.18	3.12	96.91%
1.1	4.03	3.98	98.18%
1.6	7.63	7.70	101.06%
2.0	9.24	9.14	98.76%
3.6	19.10	19.11	100.08%
7.3	30.50	30.11	98.68%
14.1	30.43	30.16	99.07%
19.3	27.85	26.83	96.21%

Table 6.10: **Table of the distinguishability ratios for the optimised combinations of each set of AND-images with accidentals subtracted constructed using a 3×3 kernel.** The distinguishability ratios for the case in which each AND-image with accidentals subtracted is optimised for distinguishability is presented as $D_{Opt}/D_{Classical}$ in column 2. The distinguishability ratios for the case in which the entire range of AND-images with accidentals subtracted are optimised for the sum of the distinguishabilities is presented as $D_{GenOpt}/D_{Classical}$ in column 3. For comparison the ratio of these two values is presented in column 4.

Thermal background to SPDC ratio	$D_{SUB,1\times1}/D_{Classical}$	$D_{GenOpt,3\times3}/D_{Classical}$	Distinguishability improvement $(\%)$
0.5	1.04	1.65	58.65%
0.7	1.95	3.12	60.00%
1.1	2.45	3.98	62.45%
1.6	4.71	7.70	63.48%
2.0	5.83	9.14	56.78%
3.6	11.28	19.11	69.41%
7.3	19.43	30.11	54.97%
14.1	17.96	30.16	67.93%
19.3	16.75	26.83	60.18%

Table 6.11: **Table of the improvement in the distinguishability ratios using the improved data extraction techniques for the bird in a cage object** The distinguishability ratios for the AND-image with accidentals subtracted constructed using a 1×1 kernel is presented as $D_{SUB,1\times1}/D_{Classical}$ in column 2. The distinguishability ratios for the range of AND-images with accidentals subtracted constructed using a 3×3 kernel and having the generalised optimisation solution applied is presented as $D_{GenOpt,3\times3}/D_{Classical}$ in column 3. The total improvement in the distinguishability that can be achieved by implementing the techniques presented in this chapter is presented in column 4.

Thermal background to SPDC ratio	$D_{SUB,1\times1}/D_{Classical}$	$D_{GenOpt,3\times3}/D_{Classical}$	Distinguishability improvement (%)
1.0	3.13	4.54	45.05%
1.3	3.93	5.98	52.16%
1.8	4.50	6.79	50.89%
2.6	3.66	5.47	49.45%
3.8	3.04	5.59	83.88%

Table 6.12: **Table of the improvement in the distinguishability ratios using the improved data extraction techniques for the fish in a net object** The distinguishability ratios for the AND-image with accidentals subtracted constructed using a 1×1 kernel is presented as $D_{SUB,1\times1}/D_{Classical}$ in column 2. The distinguishability ratios for the range of AND-images with accidentals subtracted constructed using a 3×3 kernel and having the generalised optimisation solution applied is presented as $D_{GenOpt,3\times3}/D_{Classical}$ in column 3. The total improvement in the distinguishability that can be achieved by implementing the techniques presented in this chapter is presented in column 4.

6.3.3 Application of Optimisation Solution to an Unknown Scene

The optimisation solutions that were derived using the bird in a cage data in the preceding section are here tested against a different scene in order to test whether the solution is generalisable. A set of images of a quantum illuminated fish caught within a thermally illuminated net is used. The quantum illuminated fish is illuminated at the same light level as the quantum illuminated bird used up until this point and the illumination levels of the net are within the range of the cage illumination levels. For the AND-images with accidentals subtracted constructed using a 1×1 kernel an average improvement in the distinguishabilities of the dataset of $\sim 15\%$ is achieved as shown in figure 6.15. For the AND-images with accidentals subtracted constructed using a 3×3 kernel an average improvement in the distinguishabilities of the dataset of $\sim$ 3.5% is achieved as shown in figure 6.16. These results show that the distinguishability of an AND-image with accidentals subtracted can be further improved through the application of a generalisable optimisation solution.

In table 6.12 the total improvement in the distinguishability for the fish in a net object that can be achieved by implementing the techniques presented in this chapter is presented for each of the illumination levels used. The average improvement for the range of ratios of thermal illumination to SPDC illumination that are presented here ($1.0\times$ to $3.8\times$) is 56.29%.

Thermal vs SPDC Brightness	Classically acquired Image	Quantum Illumination AND-Image with Accidentals Subtracted 1x1 Kernel	Optimised Quantum Illumination AND-Image with Accidentals Subtracted 1x1 Kernel	Distinguishability Ratio		
				$\frac{D_{SUB}}{D_{Classical}}$	$\frac{D_{Opt}}{D_{Classical}}$	Percentage Increase
0.9				3.13	3.52	12.46%
1.2				3.93	4.73	20.36%
1.6				4.50	4.99	10.89%
2.4				3.66	4.15	13.39%
3.5			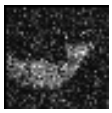	3.04	3.61	18.75%

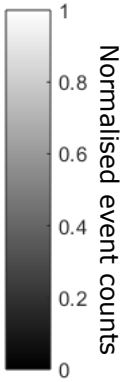

Figure 6.15: **Combination of AND-images with accidentals subtracted constructed using a 1×1 kernel using the optimised solution for the set of AND-images with accidentals subtracted for the fish in a net object obtained across the entire range of thermal illumination to SPDC illumination ratios of $0.5\times$ to $19.3\times$.** The classically acquired image (column 1), the quantum illumination AND-image with accidentals subtracted (2nd column) and the optimised quantum illumination AND-image with accidentals subtracted (3rd column) alongside the distinguishability ratios. Images constructed over 2.4 million frames.

Thermal vs SPDC Brightness	Classically acquired Image	Quantum Illumination AND-Image with Accidentals Subtracted 3x3 Kernel	Optimised Quantum Illumination AND-Image with Accidentals Subtracted 3x3 Kernel	Distinguishability Ratio		
				$\frac{D_{SUB}}{D_{Classical}}$	$\frac{D_{Opt}}{D_{Classical}}$	Percentage Increase
0.9				4.37	4.54	3.89%
1.2				5.87	5.98	1.87%
1.6				6.41	6.79	5.93%
2.4				5.36	5.47	2.05%
3.5	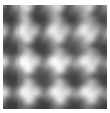			5.38	5.59	3.90%

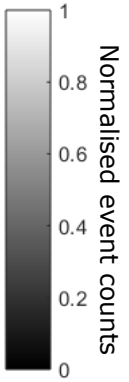

Figure 6.16: **Combination of AND-images with accidentals subtracted constructed using a 3×3 kernel using the optimised solution for the set of AND-images with accidentals subtracted for the fish in a net object obtained across the entire range of thermal illumination to SPDC illumination ratios of $0.5\times$ to $19.3\times$.** The classically acquired image (column 1), the quantum illumination AND-image with accidentals subtracted (2nd column) and the optimised quantum illumination AND-image with accidentals subtracted (3rd column) alongside the distinguishability ratios. Images constructed over 2.4 million frames.

6.4 Discussion

The improved data extraction techniques presented in this chapter enabled greatly improved distinguishability metrics to be obtained. By using the 3×3 kernel to integrate over the extent of the correlation peak the rate at which events are added to the quantum illumination AND-image is increased. An improved data rate can be used to achieve an increased image smoothness or to reduce image acquisition time. The existence of generalised optimisation solutions that use combinations of image data thresholded at different values also shows that there are improvements that can be achieved using the available data and without resorting to black-box methods. By implementing the two improved data extraction techniques presented in this chapter, an average improvement in the distinguishability for the bird in a cage data of 61.54% is obtained. Furthermore, by applying the generalised optimisation solution derived from the bird in a cage data to the fish in a net data an average improvement in the distinguishability of 56.29% is obtained. The increase in the distinguishability metric, or the ability to extract the quantum information in the scene, demonstrates a great improvements and aids progress towards a system that could be implemented in real-world applications.

Chapter 7

Conclusions

At the start of the thesis the following question was asked:
"What is the potential quantum advantage in noise rejection that can be achieved when using a quantum source of illumination over a classical source when imaging under a low-photon flux?"

This thesis presented an imaging scheme that has been applied in a number of different imaging regimes to obtain a quantum advantage in terms of noise rejection. In chapter 1, a summary of background works in the field of quantum imaging was given. In chapter 2, spatial correlations between entangled photon-pairs generated by SPDC are characterised. These spatial correlations are used to realise the quantum advantage in terms of image contrast and noise rejection that are presented here in this thesis.

In chapter 3 the use of this quantum correlated photon source to perform contrast enhanced imaging was demonstrated. A contrast enhancement by a factor of 4.56 ± 0.07 relative to the direct classical imaging scheme was observed. The preferential selection of spatially correlated photon-pairs and preferential rejection of uncorrelated noise was achieved by performing a simple AND-operation on thresholded and binarised camera frames. This operation was performed on the regions of the camera frame that contain the spatially separated reference and the probe beam. This work has applicability in the imaging of photosensitive samples which may be destroyed or damaged should the rate of energy transfer be too great.

In chapter 4 this concept of noise rejection was extended and thermal source was added to

the experimental setup to introduce uncorrelated light into the system and overlay the portion of the camera sensor that detects the probe beam. This work represents the first implementation of a quantum illumination protocol in the context of full-field imaging. An enhancement in background rejection of up to 5.8 and an image contrast improvement of up to a factor of 11 was achieved. Furthermore, it was demonstrated that there is an advantage in the ability to distinguish the scene illuminated using quantum light from the spoof scene illuminated using a thermal light source. The quantum advantage exhibited by the imaging scheme presented in chapter 4 is maintained even in the presence of noise and loss.

In chapter 5 it was shown that the uncorrelated background light present in the spoof scene can be almost completely eliminated through appropriate combination of the quantum illumination AND-image and the classically acquired image. The data required to perform this subtraction operation is all obtained within the same acquisition. In performing this operation $\gtrsim 99\%$ rejection of background light is achieved. An improvement in the distinguishability of the quantum illumination AND-images with accidentals subtracted is up to $\sim 27\times$ that of the corresponding classically acquired image and up to $\sim 11\times$ that of the corresponding quantum illumination AND-image. The rejection of background noise when imaging under a low photon flux has applications in hostile imaging and quantum lidar applications.

In chapter 6 two methods to improve the volume of data that can be extracted from a given set of frames were described. Firstly, to utilise the extent of the correlation peak to compensate for imperfect matching of the strength of the spatial correlations and detector pixel size. Secondly, a generalised optimisation solution of a combination of the quantum illumination AND-images with accidentals subtracted constructed by thresholding the frames at different levels was derived. This optimisation serves to improve the distinguishability metric by $\sim 10\%$ for the data upon which it was derived (bird in a cage) and an improved the distinguishability metric by 3.5% for a new unseen data set (fish in a net). The combination of these two data extraction techniques serves to improve the resulting image distinguishability by $\sim 56\%$ when compared to performing the AND-operation to select the correlated photon-pairs and subtracting the accidental correlations.

The work presented in this thesis contributes towards of quantum enhanced imaging and will

inspire further developments in this field. The experiments demonstrate the potential of quantum enhanced imaging to be applied to imaging under a low photon flux, an imaging regime in which background light and sensor noise rapidly degrade the ability to extract information from an acquired image. Future work in the context of biological imaging would be to implement the system presented in chapter 3 into a quantum microscope for the imaging of photo-sensitive samples. Future work in the context of noise rejection and covert imaging would be to test the system presented in chapters 4 and 5 with regard to the limits on the ratio of thermal illumination to SPDC illumination. Imaging in optically hostile environments has military applications for quantum lidar and covert imaging. Within the context of such applications the ability to observe the real scene and not be deceived by active spoofing, whilst retaining the ability to perform imaging in a covert manner would have a clear benefit in asymmetrical intelligence gathering. The work presented here in this thesis demonstrates some principles that could be applied in the development of such applications. Further work to increase the data rate, either by continuing research into improved data extraction techniques, or through the use of different detectors is required in both cases. This work will contribute towards the development of technologies that are found in real-world applications that present hostile imaging environments. Such future applications include low photon flux biological imaging, covert imaging, quantum lidar, and quantum radar.

Appendix A

Tables of Optimisation Values

Optimisation performed using Matlab to maximise the distinguishability. Opttimisation parameters are as follows: Algorithm - interior-point, MaxFunctionEvaluations - 1000000, DiffMinChange - 0.0001, MaxIterations - 1000000, StepTolerance - 1.0000e-16.

Table A.1: **Table of the optimisation solution for the combination of AND-images constructed using a 1×1 kernel combined to maximise the distinguishability metric for each of the thermal illumination to SPDC illumination ratios of $0.5\times$ to $19.3\times$.** The optimised combination of AND-images constructed using a 1×1 kernel are presented in 6.8.

Illumination Ratio	Threshold									
	1σ	1.5σ	2σ	2.5σ	3σ	3.5σ	4σ	4.5σ	5σ	5.5σ
0.5	8.78E-04	2.15E-03	1.24E-02	3.12E-02	1.13E-01	2.32E-01	4.58E-02	2.42E-02	2.62E-02	1.77E-02
0.7	9.43E-04	2.53E-03	8.81E-03	4.23E-02	2.14E-01	1.34E-01	4.01E-02	5.86E-02	2.71E-02	2.56E-02
1.1	6.18E-04	8.68E-04	9.49E-03	6.59E-02	1.71E-01	1.76E-01	2.40E-03	1.53E-03	4.56E-03	3.87E-03
1.6	5.49E-04	6.78E-05	1.66E-02	3.88E-02	2.32E-01	2.74E-01	9.73E-03	1.83E-03	7.47E-04	1.46E-03
2.0	1.59E-03	1.21E-03	1.48E-02	1.22E-02	2.24E-01	2.26E-01	3.43E-03	2.02E-03	3.21E-02	9.99E-04
3.6	6.79E-05	1.54E-03	1.20E-02	4.03E-02	3.14E-01	2.33E-01	4.77E-02	3.02E-02	9.90E-04	4.85E-04
7.3	5.91E-04	3.14E-03	1.44E-02	1.11E-01	1.99E-01	3.34E-01	1.44E-03	3.15E-03	7.35E-03	2.32E-03
14.1	3.67E-03	1.92E-03	1.62E-02	4.00E-02	1.95E-01	2.27E-01	3.72E-02	3.34E-02	2.96E-02	3.58E-02
19.3	5.19E-03	4.93E-04	4.04E-03	1.04E-01	2.99E-01	1.82E-01	1.81E-01	7.93E-02	5.63E-03	6.02E-03
	Threshold									
	6σ	6.5σ	7σ	7.5σ	8σ	8.5σ	9σ	9.5σ	10σ	510
0.5	2.34E-02	2.06E-02	1.82E-02	3.48E-02	6.45E-02	6.59E-02	5.24E-02	4.36E-02	4.13E-02	1.30E-01
0.7	2.88E-02	3.82E-02	3.67E-02	3.48E-02	3.92E-02	3.92E-02	4.68E-02	5.85E-02	5.39E-02	7.03E-02
1.1	1.10E-02	5.33E-02	4.67E-02	5.64E-03	7.73E-02	2.15E-02	1.33E-02	8.69E-02	2.46E-01	2.24E-03
1.6	3.69E-03	4.07E-03	2.43E-01	9.00E-03	2.71E-03	5.36E-03	5.86E-03	3.98E-03	7.96E-03	1.39E-01
2.0	1.26E-03	1.66E-03	1.83E-03	4.01E-03	4.39E-03	3.44E-01	6.93E-03	3.54E-03	1.03E-02	1.04E-01
3.6	9.06E-04	1.15E-03	3.48E-03	7.15E-03	8.20E-03	2.35E-01	3.77E-03	4.37E-03	5.38E-02	2.55E-03
7.3	1.92E-03	1.27E-03	3.17E-03	1.81E-03	3.39E-03	3.22E-03	7.47E-03	5.80E-03	1.99E-02	2.75E-01
14.1	3.12E-02	3.14E-02	3.14E-02	3.90E-02	4.02E-02	3.79E-02	3.71E-02	4.11E-02	4.51E-02	4.53E-02
19.3	4.65E-03	3.69E-03	3.54E-03	4.54E-03	8.48E-03	9.55E-03	9.21E-03	2.36E-02	4.11E-02	2.52E-02

Table A.2: **Table of the generalised optimisation solution for the combination of AND-images constructed using a 1×1 kernel using the optimised solution for thermal illumination to SPDC illumination ratios of $1.1\times$ to $7.3\times$.** The combination of AND-images constructed using a 1×1 kernel using this generalised optimisation solution for the thermal illumination to SPDC illumination ratios of $1.1\times$ to $7.3\times$ are presented in 6.9.

Threshold									
1σ	1.5σ	2σ	2.5σ	3σ	3.5σ	4σ	4.5σ	5σ	5.5σ
5.96E-07	1.78E-06	7.64E-06	2.94E-05	2.91E-04	4.61E-01	1.17E-01	7.38E-03	2.68E-02	4.81E-03
Threshold									
6σ	6.5σ	7σ	7.5σ	8σ	8.5σ	9σ	9.5σ	10σ	510
1.54E-02	1.00E-02	2.10E-01	5.43E-03	7.09E-03	1.54E-02	1.11E-02	8.20E-03	1.17E-02	8.81E-02

Table A.3: **Table of the optimisation solution for the combination of AND-images constructed using a 3×3 kernel combined to maximise the distinguishability metric for each of the thermal illumination to SPDC illumination ratios of $0.5\times$ to $19.3\times$.** The optimised combination of AND-images constructed using a 3×3 kernel are presented in 6.10.

Illumination Ratio	Threshold									
	1σ	1.5σ	2σ	2.5σ	3σ	3.5σ	4σ	4.5σ	5σ	5.5σ
0.5	1.44E-07	4.13E-07	2.37E-06	1.12E-05	2.79E-02	4.18E-01	4.41E-04	8.63E-04	5.66E-03	2.22E-03
0.7	4.43E-08	1.23E-07	6.19E-07	2.47E-06	5.91E-05	4.58E-01	2.27E-02	3.49E-04	1.05E-03	7.17E-02
1.1	8.44E-08	2.11E-07	8.59E-07	3.37E-06	2.78E-05	3.71E-01	2.95E-01	1.59E-04	3.25E-04	3.26E-01
1.6	4.84E-08	8.82E-08	2.82E-07	8.99E-07	6.78E-06	5.84E-05	1.61E-01	3.46E-04	2.13E-04	4.23E-04
2.0	1.16E-07	1.49E-07	3.88E-07	1.19E-06	8.69E-06	1.66E-01	4.65E-04	3.13E-01	2.24E-03	6.63E-04
3.6	3.28E-03	1.67E-05	3.38E-05	9.38E-05	6.41E-04	1.17E-02	6.12E-02	5.49E-01	2.63E-02	1.76E-02
7.3	9.51E-01	8.59E-06	1.62E-05	3.84E-05	1.37E-04	3.57E-04	5.04E-04	6.74E-04	8.21E-04	1.10E-03
14.1	9.79E-01	4.10E-06	6.97E-06	1.57E-05	4.65E-05	9.54E-05	1.29E-04	1.82E-04	2.46E-04	3.44E-04
19.3	9.88E-01	2.65E-06	4.49E-06	9.74E-06	2.79E-05	5.38E-05	7.06E-05	9.95E-05	1.26E-04	1.75E-04
	Threshold									
	6σ	6.5σ	7σ	7.5σ	8σ	8.5σ	9σ	9.5σ	10σ	510
0.5	1.67E-01	6.01E-03	1.12E-01	6.02E-03	5.60E-03	2.37E-01	3.29E-03	3.15E-03	3.16E-03	5.89E-04
0.7	4.12E-01	1.30E-03	6.46E-04	3.75E-04	6.02E-04	5.88E-03	4.57E-03	2.73E-03	1.36E-03	1.62E-02
1.1	3.82E-04	4.74E-04	5.60E-04	3.70E-04	5.11E-04	1.01E-03	7.12E-04	1.05E-03	9.74E-04	7.83E-04
1.6	7.77E-02	1.70E-04	4.18E-04	2.07E-04	2.63E-04	2.93E-04	4.77E-04	7.98E-04	4.70E-04	7.58E-01
2.0	5.25E-03	3.79E-03	9.80E-03	3.90E-03	3.94E-04	7.92E-04	8.36E-04	5.15E-04	7.84E-04	4.91E-01
3.6	5.69E-02	3.02E-02	4.46E-02	2.13E-02	1.54E-02	3.04E-02	2.95E-02	2.81E-02	3.35E-02	4.01E-02
7.3	1.52E-03	1.87E-03	2.49E-03	2.94E-03	3.60E-03	4.83E-03	6.77E-03	8.98E-03	1.23E-02	4.55E-04
14.1	4.77E-04	6.59E-04	9.52E-04	1.26E-03	1.60E-03	2.40E-03	3.12E-03	3.96E-03	5.01E-03	1.18E-04
19.3	2.37E-04	3.16E-04	4.23E-04	6.23E-04	8.19E-04	1.27E-03	1.76E-03	2.25E-03	3.39E-03	6.46E-05

Table A.4: **Table of the optimisation solution for the combination of AND-images with accidentals subtracted constructed using a 1×1 kernel combined to maximise the distinguishability metric for each of the thermal illumination to SPDC illumination ratios of $0.5\times$ to $19.3\times$..** The combination of AND-images with accidentals subtracted constructed using a 1×1 kernel using this generalised optimisation solution for the thermal illumination to SPDC illumination ratios of $0.5\times$ to $19.3\times$ are presented in 6.12.

Illumination Ratio	Threshold									
	1σ	1.5σ	2σ	2.5σ	3σ	3.5σ	4σ	4.5σ	5σ	5.5σ
0.5	8.78E-04	2.15E-03	1.24E-02	3.12E-02	1.13E-01	2.32E-01	4.58E-02	2.42E-02	2.62E-02	1.77E-02
0.7	9.43E-04	2.53E-03	8.81E-03	4.23E-02	2.14E-01	1.34E-01	4.01E-02	5.86E-02	2.71E-02	2.56E-02
1.1	6.18E-04	8.68E-04	9.49E-03	6.59E-02	1.71E-01	1.76E-01	2.40E-03	1.53E-03	4.56E-03	3.87E-03
1.6	5.49E-04	6.78E-05	1.66E-02	3.88E-02	2.32E-01	2.74E-01	9.73E-03	1.83E-03	7.47E-04	1.46E-03
2.0	1.59E-03	1.21E-03	1.48E-02	1.22E-02	2.24E-01	2.26E-01	3.43E-03	2.02E-03	3.21E-02	9.99E-04
3.6	6.79E-05	1.54E-03	1.20E-02	4.03E-02	3.14E-01	2.33E-01	4.77E-02	3.02E-02	9.90E-04	4.85E-04
7.3	5.91E-04	3.14E-03	1.44E-02	1.11E-01	1.99E-01	3.34E-01	1.44E-03	3.15E-03	7.35E-03	2.32E-03
14.1	3.67E-03	1.92E-03	1.62E-02	4.00E-02	1.95E-01	2.27E-01	3.72E-02	3.34E-02	2.96E-02	3.58E-02
19.3	5.19E-03	4.93E-04	4.04E-03	1.04E-01	2.99E-01	1.82E-01	1.81E-01	7.93E-02	5.63E-03	6.02E-03
	Threshold									
	6σ	6.5σ	7σ	7.5σ	8σ	8.5σ	9σ	9.5σ	10σ	510
0.5	2.34E-02	2.06E-02	1.82E-02	3.48E-02	6.45E-02	6.59E-02	5.24E-02	4.36E-02	4.13E-02	1.30E-01
0.7	2.88E-02	3.82E-02	3.67E-02	3.48E-02	3.92E-02	3.92E-02	4.68E-02	5.85E-02	5.39E-02	7.03E-02
1.1	1.10E-02	5.33E-02	4.67E-02	5.64E-03	7.73E-02	2.15E-02	1.33E-02	8.69E-02	2.46E-01	2.24E-03
1.6	3.69E-03	4.07E-03	2.43E-01	9.00E-03	2.71E-03	5.36E-03	5.86E-03	3.98E-03	7.96E-03	1.39E-01
2.0	1.26E-03	1.66E-03	1.83E-03	4.01E-03	4.39E-03	3.44E-01	6.93E-03	3.54E-03	1.03E-02	1.04E-01
3.6	9.06E-04	1.15E-03	3.48E-03	7.15E-03	8.20E-03	2.35E-01	3.77E-03	4.37E-03	5.38E-02	2.55E-03
7.3	1.92E-03	1.27E-03	3.17E-03	1.81E-03	3.39E-03	3.22E-03	7.47E-03	5.80E-03	1.99E-02	2.75E-01
14.1	3.12E-02	3.14E-02	3.14E-02	3.90E-02	4.02E-02	3.79E-02	3.71E-02	4.11E-02	4.51E-02	4.53E-02
19.3	4.65E-03	3.69E-03	3.54E-03	4.54E-03	8.48E-03	9.55E-03	9.21E-03	2.36E-02	4.11E-02	2.52E-02

Table A.5: **Table of the generalised optimisation solution for the combination of AND-images with accidentals subtracted constructed using a 1×1 kernel using the optimised solution for the set of AND-images with accidentals subtracted obtained across the entire range of thermal illumination to SPDC illumination ratios of $0.5\times$ to $19.3\times$.** The combination of AND-images with accidentals subtracted constructed using a 1×1 kernel using this generalised optimisation solution for the thermal illumination to SPDC illumination ratios of $0.5\times$ to $19.3\times$ are presented in 6.12.

Threshold									
1σ	1.5σ	2σ	2.5σ	3σ	3.5σ	4σ	4.5σ	5σ	5.5σ
1.94E-03	2.73E-04	1.94E-02	7.41E-02	2.90E-01	3.75E-01	5.80E-03	5.75E-02	3.90E-03	2.74E-03
Threshold									
6σ	6.5σ	7σ	7.5σ	8σ	8.5σ	9σ	9.5σ	10σ	510
2.11E-03	1.50E-03	2.41E-03	2.98E-03	4.90E-03	5.23E-03	4.51E-03	9.78E-03	4.21E-02	9.34E-02

Table A.6: **Table of the optimisation solution for the combination of AND-images with accidentals subtracted constructed using a 3×3 kernel combined to maximise the distinguishability metric for each of the thermal illumination to SPDC illumination ratios of $0.5\times$ to $19.3\times$..** The combination of AND-images with accidentals subtracted constructed using a 1×1 kernel using this generalised optimisation solution for the thermal illumination to SPDC illumination ratios of $0.5\times$ to $19.3\times$ are presented in 6.14.

Illumination Ratio	Threshold									
	1σ	1.5σ	2σ	2.5σ	3σ	3.5σ	4σ	4.5σ	5σ	5.5σ
0.5	3.81E-03	8.08E-05	4.41E-03	5.27E-04	2.55E-01	3.19E-01	3.42E-03	2.50E-03	1.87E-01	7.09E-03
0.7	4.06E-03	8.99E-05	6.69E-03	3.33E-03	2.21E-01	4.94E-01	5.76E-03	3.49E-03	7.65E-03	2.38E-02
1.1	3.55E-03	1.77E-03	3.92E-03	3.42E-02	1.56E-01	4.47E-01	2.83E-02	1.00E-02	1.41E-02	5.12E-02
1.6	2.75E-03	2.71E-03	1.13E-02	3.23E-02	1.61E-01	1.06E-01	8.88E-02	4.95E-02	4.45E-02	4.06E-02
2.0	4.13E-03	1.79E-03	3.17E-03	2.75E-02	1.33E-01	2.43E-01	3.83E-02	4.11E-02	3.61E-02	2.60E-02
3.6	3.70E-03	2.56E-03	6.49E-03	3.02E-02	1.87E-01	1.31E-01	6.19E-02	7.84E-02	5.43E-02	4.21E-02
7.3	6.04E-03	4.43E-05	7.48E-04	7.69E-02	1.51E-01	1.60E-01	5.22E-03	8.66E-02	8.71E-04	1.33E-03
14.1	8.01E-03	4.16E-04	1.05E-03	8.17E-02	2.89E-01	7.25E-02	7.28E-03	1.12E-01	1.49E-02	9.46E-02
19.3	5.08E-04	2.02E-05	2.19E-04	7.56E-02	2.74E-01	1.81E-01	8.98E-04	7.01E-04	1.97E-03	1.74E-02
	Threshold									
	6σ	6.5σ	7σ	7.5σ	8σ	8.5σ	9σ	9.5σ	10σ	510
0.5	2.37E-02	2.26E-02	1.10E-02	1.05E-02	6.34E-02	1.47E-02	1.23E-02	1.04E-02	1.38E-02	3.58E-02
0.7	2.22E-02	5.29E-02	2.44E-02	1.57E-02	9.26E-03	1.81E-02	1.98E-02	2.86E-02	3.41E-02	5.28E-03
1.1	1.97E-02	1.98E-02	1.98E-02	2.15E-02	2.50E-02	2.92E-02	2.65E-02	3.05E-02	3.57E-02	2.23E-02
1.6	4.25E-02	3.62E-02	3.86E-02	3.88E-02	4.20E-02	4.30E-02	4.23E-02	4.51E-02	4.80E-02	8.42E-02
2.0	2.53E-02	3.05E-02	4.11E-02	4.01E-02	3.66E-02	4.32E-02	4.57E-02	4.91E-02	6.31E-02	7.06E-02
3.6	4.64E-02	3.56E-02	3.82E-02	3.47E-02	3.53E-02	3.77E-02	3.90E-02	3.94E-02	4.25E-02	5.33E-02
7.3	1.99E-03	3.45E-03	5.85E-02	6.57E-02	8.28E-03	7.35E-02	9.95E-03	1.16E-02	8.14E-03	2.70E-01
14.1	1.39E-02	1.55E-02	1.37E-02	1.07E-02	1.68E-02	3.74E-02	2.73E-02	2.46E-02	2.93E-02	1.29E-01
19.3	1.50E-03	1.00E-03	2.61E-03	5.11E-03	5.08E-03	4.23E-03	4.11E-01	4.60E-03	1.21E-02	1.07E-03

Table A.7: **Table of the generalised optimisation solution for the combination of AND-images with accidentals subtracted constructed using a 3×3 kernel using the optimised solution for the set of AND-images with accidentals subtracted obtained across the entire range of thermal illumination to SPDC illumination ratios of $0.5\times$ to $19.3\times$.** The combination of AND-images with accidentals subtracted constructed using a 3×3 kernel using this generalised optimisation solution for the thermal illumination to SPDC illumination ratios of $0.5\times$ to $19.3\times$ are presented in 6.14.

Threshold									
1σ	1.5σ	2σ	2.5σ	3σ	3.5σ	4σ	4.5σ	5σ	5.5σ
4.01E-03	2.41E-04	2.41E-03	6.04E-02	2.69E-01	2.29E-01	2,40E-02	4.71E-02	1.43E-02	3.77E-02
Threshold									
6σ	6.5σ	7σ	7.5σ	8σ	8.5σ	9σ	9.5σ	10σ	510
2.00E-02	1.53E-02	3.06E-02	2.44E-02	2.55E-02	03.39E-02	3.36E-02	2.85E-02	3.49E-02	6.51E-02

Bibliography

[1] M. Planck. On the law of distribution of energy in the normal spectrum. *Annalen der Physik*, 4(3):553–563, 1901.

[2] A. Einstein. On a heuristic point of view about the creation and conversion of light. *Annalen der Physik*, 17:132, 1905.

[3] J. C. Maxwell. A dynamical theory of the electromagnetic field. *Philosophical Transactions of the Royal Society*, 155:459–512, 1865.

[4] N. Bohr. In *On the Quantum Theory of Line Spectra*, Vienna, 1918. D. Kgl. Danske Vidensk. Selsk. Skrifter, Naturvidensk. og Mathem. Afd. 8. Række, IV.1, 1–3.

[5] L. De Broglie. A tentative theory of light quanta. *Philosophical Magazine Letters*, 47:446–458, 1924.

[6] P. Weinberger. Revisiting Louis de Broglie's famous 1924 paper in the *Philosophical Magazine.* Philosophical Magazine Letters*, 86(7):405–410, 2006.*

[7] W. Heisenberg. The actual content of quantum theoretical kinematics and mechanics. Zeitschrift für Physik*, 43(3-4):172–198, 1927.*

[8] W. Heisenberg. Quantum-theoretical reinterpretation of kinematic and mechanical relations. Zeitschrift für Physik*, 33:879–893, 1925.*

[9] M. Born and P. Jordan. Zur Quantenmechanik. Zeitschrift für Physik*, 34(1):858–888, 1925.*

[10] M. Born, W. Heisenberg, and P. Jordan. Zur Quantenmechanik II. Zeitschrift für Physik*, 35:557–615, 1925.*

[11] P. A. M. Dirac. The fundamental equations of quantum mechanics. Proceedings of the Royal Society A*, 109(752):642–653, 1925.*

[12] E. Schrödinger. An undulatory theory of the mechanics of atoms and molecules. Physical Review*, 28(6):1049–1070, 1926.*

[13] M. Born. Zur Quantenmechanik der Stoßvorgänge. Zeitschrift für Physik*, 37:863–867, 1926.*

[14] M. Born. Quantenmechanik der Stoßvorgänge. Zeitschrift für Physik*, 38:803–827, 1926.*

[15] P. Jordan. Bemerkung über einen zusammenhang zwischen duanes quantentheorie der interferenz und den de broglieschen wellen. Zeitschrift für Physik*, 37:376–382, 1926.*

[16] *P. A. M. Dirac. The physical interpretation of the quantum dynamics.* Proceedings of the Royal Society A, *113(765):621–641, 1927.*

[17] *A. Einstein, B. Podolsky, and N. Rosen. Can Quantum-Mechanical Description of Physical Reality Be Considered Complete?* Physical Review, *47(777):777–780, 1935.*

[18] *N. Bohr. Can quantum-mechanical description of physical reality be considered complete?* Physical Review, *48(8):696, 1935.*

[19] *E. Schrördinger. Discussion of probability relations between separated systems.* Mathematical Proceedings of the Cambridge Philosophical Society, *31:555–563, 1935.*

[20] *E. Schrödinger. Probability relations between separated systems.* Mathematical Proceedings of the Cambridge Philosophical Society, *32:446–452, 1936.*

[21] *D. Howard. Einstein on locality and separability.* Studies in History and Philosophy of Science, *16:171–201, 1985.*

[22] *N. Harrigan and R. Spekkens. Incompleteness, and the epistemic view of quantum states.* Foundations of Physics, *40:125–157, 2010.*

[23] *E. Schrödinger. The Present Status of Quantum Mechanics.* Die Naturwissenschaften, *23(48):807–812; 823–828; 844–849, 1935.*

[24] *J. D. Trimmer. The present situation in quantum mechanics: A translation of Schrödinger's" Cat Paradox" paper.* Proceedings of the American Philosophical Society, *pages 323–338, 1980.*

[25] *R. J. C. Spreeuw. A Classical Analogy of Entanglement.* Foundations of Physics, *28(3):361–374, 1998.*

[26] *E. Karimi and R. W. Boyd. Classical entanglement?* Science, *350(6265):1172–1173, 2015.*

[27] *D. Paneru, E. Cohen, R. Fickler, R. W. Boyd, and E. Karimi. Entanglement: quantum or classical?* Reports on Progress in Physics, *83(6):064001, 2020.*

[28] *E. P. Wigner. The Problem of Measurement.* American Journal of Physics, *31(6):6–15, 1963.*

[29] *D. Bohm. A suggested interpretation of the quantum theory in terms of" hidden" variables. I.* Physical Review, *85(2):166–179, 1952.*

[30] *D. Bohm. A suggested interpretation of the quantum theory in terms of" hidden" variables. II.* Physical Review, *85(2):180–193, 1952.*

[31] *D. W. Belousek. Einstein's 1927 unpublished hidden-variable theory: Its background, context and significance.* Studies in History and Philosophy of Science Part B: Studies in History and Philosophy of Modern Physics, *27(4):437–461, 1996.*

[32] *P. Holland. What's wrong with Einstein's 1927 hidden-variable interpretation of quantum mechanics?* Foundations of Physics, *35:177–196, 2005.*

[33] J. Von Neumann. Mathematische Grundlagen der Quantenmechanik. *Verlag Julius-Springer, Berlin, Germany, 1932.*

[34] D. Bohm and Y. Aharonov. Discussion of experimental proof for the paradox of Einstein, Rosen, and Podolsky. Physical Review*, 108(4):1070, 1957.*

[35] J. S. Bell. On the Einstein-Podolsky-Rosen Paradox. Physics*, 1(3):195–200, 1964.*

[36] J. S. Bell. No local deterministic hidden-variable theory can reproduce all the experimental predictions of quantum mechanics. In D'Espagnat, B., editor, Foundations of Quantum Mechanics, Proceedings of the International School of Physics "EnricoFermi" Course XLIX*, page 171. Academic Press, New York, NY, 1971.*

[37] J. Bell. Quantum mechanical ideas. Science*, 177(4052):880–881, 1972.*

[38] J. F. Clauser and M. A. Horne. Experimental consequences of objective local theories. Physical Review D*, 10(2):526, 1974.*

[39] E. P. Wigner. On Hidden Variables and Quantum Mechanical Probabilities. American Journal of Physics*, 38(8):1005–1009, 1970.*

[40] J. F. Clauser and A. Shimony. Bell's theorem: experimental tests and implications. Reports on Progress in Physics*, 41:1881–1927, 1978.*

[41] K. Banaszek and K. Wódkiewicz. Nonlocality of the Einstein-Podolsky-Rosen state in the Wigner representation. Physical Review A*, 58(6):4345–4347, 1998.*

[42] J. F. Clauser, M. A. Horne, A. Shimony, and R. A. Holt. Proposed experiment to test local hidden-variable theories. Physical Review Letters*, 23(15):880, 1969.*

[43] S. J. Freedman and J. F. Clauser. Experimental test of local hidden-variable theories. Physical Review Letters*, 28(14):938, 1972.*

[44] C. A. Kocher and E. D. Commins. Polarization correlation of photons emitted in an atomic cascade. Physical Review Letters*, 18(15):575, 1967.*

[45] A. Aspect, P. Grangier, and G. Roger. Experimental Tests of Realistic Local Theories via Bell's Theorem. Physical Review Letters*, 47(7):460–463, 1981.*

[46] A. Aspect, P. Grangier, and G. Roger. Experimental Realization of Einstein-Podolsky-Rosen-Bohm Gedankenexperiment: A New Violation of Bell's Inequalities. Physical Review Letters*, 49(2):91–94, 1982.*

[47] A. Aspect, J. Dalibard, and G. Roger. Experimental test of Bell's inequalities using time-varying analyzers. Physical Review Letters*, 49(25):1804, 1982.*

[48] J. D. Franson. Bell inequality for position and time. Physical Review Letters*, 62(19):2205–2208, 1989.*

[49] A. Aspect. In Bell's Theorem: The Naive View of an Experimentalist*, Vienna, 2000. Springer.*

[50] M. Genovese. Research on hidden variable theories: A review of recent progresses. Physics Reports*, 413(6):319–396, 2005.*

[51] *P.-A. Moreau, E. Toninelli, T. Gregory, R. S. Aspden, P. A. Morris, and M. J. Padgett. Imaging Bell-type nonlocal behavior.* Science Advances*, 5(7):eaaw2563, 2019.*

[52] *A. J. Leggett and A. Garg. Quantum mechanics versus macroscopic realism: Is the flux there when nobody looks?* Physical Review Letters*, 54(9):857–860, 1985.*

[53] *L. Hardy. Quantum mechanics, local realistic theories, and Lorentz-invariant realistic theories.* Physical Review Letters*, 68(20):2981, 1992.*

[54] *A. J. Leggett. Nonlocal Hidden-Variable Theories and Quantum Mechanics: An Incompatibility Theorem.* Foundations of Physics*, 54(10):1469–1493, 2003.*

[55] *J. Kofler and a. Brukner. Condition for macroscopic realism beyond the Leggett-Garg inequalities.* Physical Review A*, 87(5):052115, 2013.*

[56] *M. E. Goggin, M. P. Almeida, M. Barbieri, B. P. Lanyon, J. L. O'Brien, A. G. White, and G. J. Pryde. Violation of the Leggett-Garg inequality with weak measurements of photons.* Proceedings of the National Academy of Sciences*, 108(4):1256–1261, 2011.*

[57] *N. S. Williams and A. N. Jordan. Weak Values and the Leggett-Garg Inequality in Solid-State Qubits.* Physical Review Letters*, 100(2):026804, 2008.*

[58] *S. Gröblacher, T. Paterek, R. Kaltenbaek, Ĉ. Brukner, M. Żukowski, M. Aspelmeyer, and A. Zeilinger. An experimental test of non-local realism.* Nature*, 446(7138):871–875, 2007.*

[59] *T. Paterek, A. Fedrizzi, S. Gröblacher, T. Jennewein, M. Żukowski, M. Aspelmeyer, and A. Zeilinger. Experimental Test of Nonlocal Realistic Theories Without the Rotational Symmetry Assumption.* Physical Review Letters*, 99(21):210406, 2007.*

[60] *K. Popper. Popper versus Copenhagen.* nature*, 328:675, 1987.*

[61] *K. R. Popper and W. W. Bartley.* Quantum theory and the schism in physics: from the postscript to the logic of scientific discovery. *Postscript Logic Scientific Discovery. Rowman and Littlefield, Totowa, NJ, 1982.*

[62] *A. Sudbery. Popper's Variant of the EPR Experiment Does Not Test the Copenhagen Interpretation.* Philosophy of Science*, 52(3):470–476, 1985.*

[63] *M. Collett and R. Loudon. Analysis of a proposed crucial test of quantum mechanics.* Nature*, 326:671–672, 1987.*

[64] *Y.-H. Kim and Y. Shih. Experimental realization of Popper's experiment: Violation of the uncertainty principle?* Foundations of Physics*, 29(12):1849–1861, 1999.*

[65] *P.-A. Moreau, P. A. Morris, E. Toninelli, T. Gregory, R. S. Aspden, G. Spalding, R. W. Boyd, and M. J. Padgett. Experimental Limits of Ghost Diffraction: Popper's Thought Experiment.* Scientific Reports*, 8(1):13183, 2018.*

[66] *M. Genovese and M. Gramegna. Quantum Correlations and Quantum Non-Locality: A Review and a Few New Ideas.* Applied Sciences*, 9(24):5406, 2019.*

[67] M. D. Reid and P. D. Drummond. Demonstration of the Einstein-Podolsky-Rosen paradox using nondegenerate parametric amplification. Physical Review Letters*, 60(26):2731–2733, 1988.*

[68] M. D. Reid. Demonstration of the Einstein-Podolsky-Rosen paradox using nondegenerate parametric amplification. Physical Review A*, 40(2):913–923, 1989.*

[69] J. C. Howell, R. S. Bennink, S. J. Bentley, and R. W. Boyd. Realization of the Einstein-Podolsky-Rosen Paradox Using Momentum- and Position-Entangled Photons from Spontaneous Parametric Down Conversion. Phys. Rev. Lett.*, 92(21):210403, 2004.*

[70] D. S. Tasca, S. P. Walborn, P. H. Souto Ribeiro, F. Toscano, and P. Pellat-Finet. Propagation of transverse intensity correlations of a two-photon state. Physical Review A*, 79(3):033801, 2009.*

[71] M. D. Reid, P. D. Drummond, W. P. Bowen, E. G. Cavalcanti, P. K. Lam, H. A. Bachor, U. L. Andersen, and G. Leuchs. Colloquium: The Einstein-Podolsky-Rosen paradox: From concepts to applications. Reviews of Modern Physics*, 81(4):1727–1751, 2009.*

[72] S. P. Walborn, C. H. Monken, S. Pádua, and P. H. Souto Ribeiro. Spatial correlations in parametric down-conversion. Physics Reports*, 495(4–5):87–139, 2010.*

[73] R. Horodecki, P. Horodecki, M. Horodecki, and K. Horodecki. Quantum entanglement. Reviews of Modern Physics*, 81(2):865–942, 2009.*

[74] M. Erhard, M. Krenn, and A. Zeilinger. Advances in High Dimensional Quantum Entanglement. Nature Reviews Physics]*, (2):365–381, 2020.*

[75] P.-A. Moreau, E. Toninelli, T. Gregory, and M. J. Padgett. Imaging with quantum states of light. Nature Reviews Physics*, 2019.*

[76] A. Zeilinger. Quantum entanglement: a fundamental concept finding its applications. Physica Scripta*, 1998(T76):203, 1998.*

[77] A. Zeilinger. Experiment and the foundations of quantum physics. Reviews of Modern Physics*, 71(2):S288, 1999.*

[78] T. Hey. Quantum computing: an introduction. Computing Control Engineering Journal*, 10(3):105–112, 1999.*

[79] P. Kok, W. J. Munro, K. Nemoto, T. C. Ralph, J. P. Dowling, and G. J. Milburn. Linear optical quantum computing with photonic qubits. Rev. Mod. Phys.*, 79:135–174, 2007.*

[80] N. Gisin, G. Ribordy, W. Tittel, and H. Zbinden. Quantum Cryptography. Reviews of Modern Physics*, 74(1), 2002.*

[81] N. Gisin and R. Thew. Quantum communication. Nature Photonics*, 1:165–171, 2007.*

[82] M. Erhard, R. Fickler, M. Krenn, and A. Zeilinger. Twisted photons: new quantum perspectives in high dimensions. Light: Science & Applications*, 7(3):17146–17146, 2018.*

[83] C. Degen, F. Reinhard, and P. Cappellaro. Quantum sensing. Reviews of Modern Physics*, 89(3):035002, 2017.*

[84] *E. Polino, M. Valeri, N. Spagnolo, and F. Sciarrino. Photonic quantum metrology.* AVS Quantum Science*, 2(2):024703, 2020.*

[85] *J. A. Armstrong, N. Bloembergen, J. Ducuing, and P. S. Pershan. Interactions between light waves in a nonlinear dielectric.* Physical Review*, 127(6):1918, 1962.*

[86] *P. A. Franken and J. F. Ward. Optical harmonics and nonlinear phenomena.* Reviews of Modern Physics*, 35(1):23, 1963.*

[87] *J. E. Midwinter. Image Conversion From* 1.6 μ *to the Visible in Lithium Niobate.* Applied Physics Letters*, 12(3):68–70, 1968.*

[88] *Robert W Boyd.* Nonlinear Optics*. Elsevier, Burlington MA, 3rd edition, 2008.*

[89] *P. A. Franken, A. E. Hill, C. W. Peters, and G. Weinreich. Generation of Optical Harmonics.* Physical Review Letters*, 7(4):118–119, 1961.*

[90] *J. A. Giordmaine. Mixing of Light Beams in Crystals.* Physical Review Letters*, 8(1):19–20, 1962.*

[91] *P. D. Maker, R. W. Terhune, M. Nisenoff, and C. M. Savage. Effects of Dispersion and Focusing on the Production of Optical Harmonics.* Physical Review Letters*, 8(1):21–22, 1962.*

[92] *A. Savage and R. C. Miller. Measurements of second harmonic generation of the ruby laser line in piezoelectric crystals.* Appl. Opt.*, 1(5):661–664, 1962.*

[93] *M. Bass, P. A. Franken, A. E. Hill, C. W. Peters, and G. Weinreich. Optical Mixing.* Physical Review Letters*, 8(1):18–18, 1962.*

[94] *R. C. Miller and A. Savage. Harmonic generation and mixing of caw*o_4*:* nd^{3+} *and ruby pulsed laser beams in piezoelectric crystals.* Phys. Rev.*, 128:2175–2179, 1962.*

[95] *C. C. Wang and G. W. Racette. Measurement of Parametric Gain Accompanying Optical Difference Frequency Generation.* Applied Physics Letters*, 6(8):169–171, 1965.*

[96] *G. D. Boyd and A. Ashkin. Theory of parametric oscillator threshold with single-mode optical masers and observation of amplification in linb*o_3*.* Phys. Rev.*, 146:187–198, 1966.*

[97] *R. H. Kingston. Parametric amplification and oscillation at optical frequencies.* Proceedings of the IRE*, 50:472, 1962.*

[98] *N. Kroll. Parametric amplification in spatially extended media and application to the design of tuneable oscillators at optical frequencies.* Proceedings of the IEEE*, 51(1):110–114, 1963.*

[99] *S. A. Akhmanov and R. V. Khokhlov. Concerning one possibility of amplification of light waves.* Soviet Physics JETP*, 16:252, 1963.*

[100] *J. A. Giordmaine and R. C. Miller. Tunable Coherent Parametric Oscillation in LiNb O 3 at Optical Frequencies.* Physical Review Letters*, 14(24):973–976, 1965.*

[101] A. H. Firester. Parametric Image Conversion: Part I. Journal of Applied Physics*, 40(12):4842–4849, 1969.*

[102] A. H. Firester. Holography and Parametric Image Conversion: Part II. Journal of Applied Physics*, 40(12):4849–4853, 1969.*

[103] A. H. Firester. Image Upconversion: Part III. Journal of Applied Physics*, 41(2):703–709, 1970.*

[104] F. Devaux and E. Lantz. Ultrahigh-speed imaging by parametric image amplification. Optics Communications*, 118(1-2):25–27, 1995.*

[105] F. Devaux and E. Lantz. Parametric amplification of a polychromatic image. Journal of the Optical Society of America B*, page 8, 1995.*

[106] F. Devaux and E. Lantz. Transfer function of spatial frequencies in parametric image amplification: experimental analysis and application to picosecond spatial filtering. Optics Communications*, 114(3-4):295–300, 1995.*

[107] E. Lantz and F. Devaux. Parametric amplification of images. Quantum and Semiclassical Optics: Journal of the European Optical Society Part B*, 9(2):279, 1997.*

[108] B. Y. Zel'dovich and D. N. Klyshko. Field Statistics in Parametric Luminesence. JETP Letters*, 9:40, 1969.*

[109] D. C. Burnham and D. L. Weinberg. Observation of Simultaneity in Parametric Production of Optical Photon Pairs. Phys. Rev. Lett.*, 25(2):84–87, 1970.*

[110] W. H. Louisell, A. Yariv, and A. E. Siegman. Quantum fluctuations and noise in parametric processes. I. Physical Review*, 124(6):1646, 1961.*

[111] H. A. Haus, J. Mullen, and W. Martienssen. Quantum noise in linear amplifiers. Physical Review*, 128:2407–2413, 1962.*

[112] J. P. Gordon, W. H. Louisell, and L. R. Walker. Quantum fluctuations and noise in parametric processes. II. Physical Review*, 129(1):481, 1963.*

[113] W. G. Wagner and R. W. Hellwarth. Quantum noise in a parametric amplifier with lossy modes. Physical Review*, 133(4A):A915, 1964.*

[114] B. R. Mollow and R. J. Glauber. Quantum Theory of Parametric Amplification. I. Physical Review*, 160(5):1076–1096, 1967.*

[115] B. R. Mollow and R. J. Glauber. Quantum Theory of Parametric Amplification. II. Physical Review*, 160:1097–1108, 1967.*

[116] K. D. N. Coherent photon decay in a nonlinear medium. Soviet Physics JETP Letters*, 6:23–25, 1967.*

[117] D. N. Klyshko. Scattering of Light in a Medium With Nonlinear Polarizability. JETP*, 28(3):522–526, 1969.*

[118] J. M. Manley and H. E. Rowe. Some General Properties of Nonlinear Elements-Part I. General Energy Relations. Proceedings of the IRE*, 44(7):904–913, 1956.*

[119] H. E. Rowe. Some General Properties of Nonlinear Elements. II. Small Signal Theory. Proceedings of the IRE*, 46(5):850–860, 1958.*

[120] H. Heffner. The Fundamental Noise Limit of Linear Amplifiers. Proceedings of the IRE*, 50(7):1604–1608, 1962.*

[121] J. Schneeloch and J. C. Howell. Introduction to the transverse spatial correlations in spontaneous parametric down-conversion through the biphoton birth zone. Journal of Optics*, 18(5):053501, 2016.*

[122] S. E. Harris, M. K. Oshman, and R. L. Byer. Observation of Tunable Optical Parametric Fluorescence. Physical Review Letters*, 18(18):732–734, 1967.*

[123] D. Magde and H. Mahr. Study in ammonium dihydrogen phosphate of spontaneous parametric interaction tunable from 4400 to 16 000 Å. Physical Review Letters*, 18(21):905, 1967.*

[124] S. A. Akhmanov, R. Fadeev, R. V. Khokhlov, and O. N. Chunaev. Quantum noise in parametric light amplifiers. Soviet Physics JETP Letters*, 6:85, 1967.*

[125] R. L. Byer and S. E. Harris. Power and Bandwidth of Spontaneous Parametric Emission. Phys. Rev.*, 168(3):1064–1068, 1968.*

[126] J. E. Midwinter and J. Warner. The effects of phase matching method and of uniaxial crystal symmetry on the polar distribution of second-order non-linear optical polarization. British Journal of Applied Physics*, 16(8):1135–1142, 1965.*

[127] D. A. Kleinman. Theory of Optical Parametric Noise. Phys. Rev.*, 174(3):1027–1041, 1968.*

[128] F. M. Miatto, D. Giovannini, J. Romero, S. Franke-Arnold, S. M. Barnett, and M. J. Padgett. Bounds and optimisation of orbital angular momentum bandwidths within parametric down-conversion systems. The European Physical Journal D*, 66(7):178, 2012.*

[129] L. Mandel and E. Wolf. Optical Coherence and Quantum Optics*. Cambridge University Press, Cambridge, UK, 1995.*

[130] H. Vanherzeele and C. Chen. Widely tunable parametric generation in beta barium borate. Applied Optics*, 27(13):2634–2636, 1988.*

[131] J. Romero, D. Giovannini, S. Franke-Arnold, S. M. Barnett, and M. J. Padgett. Increasing the dimension in high-dimensional two-photon orbital angular momentum entanglement. Physical Review A*, 86(1):012334, 2012.*

[132] A. Gavrielides, P. Peterson, and D. Cardimona. Diffractive imaging in three-wave interactions. Journal of Applied Physics*, 62(7):2640–2645, 1987.*

[133] P. A. Laferriere, C. J. Wetterer, L. P. Schelonka, and M. A. Kramer. Spatial-frequency selection using downconversion optical parametric amplification. Journal of Applied Physics*, 65(9):3347–3350, 1989.*

[134] G. D. Boyd, R. C. Miller, K. Nassau, W. L. Bond, and A. Savage. $LiNbO_3$: An Efficient Phase Matchable Nonlinear Optical Material. Applied Physics Letters*, 5(11):234–236, 1964.*

[135] R. C. Miller, G. D. Boyd, and A. Savage. Nonlinear Optical Iinteractions in $LiNbO_3$ Without Double Refraction. Applied Physics Letters*, 6(4):77–79, 1965.*

[136] R. C. Miller and A. Savage. Temperature Dependence of the Optical Properties of Ferroelectric $LiNbO_3$ and $LiTaO_3$. Applied Physics Letters*, 9(4):169–171, 1966.*

[137] M. V. Hobden and J. Warner. The Temperature Dependence of the Refractive Indices of Pure Lithium Niobate. Physics Letters*, 22(3):243–244, 1966.*

[138] W. Wiechmann, T. Fukui, H. Masuda, and S. Kubota. Refractive-index temperature derivatives of potassium titanyl phosphate. Optics Letters*, 18(15):1208, 1993.*

[139] S. Emanueli and A. Arie. Temperature-Dependent Dispersion Equations for KTiOPO4 and KTiOAsO4. Applied Optics*, 42(33):6661, 2003.*

[140] T. E. Keller and M. H. Rubin. Theory of two-photon entanglement for spontaneous parametric down-conversion driven by a narrow pump pulse. Physical Review A*, 56(2):1534–1541, 1997.*

[141] N. Boeuf, D. Branning, I. Chaperot, E. Dauler, S. Guérin, G. Jaeger, and A. Muller, A.and Migdall. Calculating characteristics of noncollinear phase matching in uniaxial and biaxial crystals. Optical Engineering*, 39(4):1016, 2000.*

[142] C. K. Law and J. H. Eberly. Analysis and Interpretation of High Transverse Entanglement in Optical Parametric Down Conversion. Physical Review Letters*, 92(12):127903, 2004.*

[143] P. Kolenderski, W. Wasilewski, and K. Banaszek. Modeling and optimization of photon pair sources based on spontaneous parametric down-conversion. Physical Review A*, 80(1):013811, 2009.*

[144] A. N. Vamivakas, B. E. A. Saleh, A. V. Sergienko, and M. C. Teich. Theory of spontaneous parametric down-conversion from photonic crystals. Physical Review A*, 70(4), 2004.*

[145] T. I. Novikova, K. A. Kuznetsov, A. A. Leontyev, and G. K. Kitaeva. Study of SPDC spectra to reveal temperature dependences for optical-terahertz biphotons. Applied Physics Letters*, 116(26):264003, 2020.*

[146] P. G. Kwiat, K. Mattle, H. Weinfurter, A. Zeilinger, A. V. Sergienko, and Y. Shih. New high-intensity source of polarization-entangled photon pairs. Physical Review Letters*, 75(24):4337, 1995.*

[147] S.-Y. Baek and Y.-H. Kim. Spectral properties of entangled photon pairs generated via frequency-degenerate type-I spontaneous parametric down-conversion. Physical Review A*, 77(4):043807, 2008.*

[148] O. Kwon, Y.-W. Cho, and Y.-H. Kim. Single-mode coupling efficiencies of type-II spontaneous parametric down-conversion: Collinear, noncollinear, and beamlike phase matching. Physical Review A*, 78(5):053825, 2008.*

[149] J.-L. Blanchet, F. Devaux, L. Furfaro, and E. Lantz. Measurement of sub-shot-noise correlations of spatial fluctuations in the photon-counting regime. Physical Review Letters*, 101(23):233604, 2008.*

[150] Type II False Colour Image. [Online] http://www.tongue-twister.net/mr/physics/entangled.htm [Accessed 10/02/2017].

[151] M. D. Reid and D. F. Walls. Violations of classical inequalities in quantum optics. Physical Review A*, 34(2):1260–1276, 1986.*

[152] P. G. Kwiat, P. H. Eberhard, A. M. Steinberg, and R. Y. Chiao. Proposal for a loophole-free Bell inequality experiment. Physical Review A*, 49(5):3209–3220, 1994.*

[153] C. H. Monken, P. H. Souto Ribeiro, and S. Pádua. Optimizing the photon pair collection efficiency: A step toward a loophole-free Bell's inequalities experiment. Physical Review A*, 57(4):R2267–R2269, 1998.*

[154] Z. Y. Ou and L. Mandel. Violation of Bell's Inequality and Classical Probability in a Two-Photon Correlation Experiment. Physical Review Letters*, 61(1):50–53, 1988.*

[155] Y. H. Shih and C. O. Alley. New Type of Einstein-Podolsky-Rosen-Bohm Experiment Using Pairs of Light Quanta Produced by Optical Parametric Down Conversion. Physical Review Letters*, 61(26):2921–2924, 1988.*

[156] J. G. Rarity and P. R. Tapster. Experimental violation of Bell's inequality based on phase and momentum. Physical Review Letters*, 64(21):2495–2498, 1990.*

[157] W. Tittel, J. Brendel, H. Zbinden, and N. Gisin. Violation of Bell Inequalities by Photons More Than 10 km Apart. Physical Review Letters*, 81(17):3563–3566, 1998.*

[158] P. G. Kwiat, E. Waks, A. G. White, I. Appelbaum, and P. H. Eberhard. Ultrabright source of polarization-entangled photons. Physical Review A*, 60(2):R773–R776, 1999.*

[159] A. F. Abouraddy, T. Yarnall, B. E. A. Saleh, and M. C. Teich. Violation of Bell's inequality with continuous spatial variables. Physical Review A*, 75(5):052114, 2007.*

[160] J. Leach, B. Jack, J. Romero, M. Ritsch-Marte, R. W. Boyd, A. K. Jha, S. M. Barnett, S. Franke-Arnold, and M. J. Padgett. Violation of a Bell inequality in two-dimensional orbital angular momentum state-spaces. Optics Express*, 17(10):8287–8293, 2009.*

[161] B. Jack, J. Leach, J. Romero, S. Franke-Arnold, M. Ritsch-Marte, S. M. Barnett, and M. J. Padgett. Holographic Ghost Imaging and the Violation of a Bell Inequality. Physical Review Letters*, 103(8), 2009.*

[162] A. C. Dada, J. Leach, G. S. Buller, M. J. Padgett, and E. Andersson. Experimental high-dimensional two-photon entanglement and violations of generalized Bell inequalities. Nature Physics*, 7(9):677–680, 2011.*

[163] M. McLaren, M. Agnew, J. Leach, F. S. Roux, M. J. Padgett, R. W. Boyd, and A. Forbes. Entangled Bessel-Gaussian beams. Optics Express*, 20(21):23589–23597, 2012.*

[164] L. K. Shalm, E. Meyer-Scott, B. G. Christensen, P. Bierhorst, M. A. Wayne, M. J. Stevens, T. Gerrits, S. Glancy, D. R. Hamel, M. S. Allman, K. J. Coakley, S. D. Dyer, C. Hodge, A. E. Lita, V. B. Verma, C. Lambrocco, E. Tortorici, A. L. Migdall, Y. Zhang, D. R. Kumor, W. H. Farr, F. Marsili, M. D. Shaw, J. A. Stern, C. Abellán, W. Amaya, V. Pruneri, T. Jennewein, M. W. Mitchell, P. G. Kwiat, J. C. Bienfang, R. P. Mirin, E. Knill, and S. W. Nam. Strong Loophole-Free Test of Local Realism. Physical Review Letters*, 115(25), 2015.*

[165] M. Giustina, M. Versteegh, S. Wengerowsky, J. Handsteiner, A. Hochrainer, K. Phelan, F. Steinlechner, J. Kofler, J. Larsson, C. Abellán, W. Amaya, V. Pruneri, M. Mitchell, J. Beyer, T. Gerrits, A. Lita, L. Shalm, S. Nam, T. Scheidl, R. Ursin, B. Wittmann, and A. Zeilinger. Significant-Loophole-Free Test of Bell's Theorem with Entangled Photons. Physical Review Letters*, 115(25), 2015.*

[166] B. Hensen, H. Bernien, A. E. Dréau, A. Reiserer, N. Kalb, M. S. Blok, J. Ruitenberg, R. F. L. Vermeulen, R. N. Schouten, C. Abellán, W. Amaya, V. Pruneri, M. W. Mitchell, M. Markham, D. J. Twitchen, D. Elkouss, S. Wehner, T. H. Taminiau, and R. Hanson. Loophole-free Bell inequality violation using electron spins separated by 1.3 kilometres. Nature*, 526(7575):682–686, 2015.*

[167] X. Guo, Y. Mei, and S. Du. Testing the Bell inequality on frequency-bin entangled photon pairs using time-resolved detection. Optica*, 4(4):388, 2017.*

[168] The BIG Bell Test Collaboration. Challenging local realism with human choices. Nature*, 557(7704):212–216, 2018.*

[169] C. K. Hong and L. Mandel. Theory of parametric frequency down conversion of light. Physical Review A*, 31(4):2409, 1985.*

[170] S. Friberg, C. K. Hong, and L. Mandel. Measurement of Time Delays in the Parametric Production of Photon Pairs. Physical Review Letters*, 54(18):2011–2013, 1985.*

[171] C. K. Hong, Z. Y. Ou, and L. Mandel. Measurement of subpicosecond time intervals between two photons by interference. Physical Review Letters*, 59(18):2044–2046, 1987.*

[172] S. Friberg, C. Hong, and L. Mandel. Intensity dependence of the normalized intensity correlation function in parametric down-conversion. Optics Communications*, 54(5):311–316, 1985.*

[173] X. Y. Zou, T. P. Grayson, and L. Mandel. Observation of quantum interference effects in the frequency domain. Physical Review Letters*, 69(21):3041, 1992.*

[174] A. A. Malygin, A. N. Penin, and A. V. Sergienko. Spatiotemporal grouping of photons in spontaneous parametric scattering of light. Soviet Physics-Doklady*, 30:227–229, 1985.*

[175] I. Marzoli, A. Gatti, and L. A. Lugiato. Spatial quantum signatures in parametric down-conversion. Physical Review Letters*, 78(11):2092, 1997.*

[176] B. M. Jost, A. V. Sergienko, A. F. Abouraddy, B. E. Saleh, and M. C. Teich. Spatial correlations of spontaneously down-converted photon pairs detected with a single-photon-sensitive CCD camera. Optics Express*, 3(2):81–88, 1998.*

[177] *F. Devaux and E. Lantz. Spatial and temporal properties of parametric fluorescence around degeneracy in a type I LBO crystal.* The European Physical Journal D*, 8(1):117, 2000.*

[178] *A. G. Basden, C. A. Haniff, and C. D. Mackay. Photon Counting Strategies with Low-Light-Level CCDs.* Monthly Notices of the Royal Astronomical Society*, 345(3):985–991, 2003.*

[179] *P.-A. Moreau, F. Devaux, and E. Lantz. Einstein-Podolsky-Rosen Paradox in Twin Images.* Physical Review Letters*, 113(16):160401, 2014.*

[180] *M. Edgar, D. Tasca, F. Izdebski, R. Warburton, J. Leach, M. Agnew, G. Buller, R. Boyd, and M. Padgett. Imaging high-dimensional spatial entanglement with a camera.* Nature Communications*, 3:984, 2012.*

[181] *L. Allen, M. W. Beijersbergen, R. J. C. Spreeuw, and J. P. Woerdman. Orbital angular momentum of light and the transformation of Laguerre-Gaussian laser modes.* Physical Review A*, 45(11):8185, 1992.*

[182] *K. Dholakia, N. B. Simpson, M. J. Padgett, and L. Allen. Second-harmonic generation and the orbital angular momentum of light.* Physical Review A*, 54(5):R3742–R3745, 1996.*

[183] *J. Courtial, K. Dholakia, L. Allen, and M. J. Padgett. Second-harmonic generation and the conservation of orbital angular momentum with high-order Laguerre-Gaussian modes.* Physical Review A*, 56(5):4193–4196, 1997.*

[184] *H. H. Arnaut and G. A. Barbosa. Orbital and Intrinsic Angular Momentum of Single Photons and Entangled Pairs of Photons Generated by Parametric Down-Conversion.* Physical Review Letters*, 85(2):286–289, 2000.*

[185] *A. Mair, A. Vaziri, G. Weihs, and A. Zeilinger. Entanglement of Orbital Angular Momentum States of Photons.* Nature*, 412(6844):313–316, 2001.*

[186] *S. P. Walborn, A. N. de Oliveira, R. S. Thebaldi, and C. H. Monken. Entanglement and conservation of orbital angular momentum in spontaneous parametric down-conversion.* Physical Review A*, 69(2), 2004.*

[187] *J. Leach, R. E. Warburton, D. G. Ireland, F. Izdebski, S. M. Barnett, A. M. Yao, G. S. Buller, and M. J. Padgett. Quantum correlations in position, momentum, and intermediate bases for a full optical field of view.* Physical Review A*, 85(1), 2012.*

[188] *M. Genovese. Real applications of quantum imaging.* Journal of Optics*, 18(7):073002, 2016.*

[189] *L. A. Lugiato, A. Gatti, and E. Brambilla. Quantum imaging.* Journal of Optics B: Quantum and Semiclassical Optics*, 4(3):S176, 2002.*

[190] *A. Meda, E. Losero, N. Samantaray, F. Scafirimuto, S. Pradyumna, A. Avella, I. Ruo-Berchera, and M. Genovese. Photon-number correlation for quantum enhanced imaging and sensing.* Journal of Optics*, 19(9):094002, 2017.*

[191] T. B. Pittman, Y. H. Shih, D. V. Strekalov, and A. V. Sergienko. Optical imaging by means of two-photon quantum entanglement. Physical Review A, 52(5):R3429–R3432, 1995.

[192] D. V. Strekalov, A. V. Sergienko, D. N. Klyshko, and Y. H. Shih. Observation of Two-Photon "Ghost" Interference and Diffraction. Physical Review Letters, 74(18):3600–3603, 1995.

[193] T. B. Pittman, D. V. Strekalov, D. N. Klyshko, M. H. Rubin, A. V. Sergienko, and Y. H. Shih. Two-photon geometric optics. Physical Review A, 53(4):2804–2815, 1996.

[194] P.-A. Moreau, E. Toninelli, T. Gregory, and M. J. Padgett. Ghost Imaging Using Optical Correlations. Laser & Photonics Reviews, page 1700143, 2017.

[195] D. N. Klyshko. A simple method of preparing pure states of an optical field, of implementing the Einstein–Podolsky–Rosen experiment, and of demonstrating the complementarity principle. Soviet Physics Uspekhi, 31(1):74–85, 1988.

[196] R. S. Aspden, D. S. Tasca, R. W. Boyd, and M. J. Padgett. EPR-based ghost imaging using a single-photon-sensitive camera. New Journal of Physics, 15(7):073032, 2013.

[197] P. A. Morris, R. S. Aspden, J. E. C. Bell, R. W. Boyd, and M. J. Padgett. Imaging with a small number of photons. Nature Communications, 6:5913, 2015.

[198] R. S. Aspden, N. R. Gemmell, P. A. Morris, D. S. Tasca, L. Mertens, M. G. Tanner, R. A. Kirkwood, A. Ruggeri, A. Tosi, R. W. Boyd, G. S. Buller, R. H. Hadfield, and M. J. Padgett. Photon-sparse microscopy: visible light imaging using infrared illumination. Optica, 2(12):1049–1052, 2015.

[199] P.-A. Moreau, E. Toninelli, P. A. Morris, R. S. Aspden, T. Gregory, G. Spalding, R. W. Boyd, and M. J. Padgett. Resolution limits of quantum ghost imaging. Optics Express, 26(6):7528, 2018.

[200] R. S. Bennink, S. J. Bentley, and R. W. Boyd. "Two-photon" coincidence imaging with a classical source. Physical Review Letters, 89(11):113601, 2002.

[201] A. F. Abouraddy, B. E. A. Saleh, A. V. Sergienko, and M. C. Teich. Role of Entanglement in Two-Photon Imaging. Physical Review Letters, 87(12):123602, 2001.

[202] A. Gatti, E. Brambilla, M. Bache, and L. A. Lugiato. Ghost imaging with thermal light: comparing entanglement and classicalcorrelation. Physical Review Letters, 93(9):093602, 2004.

[203] Y. J. Cai and S. Y. Zhu. Ghost imaging with incoherent and partially coherent light radiation. Physical Review E, 71(5):056607, 2005.

[204] A. Valencia, G. Scarcelli, M. D'Angelo, and Y. Shih. Two-Photon Imaging with Thermal Light. Physical Review Letters, 94(6):063601, 2005.

[205] F. Ferri, D. Magatti, A. Gatti, M. Bache, E. Brambilla, and L. A. Lugiato. High-Resolution Ghost Image and Ghost Diffraction Experiments with Thermal Light. Physical Review Letters, 94(18):183602, 2005.

[206] G. Scarcelli, V. Berardi, and Y. Shih. Can Two-Photon Correlation of Chaotic Light Be Considered as Correlation of Intensity Fluctuations? Physical Review Letters*, 96(6):063602, 2006.*

[207] B. I. Erkmen and J. H. Shapiro. Unified theory of ghost imaging with Gaussian-state light. Physical Review A*, 77(4):043809, 2008. WOS:000255457100165.*

[208] J. H. Shapiro. Computational ghost imaging. Physical Review A*, 78(6):061802, 2008.*

[209] Y. Bromberg, O. Katz, and Y. Silberberg. Ghost imaging with a single detector. Physical Review A*, 79(5):053840, 2009.*

[210] B. I. Erkmen and J. H. Shapiro. Ghost imaging: from quantum to classical to computational. Advances in Optics and Photonics*, 2(4):405–450, 2010.*

[211] J. H. Shapiro and R. W. Boyd. The physics of ghost imaging. Quantum Information Processing*, 11(4):949–993, 2012.*

[212] A. Gatti, E. Brambilla, M. Bache, and L. A. Lugiato. Correlated imaging, quantum and classical. Physical Review A*, 70(1):013802, 2004.*

[213] R. S. Bennink, S. J. Bentley, R. W. Boyd, and J. C. Howell. Quantum and Classical Coincidence Imaging. Physical Review Letters*, 92(3):033601, 2004.*

[214] G. Brida, M. V. Chekhova, G. A. Fornaro, M. Genovese, L. Lopaeva, and I. R. Berchera. Systematic analysis of SNR in bipartite Ghost Imaging with classical and quantum light. Physical Review A*, 83(6):063807, 2011.*

[215] C. C. Kim and G. Kanner. Infrared two-color ghost imaging using entangled beams. In R. E. Meyers, Y. Shih, and K. S. Deacon, editors, Proceedings Volume 7815, Quantum Communications and Quantum Imaging VIII; 781503 (2010)*, page 781503, 2010.*

[216] S. Karmakar and Y. Shih. Two-color ghost imaging with enhanced angular resolving power. Physical Review A*, 81(3):033845, 2010.*

[217] V. V. Kornienko, S. A. Savinov, Y. A. Mityagin, and G. K. Kitaeva. Terahertz continuous wave nonlinear-optical detection without phase-locking between a source and the detector. Optics Letters*, 41(17):4075–4078, 2016.*

[218] M. Kutas, B. Haase, P. Bickert, F. Riexinger, D. Molter, and G. von Freymann. Terahertz quantum sensing. Science Advances*, 6(11):eaaz8065, 2020.*

[219] J. Cheng and S. Han. Incoherent Coincidence Imaging and Its Applicability in X-ray Diffraction. Physical Review Letters*, 92(9):093903, 2004.*

[220] D. Pelliccia, A. Rack, M. Scheel, V. Cantelli, and D. M. Paganin. Experimental x-ray ghost imaging. Physical Review Letters*, 117(11):113902, 2016.*

[221] H. Yu, R. Lu, S. Han, H. Xie, G. Du, T. Xiao, and D. Zhu. Fourier-transform ghost imaging with hard X rays. Physical Review Letters*, 117(11):113901, 2016.*

[222] R. Meyers, K. S. Deacon, and Y. Shih. Ghost-imaging experiment by measuring reflected photons. Physical Review A*, 77(4):041801, 2008.*

[223] R. E. Meyers, K. S. Deacon, and Y. Shih. Turbulence-free ghost imaging. Applied Physics Letters, 98(11):111115, 2011.

[224] Y. Zhang, A. Sit, F. Bouchard, H. Larocque, F. Grenapin, E. Cohen, A. C. Elitzur, J. L. Harden, R. W. Boyd, and E. Karimi. Interaction-free ghost-imaging of structured objects. Optics Express, 27(3):2212, 2019.

[225] Y. Zhang, L. Gao, A. Sit, G. Amit, H. Larocque, F. Grenapin, J. L. Harden, R. W. Boyd, A. C. Elitzur, E. Cohen, and E. Karimi. Interaction-free quantum imaging. In D. Fixler, S. Wachsmann-Hogiu, and E. M. Goldys, editors, Nanoscale Imaging, Sensing, and Actuation for Biomedical Applications XVII, page 4, San Francisco, United States, 2020. SPIE.

[226] A. C. Elitzur and L. Vaidman. Quantum mechanical interaction-free measurements. Foundations of Physics, 23(7):987–997, 1993.

[227] Vaidman, L. On the Realization of Interaction-Free Measurements. Quantum Opt., 6:119–126, 1994.

[228] P. Kwiat, H. Weinfurter, T. Herzog, A. Zeilinger, and M. Kasevich. Experimental Realization of Interaction-free Measurements. Annals of the New York Academy of Sciences, 755(1):383–393, 1995.

[229] Kwiat P, Weinfurter H, Herzog T, Zeilinger A, and Kasevich M. A. Interaction-Free Measurement. Physical Review Letters, 74(24):4763–4766, 1995.

[230] H. Paul and M. Pavičić. Nonclassical interaction-free detection of objects in a monolithic total-internal-reflection resonator. JOSA B, 14(6):1275–1279, 1997.

[231] T. Tsegaye, E. Goobar, A. Karlsson, G. Björk, M. Y. Loh, and K. H. Lim. Efficient interaction-free measurements in a high-finesse interferometer. Physical Review A, 57(5):3987, 1998.

[232] A. G. White, J. R. Mitchell, O. Nairz, and P. G. Kwiat. "Interaction-free" imaging. Physical Review A, 58(1):605, 1998.

[233] P. G. Kwiat, A. G. White, J. R. Mitchell, O. Nairz, G. Weihs, H. Weinfurter, and A. Zeilinger. High-efficiency quantum interrogation measurements via the quantum Zeno effect. Physical Review Letters, 83(23):4725, 1999.

[234] J.-S. Jang. Optical interaction-free measurement of semitransparent objects. Physical Review A, 59(3):2322, 1999.

[235] G. B. Lemos, V. Borish, G. D. Cole, S. Ramelow, R. Lapkiewicz, and A. Zeilinger. Quantum imaging with undetected photons. Nature, 512(7515):409–412, 2014.

[236] M. Lahiri, R. Lapkiewicz, G. B. Lemos, and A. Zeilinger. Theory of quantum imaging with undetected photons. Physical Review A, 92(1), 2015.

[237] A. Zeilinger, S. Ramelow, R. Lapkiewicz, V. Borish, and G. B. Lemos. Quantum imaging with undetected photons, U.S. Patent 9,557.262 B2, Aug. 2014.

[238] X. Y. Zou, L. J. Wang, and L. Mandel. Induced coherence and indistinguishability in optical interference. Physical Review Letters*, 67(3):318, 1991.*

[239] L. J. Wang, X. Y. Zou, and L. Mandel. Induced coherence without induced emission. Physical Review A*, 44(7):4614, 1991.*

[240] M. I. Kolobov, E. Giese, S. Lemieux, R. Fickler, and R. W. Boyd. Controlling induced coherence for quantum imaging. Journal of Optics*, 19(5):054003, 2017.*

[241] M. Lahiri, A. Hochrainer, R. Lapkiewicz, G. B. Lemos, and A. Zeilinger. Nonclassicality of induced coherence without induced emission. Physical Review A*, 100(5):053839, 2019.*

[242] H. Wiseman and K. Mølmer. Induced coherence with and without induced emission. Physics Letters A*, 270(5):245–248, 2000.*

[243] A. Hochrainer, M. Lahiri, R. Lapkiewicz, G. B. Lemos, and A. Zeilinger. Quantifying the momentum correlation between two light beams by detecting one. Proceedings of the National Academy of Sciences*, 114(7):1508–1511, 2017.*

[244] M. Lahiri, A. Hochrainer, R. Lapkiewicz, G. B. Lemos, and A. Zeilinger. Twin-photon correlations in single-photon interference. Physical Review A*, 96(1), 2017.*

[245] Z. Y. Ou, L. J. Wang, X.-B. Zou, and L. Mandel. Coherence in two-photon down-conversion induced by a laser. Physical Review A*, 41(3):1597–1601, 1990.*

[246] P. H. S. Ribeiro, S. Pádua, and C. H. Monken. Image and coherence transfer in the stimulated down-conversion process. Physical Review A*, 60(6):5074–5078, 1999.*

[247] J. H. Shapiro, D. Venkatraman, and F. N. C. Wong. Classical Imaging with Undetected Photons. Scientific Reports*, 5:10329, 2015.*

[248] A. C. Cardoso, L. P. Berruezo, D. F. Ávila, G. B. Lemos, W. M. Pimenta, C. H. Monken, P. L. Saldanha, and S. Pádua. Classical imaging with undetected light. Physical Review A*, 97(3):033827, 2018.*

[249] M. A. Taylor, J. Janousek, V. Daria, J. Knittel, B. Hage, H.-A. Bachor, and W. P. Bowen. Biological measurement beyond the quantum limit. Nature Photonics*, 7(3):229–233, 2013.*

[250] M. A. Taylor and W. P. Bowen. Quantum metrology and its application in biology. Physics Reports*, 615:1–59, 2016.*

[251] E. Jakeman and J. Walker. Analysis of a method for the generation of light with sub-poissonian photon statistics. Optics Communications*, 55(3):219–222, 1985.*

[252] E. Jakeman and J. H. Jefferson. Antibunching and Sub-poissonian Statistics in Photoelectron-triggered Optical Dead-time Experiments. Optica Acta: International Journal of Optics*, 33(5):557–576, 1986.*

[253] E. Jakeman and J. Rarity. The use of pair production processes to reduce quantum noise in transmission measurements. Optics Communications*, 59(3):219–223, 1986.*

[254] A. Heidmann, R. J. Horowicz, S. Reynaud, E. Giacobino, C. Fabre, and G. Camy. Observation of quantum noise reduction on twin laser beams. Physical Review Letters, 59(22):2555, 1987.

[255] J. Rarity, P. Tapster, and E. Jakeman. Observation of sub-poissonian light in parametric downconversion. Optics Communications, 62(3):201–206, 1987.

[256] P. R. Tapster, S. F. Seward, and J. G. Rarity. Sub-shot-noise measurement of modulated absorption using parametric down-conversion. Physical Review A, 44(5):3266–3269, 1991.

[257] E. Brambilla, L. Caspani, O. Jedrkiewicz, L. Lugiato, and A. Gatti. High-sensitivity imaging with multi-mode twin beams. Physical Review A, 77(5):053807, 2008.

[258] G. Brida, M. Genovese, and I. R. Berchera. Experimental realization of sub-shot-noise quantum imaging. Nature Photonics, 4(4):227–230, 2010.

[259] G. Brida, M. Genovese, A. Meda, and I. R. Berchera. Experimental quantum imaging exploiting multimode spatial correlation of twin beams. Physical Review A, 83(3):033811, 2011.

[260] M. B. Nasr, B. E. A. Saleh, A. V. Sergienko, and M. C. Teich. Demonstration of Dispersion-Canceled Quantum-Optical Coherence Tomography. Physical Review Letters, 91(8):4, 2003.

[261] N. Samantaray, I. Ruo-Berchera, A. Meda, and M. Genovese. Realization of the first sub-shot-noise wide field microscope. Light: Science & Applications, 6(7):e17005–e17005, 2017.

[262] P.-A. Moreau, J. Sabines-Chesterking, R. Whittaker, S. K. Joshi, P. M. Birchall, A. McMillan, J. G. Rarity, and J. C. F. Matthews. Demonstrating an absolute quantum advantage in direct absorption measurement. Scientific Reports, 7(1), 2017.

[263] E. Losero, I. Ruo-Berchera, A. Meda, A. Avella, and M. Genovese. Unbiased estimation of an optical loss at the ultimate quantum limit with twin-beams. Scientific Reports, 8(1):7431, 2018.

[264] V. Giovannetti, S. Lloyd, and L. Maccone. Advances in quantum metrology. Nature Photonics, 5(4):222–229, 2011.

[265] S. Lloyd. Enhanced sensitivity of photodetection via quantum illumination. Science, 321(5895):1463–1465, 2008.

[266] S.-H. Tan, B. I. Erkmen, V. Giovannetti, S. Guha, S. Lloyd, L. Maccone, S. Pirandola, and J. H. Shapiro. Quantum Illumination with Gaussian States. Physical Review Letters, 101(25), 2008.

[267] J. H. Shapiro and S. Lloyd. Quantum illumination versus coherent-state target detection. New Journal of Physics, 11(6):063045, 2009.

[268] L. Mandel. Proposal for almost noise-free optical communication under conditions of high background. Journal of the Optical Society of America B, 1(1):108–110, 1984.

[269] S. Guha and B. I. Erkmen. Gaussian-state quantum-illumination receivers for target detection. Physical Review A*, 80(5), 2009.*

[270] M. F. Sacchi. Optimal discrimination of quantum operations. Physical Review A*, 71(6), 2005.*

[271] M. F. Sacchi. Entanglement can enhance the distinguishability of entanglement-breaking channels. Physical Review A*, 72(1), 2005.*

[272] S. Pirandola, B. R. Bardhan, T. Gehring, C. Weedbrook, and S. Lloyd. Advances in photonic quantum sensing. Nature Photonics*, 12(12):724–733, 2018.*

[273] M. Sanz, U. Las Heras, J. GarcíaRipoll, E. Solano, and R. Di Candia. Quantum Estimation Methods for Quantum Illumination. Physical Review Letters*, 118(7), 2017.*

[274] E. D. Lopaeva, I. R. Berchera, I. P. Degiovanni, S. Olivares, G. Brida, and M. Genovese. Experimental realisation of quantum illumination. Physical Review Letters*, 110, 2013.*

[275] E. D. Lopaeva, I. Ruo Berchera, S. Olivares, G. Brida, I. P. Degiovanni, and M. Genovese. A detailed description of the experimental realization of a quantum illumination protocol. Physica Scripta*, T160:014026, 2014.*

[276] S. Ragy, I. R. Berchera, I. P. Degiovanni, S. Olivares, M. G. A. Paris, G. Adesso, and M. Genovese. Quantifying the source of enhancement in experimental continuous variable quantum illumination. Journal of the Optical Society of America B*, 31(9):2045, 2014.*

[277] D. G. England, B. Balaji, and B. J. Sussman. Quantum-enhanced standoff detection using correlated photon pairs. Physical Review A*, 99(2):023828, 2019.*

[278] E. Toninelli, T. Gregory, P.-A. Moreau, and M. J. Padgett. Beating classical imaging limits with entangled photons. In S. M. Shahriar and J. Scheuer, editors, Optical, Opto-Atomic, and Entanglement-Enhanced Precision Metrology*, page 59, San Francisco, United States, 2019. SPIE.*

[279] T. Gregory, P.-A. Moreau, E. Toninelli, and M. J. Padgett. Imaging through noise with quantum illumination. Science Advances*, 6(6):eaay2652, 2020.*

[280] Y. Zhang, D. England, A. Nomerotski, P. Svihra, S. Ferrante, P. Hockett, and B. Sussman. Multidimensional quantum-enhanced target detection via spectrotemporal-correlation measurements. Physical Review A*, 101:053808, 2020.*

[281] M. Casariego, Y. Omar, and M. Sanz. Bi-frequency illumination: a quantum-enhanced protocol. arXiv preprint arXiv:2010.15097v2*, 2020.*

[282] J. H. Shapiro. Defeating passive eavesdropping with quantum illumination. Physical Review A*, 80(2), 2009.*

[283] Z. Zhang, M. Tengner, T. Zhong, F. N. C. Wong, and J. H. Shapiro. Entanglement's Benefit Survives an Entanglement-Breaking Channel. Physical Review Letters*, 111(1), 2013.*

[284] S. Barzanjeh, S. Guha, C. Weedbrook, D. Vitali, J. H. Shapiro, and S. Pirandola. Microwave quantum illumination. Physical Review Letters*, 114(8):080503, 2015.*

[285] C. W. S. Chang, A. M. Vadiraj, J. Bourassa, B. Balaji, and C. M. Wilson. Quantum-enhanced noise radar. Applied Physics Letters*, 114(11):112601, 2019.*

[286] J. H. Shapiro. The Quantum Illumination Story. IEEE Aerospace and Electronic Systems Magazine*, 35(4):8–20, 2020.*

[287] J. SabinesChesterking, R. Whittaker, S. K. Joshi, P. M. Birchall, P. A. Moreau, A. McMillan, H. V. Cable, J. L. O'Brien, J. G. Rarity, and J. C. Matthews. Sub-Shot-Noise Transmission Measurement Enabled by Active Feed-Forward of Heralded Single Photons. Physical Review Applied*, 8(1):014016, 2017.*

[288] J. Sabines-Chesterking, A. R. McMillan, P. A. Moreau, S. K. Joshi, S. Knauer, E. Johnston, J. G. Rarity, and J. C. F. Matthews. Twin-beam sub-shot-noise raster-scanning microscope. Optics Express*, 27(21):30810, 2019.*

[289] C. W. S. Chang, A. M. Vadiraj, J. Bourassa, B. Balaji, and C. M. Wilson. Quantum-enhanced noise radar. Applied Physics Letters*, 114(11):112601, 2019.*

[290] E. Abbe. Beiträge zur Theorie des Mikroskops und der mikrosk. Wahrnehmung. Archiv für Mikroskopische Anatomie*, 9:413–468, 1873.*

[291] Rayleigh. XV. On the theory of optical images, with special reference to the microscope. The London, Edinburgh, and Dublin Philosophical Magazine and Journal of Science*, 42(255):167–195, 1896.*

[292] V. Giovannetti, S. Lloyd, L. Maccone, and J. H. Shapiro. Sub-Rayleigh-diffraction-bound quantum imaging. Physical Review A*, 79(1), 2009.*

[293] E. Toninelli, P.-A. Moreau, T. Gregory, A. Mihalyi, M. Edgar, N. Radwell, and M. Padgett. Resolution-enhanced quantum imaging by centroid estimation of biphotons. Optica*, 6(3):347, 2019.*

[294] F. Guerrieri, L. Maccone, F. N. C. Wong, J. H. Shapiro, S. Tisa, and F. Zappa. Sub-Rayleigh Imaging via N -Photon Detection. Physical Review Letters*, 105(16):163602, 2010.*

[295] S. Mouradian, F. N. C. Wong, and J. H. Shapiro. Achieving sub-Rayleigh resolution via thresholding. Optics Express*, page 9, 2011.*

[296] M. Tsang, R. Nair, and X.-M. Lu. Quantum Theory of Superresolution for Two Incoherent Optical Point Sources. Physical Review X*, 6(3):031033, 2016.*

[297] M. Tsang. Quantum Imaging beyond the Diffraction Limit by Optical Centroid Measurements. Physical Review Letters*, 102(25):253601, 2009.*

[298] H. Shin, K. W. C. Chan, H. J. Chang, and R. W. Boyd. Quantum Spatial Superresolution by Optical Centroid Measurements. Physical Review Letters*, 107(8), 2011.*

[299] A. N. Boto, P. Kok, D. S. Abrams, S. L. Braunstein, C. P. Williams, and J. P. Dowling. Quantum Interferometric Optical Lithography: Exploiting Entanglement to Beat the Diffraction Limit. Physical Review Letters*, 85(13):2733–2736, 2000.*

[300] M. D'Angelo, M. V. Chekhova, and Y. Shih. Two-Photon Diffraction and Quantum Lithography. Physical Review Letters*, 87(1):013602, 2001.*

[301] H. J. Chang, H. Shin, M. N. O'Sullivan-Hale, and R. W. Boyd. Implementation of sub-Rayleigh-resolution lithography using an N -photon absorber. Journal of Modern Optics*, 53(16-17):2271–2277, 2006.*

[302] M. Unternährer, B. Bessire, L. Gasparini, M. Perenzoni, and A. Stefanov. Super-resolution quantum imaging at the Heisenberg limit. Optica*, 5(9):1150, 2018.*

[303] Sung Cheol Park, Min Kyu Park, and Moon Gi Kang. Super-resolution image reconstruction: a technical overview. IEEE Signal Processing Magazine*, 20(3):21–36, 2003.*

[304] S. W. Hell and J. Wichmann. Breaking the diffraction resolution limit by stimulated emission: stimulated-emission-depletion fluorescence microscopy. Optics Letters*, 19(11):780, 1994.*

[305] S. W. Hell and M. Kroug. Ground-state-depletion fluorscence microscopy: A concept for breaking the diffraction resolution limit. Applied Physics B Lasers and Optics*, 60(5):495–497, 1995.*

[306] E. Betzig, G. H. Patterson, R. Sougrat, O. W. Lindwasser, S. Olenych, J. S. Bonifacino, M. W. Davidson, J. Lippincott-Schwartz, and H. F. Hess. Imaging Intracellular Fluorescent Proteins at Nanometer Resolution. Science*, 313(5793):1642–1645, 2006.*

[307] M. J. Rust, M. Bates, and X. Zhuang. Sub-diffraction-limit imaging by stochastic optical reconstruction microscopy (STORM). Nature Methods*, 3(10):793–796, 2006.*

[308] F. Göttfert, C. A. Wurm, V. Mueller, S. Berning, V. C. Cordes, A. Honigmann, and S. W. Hell. Coaligned Dual-Channel STED Nanoscopy and Molecular Diffusion Analysis at 20 nm Resolution. Biophysical Journal*, 105(1):L01–L03, 2013.*

[309] J. Hanne, H. J. Falk, F. Görlitz, P. Hoyer, J. Engelhardt, S. J. Sahl, and S. W. Hell. STED nanoscopy with fluorescent quantum dots. Nature Communications*, 6(1):7127, 2015.*

[310] S. Wäldchen, J. Lehmann, T. Klein, S. van de Linde, and M. Sauer. Light-induced cell damage in live-cell super-resolution microscopy. Scientific Reports*, 5(1):15348, 2015.*

[311] R. Tenne, U. Rossman, B. Rephael, Y. Israel, A. Krupinski-Ptaszek, R. Lapkiewicz, Y. Silberberg, and D. Oron. Super-resolution enhancement by quantum image scanning microscopy. Nature Photonics*, 13(2):116–122, 2019.*

[312] J.-E. Oh, Y.-W. Cho, G. Scarcelli, and Y.-H. Kim. Sub-Rayleigh imaging via speckle illumination. Optics Letters*, 38(5):682–684, 2013.*

[313] Y.-H. Zhai, X.-H. Chen, D. Zhang, and L.-A. Wu. Two-photon interference with true thermal light. Physical Review A*, 72(4):043805, 2005.*

[314] Y. Zhai, F. E. Becerra, J. Fan, and A. Migdall. Direct measurement of sub-wavelength interference using thermal light and photon-number-resolved detection. Applied Physics Letters*, 105(10):101104, 2014.*

[315] E. Zhang, H. Lin, W. Liu, Q. Li, and P. Chen. Sub-Rayleigh-diffraction imaging via modulating classical light. Optics Express, 23(26):33506, 2015.

[316] O. Schwartz and D. Oron. Improved resolution in fluorescence microscopy using quantum correlations. Physical Review A, 85(3):033812, 2012.

[317] Y. Israel, R. Tenne, D. Oron, and Y. Silberberg. Quantum correlation enhanced super-resolution localization microscopy enabled by a fibre bundle camera. Nature Communications, 8(1):14786, 2017.

[318] J.-M. Cui, F.-W. Sun, X.-D. Chen, Z.-J. Gong, and G.-C. Guo. Quantum Statistical Imaging of Particles without Restriction of the Diffraction Limit. Physical Review Letters, 110(15):153901, 2013.

[319] D. G. Monticone, K. Katamadze, P. Traina, E. Moreva, J. Forneris, I. R. Berchera, P. Olivero, I. P. Degiovanni, G. Brida, and M. Genovese. Beating Abbe diffraction limit in confocal microscopy via non-classical photon statistics. Physical Review Letters, 113(14):143602, 2014.

[320] E. Rittweger, S. Han, K.and Irvine, C. Eggeling, and S. Hell. Sted microscopy reveals crystal colour centres with nanometric resolution. Nature Photonics, 3:144–147, 2009.

[321] O. Schwartz, J. M. Levitt, R. Tenne, S. Itzhakov, Z. Deutsch, and D. Oron. Superresolution Microscopy with Quantum Emitters. Nano Letters, 13(12):5832–5836, 2013.

[322] A. Classen, J. von Zanthier, M. O. Scully, and G. S. Agarwal. Superresolution via structured illumination quantum correlation microscopy. Optica, 4(6):580, 2017.

[323] T. Gregory, P.-A. Moreau, S. Mekhail, O. Wolley, and M. J. Padgett. Noise rejection through an improved quantum illumination protocol. Scientific Reports, 11:21841, 2021.

[324] W. Seka, S. Jacobs, J. Rizzo, R. Boni, and R. Craxton. Demonstration of high efficiency third harmonic conversion of high power Nd-glass laser radiation. Optics Communications, 34(3):469–473, 1980.

[325] R. Craxton. High efficiency frequency tripling schemes for high-power Nd: Glass lasers. IEEE Journal of Quantum Electronics, 17(9):1771–1782, 1981.

[326] Rp photonics website. [online] https://www.rp-photonics.com/frequency_tripling.html [accessed 02/05/2018].

[327] A. Joobeur, B. E. A. Saleh, T. S. Larchuk, and M. C. Teich. Coherence properties of entangled light beams generated by parametric down-conversion: Theory and experiment. Physical Review A, 53(6):4360–4371, 1996.

[328] M. D'Angelo, Y.-H. Kim, S. P. Kulik, and Y. Shih. Identifying Entanglement Using Quantum Ghost Interference and Imaging. Physical Review Letters, 92(23):233601, 2004.

[329] H. Di Lorenzo Pires and M. P. van Exter. Observation of near-field correlations in spontaneous parametric down-conversion. Physical Review A, 79(4):041801, 2009.

[330] H. Di Lorenzo Pires and M. P. van Exter. Near-field correlations in the two-photon field. Physical Review A, 80(5):053820, 2009.

[331] G. A. Howland and J. C. Howell. Efficient High-Dimensional Entanglement Imaging with a Compressive-Sensing Double-Pixel Camera. Physical Review X*, 3(1):011013, 2013.*

[332] O. Jedrkiewicz, Y.-K. Jiang, E. Brambilla, A. Gatti, M. Bache, L. Lugiato, and P. Di Trapani. Detection of sub-shot-noise spatial correlation in high-gain parametric down conversion. Physical Review Letters*, 93(24):243601, 2004.*

[333] O. Jedrkiewicz, E. Brambilla, M. Bache, A. Gatti, L. A. Lugiato, and P. D. Trapani. Quantum spatial correlations in high-gain parametric down-conversion measured by means of a CCD camera. Journal of Modern Optics*, 53(5-6):575–595, 2006.*

[334] F. Devaux, J. Mougin-Sisini, P. A. Moreau, and E. Lantz. Towards the evidence of a purely spatial Einstein-Podolsky-Rosen paradox in images: measurement scheme and first experimental results. The European Physical Journal D*, 66(7), 2012.*

[335] P.-A. Moreau, J. Mougin-Sisini, F. Devaux, and E. Lantz. Realization of the purely spatial Einstein-Podolsky-Rosen paradox in full-field images of spontaneous parametric down-conversion. Physical Review A*, 86(1):010101, 2012.*

[336] E. Lantz, S. Denis, P.-A. Moreau, and F. Devaux. Einstein-Podolsky-Rosen paradox in single pairs of images. Optics Express*, 23(20):26472, 2015.*

[337] E. Toninelli, P.-A. Moreau, T. Gregory, and M. J. Padgett. A model for the detection of spatially correlated biphotons using a photon-counting camera. arXiv:1911.10562 [physics, physics:quant-ph]*, 2019. arXiv: 1911.10562.*

[338] E. Brambilla, A. Gatti, M. Bache, and L. A. Lugiato. Simultaneous near-field and far-field spatial quantum correlations in the high-gain regime of parametric down-conversion. Physical Review A*, 69(2):023802, 2004.*

[339] K. W. C. Chan, M. N. O'Sullivan, and R. W. Boyd. High-order thermal ghost imaging. Optics Letters*, 34(21):3343–3345, 2009.*

[340] D. S. Tasca, M. P. Edgar, F. Izdebski, G. S. Buller, and M. J. Padgett. Optimizing the use of detector arrays for measuring intensity correlations of photon pairs. Physical Review A*, 88(1), 2013.*

[341] K. W. Chan, J. P. Torres, and J. H. Eberly. Transverse entanglement migration in Hilbert space. Physical Review A*, 75(5):050101, 2007.*

[342] M. H. Rubin. Transverse correlation in optical spontaneous parametric down-conversion. Physical Review A*, 54(6):5349–5360, 1996.*

[343] G. Brida, L. Caspani, A. Gatti, M. Genovese, A. Meda, and I. R. Berchera. Measurement of Sub-Shot-Noise Spatial Correlations without Background Subtraction. Physical Review Letters*, 102(21), 2009.*

[344] C. D. Nabors and R. M. Shelby. Two-color squeezing and sub-shot-noise signal recovery in doubly resonant optical parametric oscillators. Physical Review A*, 42(1):556–559, 1990.*

[345] P. H. S. Ribeiro, C. Schwob, A. Maître, and C. Fabre. Sub-shot-noise high-sensitivity spectroscopy with optical parametric oscillator twin beams. Optics letters, 22(24):1893, 1997.

[346] M. Bondani, A. Allevi, G. Zambra, M. G. A. Paris, and A. Andreoni. Sub-shot-noise photon-number correlation in a mesoscopic twin beam of light. Physical Review A, 76(1), 2007.

[347] T. Iskhakov, M. V. Chekhova, and G. Leuchs. Generation and Direct Detection of Broadband Mesoscopic Polarization-Squeezed Vacuum. Physical Review Letters, 102(18):183602, 2009.

[348] E. Toninelli, M. P. Edgar, P.-A. Moreau, G. M. Gibson, G. D. Hammond, and M. J. Padgett. Sub-shot-noise shadow sensing with quantum correlations. Optics Express, 25(18):21826, 2017.

[349] Y. Kang, K. Cho, J. Noh, D. L. P. Vitullo, C. Leary, and M. G. Raymer. Remote preparation of complex spatial states of single photons and verification by two-photon coincidence experiment. Optics Express, 18(2):1217, 2010.

[350] D. N. Klyshko. Combined EPR and two-slit experiments: Interference of advanced waves. Physics Letters A, 132(6):299–304, 1988.

[351] R. S. Aspden, D. S. Tasca, A. Forbes, R. W. Boyd, and M. J. Padgett. Experimental demonstration of Klyshko's advanced-wave picture using a coincidence-count based, camera-enabled imaging system. Journal of Modern Optics, 61(7):547–551, 2014.

[352] M. McLaren, J. Romero, M. J. Padgett, F. S. Roux, and A. Forbes. Two-photon optics of Bessel-Gaussian modes. Physical Review A, 88(3), 2013.

[353] Y. Aharonov, P. G. Bergmann, and J. L. Lebowitz. Time symmetry in the quantum process of measurement. Physical Review, 134(6B):B1410, 1964.

[354] Y. Aharonov and L. Vaidman. Complete description of a quantum system at a given time. Journal of Physics A: Mathematical and General, 24(10):2315–2328, 1991.

[355] E.-K. Tan, J. Jeffers, S. M. Barnett, and D. T. Pegg. Retrodictive states and two-photon quantum imaging. The European Physical Journal D - Atomic, Molecular and Optical Physics, 22(3):495–499, 2003.

[356] E.-K. Tan, J. Jeffers, S. M. Barnett, and D. T. Pegg. Retrodictive states and two-photon quantum imaging. The European Physical Journal D - Atomic, Molecular and Optical Physics, 29(2):309–309, 2004.

[357] S. M. Barnett, D. T. Pegg, and J. Jeffers. Bayes' theorem and quantum retrodiction. Journal of Modern Optics, 47(11):1779–1789, 2000. arXiv: quant-ph/0106139.

[358] T. B. Pittman, D. V. Strekalov, A. Migdall, M. H. Rubin, A. V. Sergienko, and Y. H. Shih. Can Two-Photon Interference be Considered the Interference of Two Photons? Physical Review Letters, 77(10):1917–1920, 1996.

[359] *N. Krstajić, S. Poland, J. Levitt, R. Walker, A. Erdogan, S. Ameer-Beg, and R. K. Henderson. 0.5 billion events per second time correlated single photon counting using CMOS SPAD arrays.* Optics Letters*, 40(18):4305, 2015.*

[360] *T. Al Abbas, N. A. W. Dutton, O. Almer, S. Pellegrini, Y. Henrion, and R. K. Henderson. Backside illuminated SPAD image sensor with 7.83 µm pitch in 3D-stacked CMOS technology. In* Electron Devices Meeting (IEDM), 2016 IEEE International*, pages 8–1. IEEE, 2016.*

[361] *T. Al Abbas, N. A. Dutton, O. Almer, N. Finlayson, F. M. D. Rocca, and R. Henderson. A CMOS SPAD Sensor With a Multi-Event Folded Flash Time-to-Digital Converter for Ultra-Fast Optical Transient Capture.* IEEE Sensors Journal*, 18(8):3163–3173, 2018.*

[362] *I. Gyongy, S. W. Hutchings, M. Tyler, S. Chan, F. Zhu, R. K. Henderson, and J. Leach. 1kFPS Time-of-Flight Imaging with a 3D-stacked CMOS SPAD Sensor. In* International Image Sensor Workshop Snowbird Resort, Snowbird, United States (2019)*, page R25, 2019.*

[363] *I. Gyongy, N. Calder, A. Davies, N. A. W. Dutton, R. R. Duncan, C. Rickman, P. Dalgarno, and R. K. Henderson. A* 256×256 *, 100-kfps,* 61% *Fill-Factor SPAD Image Sensor for Time-Resolved Microscopy Applications.* IEEE Transactions on Electron Devices*, 65(2):547–554, 2018.*

[364] *S. W. Hutchings, N. Johnston, I. Gyongy, T. Al Abbas, N. A. W. Dutton, M. Tyler, S. Chan, J. Leach, and R. K. Henderson. A Reconfigurable 3-D-Stacked SPAD Imager With In-Pixel Histogramming for Flash LIDAR or High-Speed Time-of-Flight Imaging.* IEEE Journal of Solid-State Circuits*, 54(11):2947–2956, 2019.*

[365] *G. Lubin, R. Tenne, I. Michel Antolovic, E. Charbon, C. Bruschini, and D. Oron. Quantum correlation measurement with single photon avalanche diode arrays.* Optics Express*, 27(23):32863, 2019.*

[366] *H. Defienne, J. Zhao, E. Charbon, and D. Faccio. Full-field quantum imaging with a single-photon avalanche diode camera.* Physical Review A*, (103):042608, 2021.*

[367] *E. Lantz, J.-L. Blanchet, L. Furfaro, and F. Devaux. Multi-imaging and Bayesian estimation for photon counting with EMCCDs.* Monthly Notices of the Royal Astronomical Society*, 386(4):2262–2270, 2008.*

[368] *P. Jerram, P. J. Pool, R. Bell, D. J. Burt, S. Bowring, S. Spencer, M. Hazelwood, I. Moody, N. Catlett, and P. S. Heyes. The LLCCD: low-light imaging without the need for an intensifier. In M. M. Blouke, J. Canosa, and N. Sampat, editors,* Proceedings of SPIE Photonics West 2001 Electronic Imaging, 2001, San Jose, CA, United States (2001)*, pages 178–186, San Jose, CA, 2001.*

[369] *M. Robbins and B. Hadwen. The noise performance of electron multiplying charge-coupled devices.* IEEE Transactions on Electron Devices*, 50(5):1227–1232, 2003.*

[370] *Andor iXon Ultra 888 User's Guide, 2018.*

[371] *K. Matsuo, M. C. Teich, and B. E. A. Saleh. Noise properties and time response of the staircase avalanche photodiode.* IEEE Transactions on Electron Devices*, 32(12):2615–2623.*

[372] *A. G. Basden and C. A. Haniff. Low light level CCDs and visibility parameter estimation.* Monthly Notices of the Royal Astronomical Society*, 347(4):1187–1197, 2004.*

[373] *L. Zhang, L. Neves, J. S. Lundeen, and I. A. Walmsley. A characterization of the single-photon sensitivity of an electron multiplying charge-coupled device.* Journal of Physics B: Atomic, Molecular and Optical Physics*, 42(11):114011, 2009.*

[374] *E. Lantz, P.-A. Moreau, and F. Devaux. Optimizing the signal-to-noise ratio in the measurement of photon pairs with detector arrays.* Physical Review A*, 90(6):063811, 2014.*

[375] *H. Defienne, M. Reichert, and J. W. Fleischer. General Model of Photon-Pair Detection with an Image Sensor.* Physical Review Letters*, 120(20), 2018.*

[376] *J.-L. Blanchet, F. Devaux, L. Furfaro, and E. Lantz. Purely spatial coincidences of twin photons in parametric spontaneous down-conversion.* Physical Review A*, 81(4), 2010.*

[377] *M. Reichert, H. Defienne, X. Sun, and J. W. Fleischer. Biphoton transmission through non-unitary objects.* Journal of Optics*, 19(4):044004, 2017.*

[378] *M. Lampton. The Microchannel Image Intensifier.* Scientific American*, 245(5):62–71, 1981.*

[379] *Andor iStar ICCD User's Guide, 2012.*

[380] *M. P. Buchin. Low-light imaging: Iccd, emccd, and scmos compete in low-light imaging.* Laser Focus World*, 47(51), 2011.*

[381] *L. Cester, A. Lyons, M. Braidotti, and D. Faccio. Time-of-Flight Imaging at 10 ps Resolution with an ICCD Camera.* Sensors*, 19(1):180, 2019.*

[382] *A. F. Abouraddy, M. B. Nasr, B. E. A. Saleh, A. V. Sergienko, and M. C. Teich. Demonstration of the complementarity of one- and two-photon interference.* Physical Review A*, 63(6), 2001.*

[383] *H. Di Lorenzo Pires, C. H. Monken, and M. P. van Exter. Direct measurement of transverse-mode entanglement in two-photon states.* Physical Review A*, 80(2):022307, 2009.*

[384] *R. S. Aspden, P. A. Morris, R. He, Q. Chen, and M. J. Padgett. Heralded phase-contrast imaging using an orbital angular momentum phase-filter.* Journal of Optics*, 18(5):055204, 2016.*

[385] *R. S. Aspden, M. J. Padgett, and G. C. Spalding. Video recording true single-photon double-slit interference.* American Journal of Physics*, 84(9):671–677, 2016.*

[386] *R. Fickler, M. Krenn, R. Lapkiewicz, S. Ramelow, and A. Zeilinger. Real-Time Imaging of Quantum Entanglement.* Scientific Reports*, 3:1914, 2013.*

[387] A. Avella, I. Ruo-Berchera, I. P. Degiovanni, G. Brida, and M. Genovese. Absolute calibration of an EMCCD camera by quantum correlation, linking photon counting to the analog regime. Optics Letters*, 41(8):1841–1844, 2016.*

[388] E. Toninelli. Quantum-enhanced imaging and sensing with spatially correlated biphotons. *PhD thesis, University of Glasgow, 2019.*

[389] L. Qi, F. Just, G. Leuchs, and M. V. Chekhova. Autonomous absolute calibration of an ICCD camera in single-photon detection regime. Optics Express*, 24(23):26444, 2016.*

[390] F. Izdebski. Quantum correlations measured with multi-pixel detectors. *PhD thesis, Heriot-Watt University, 2013.*

[391] A. Michelson. Studies In Optics. *The University of Chicago Press, Chicago, Illinois, 1927.*

[392] A. Khodjakov and C. L. Rieder. Imaging the division process in living tissue culture cells. Methods*, 38:2–16, 2006.*

[393] G. M. Gibson, S. D. Johnson, and M. J. Padgett. Single-pixel imaging 12 years on: A review. Optics Express*, 28:28190, 2020.*